Utrecht University

ALICE

Opleiding Natuur- en Sterrenkunde

The charge-dependent directed flow of D^{*+} and D^{*-} mesons and the calibration of the ZDC Q-vectors in Pb-Pb collisions at the LHC with ALICE

Bachelor Thesis

Olaf Massen

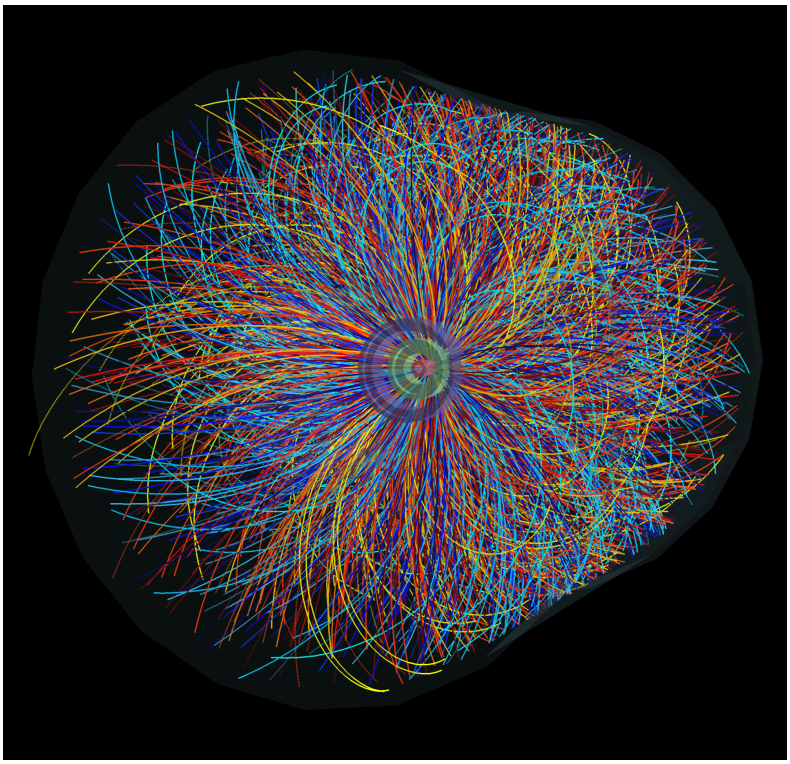

Supervisors:

Dr. A. Grelli
Institute for Subatomic Physics

S. Jaelani MSc.
Institute for Subatomic Physics

June 2020

Abstract

‘

The charge dependent directed flow (v_1) of D^{*+} mesons relative to the spectator plane was determined as a function of pseudorapidity using the ALICE detectors at the LHC in Pb–Pb collisions at $\sqrt{s} = 5.02$ TeV (2015 data set). In contrast with the charge dependent directed flow measurements of D^0 mesons, no significant charge dependent directed flow was found within the limits of the statistical uncertainty in both the $3 < p_T < 6\,\mathrm{GeV}/c$ and $3 < p_T < 36\,\mathrm{GeV}/c$ transverse momentum regions. In order to perform the analysis in the 2018 Pb–Pb data set, reducing the statistical uncertainty, a calibration of the Q-vectors, built using data from the two ZDC detectors, must be performed. A new code was built to perform the calibration of the 2018 (and future) Pb–Pb data sets. The aim is to repeat this analysis improving the statistics. A more accurate analysis of the charge dependent directed flow may lead to constraints on theoretical models describing the development of the strong electromagnetic field produced in heavy ion collisions. These constraints are crucial to find a signal of the chiral magnetic effect in heavy ion collisions.

Contents

Chapter 1

Introduction

One of the greatest questions in modern day physics is: "why is there more matter than antimatter in the universe?" To answer this question one has to study the fundamental particles and forces that make up and govern our universe. These fundamental particles and forces are all, except for the gravitational force, described in the Standard Model of Particle Physics. The Standard Model describes these fundamental particles, such as quarks and leptons, and the forces that govern their interactions. These particles and interactions have been studied extensively both experimentally and theoretically.[1]
In order to understand why the universe is mostly made out of matter instead of antimatter the differences between the two must be understood. The difference between a particle and an antiparticle is its charge. For instance, the antiparticle of an electron is a positron. It has the same properties as an electron except for its charge, which has the same magnitude but the opposite sign. In particle physics there are a number of different symmetries or transformations one can study. Other transformations often considered in particle physics are Parity and Time Reversal. A parity transformation flips the sign of all spatial components and a time reversal transformation reverses time. If these symmetries would all hold there should be no differences in the laws of physics for particles and antiparticles. But, why do we observe more matter than antimatter?[2]
The reason for this could be the violation of a combination of these symmetries. In the weak interaction the Charge-Parity symmetry is violated. The violation of this symmetry, called $\mathcal{CP}$-violation, was found in K^0 decay experiments [3] and explained by theory.[4] The strong interaction, described using the theory of Quantum Chromo Dynamics (QCD), is also allowed to violate $\mathcal{CP}$-symmetry mathematically.[5] There are some theories expanding QCD to make it $\mathcal{CP}$-symmetric but these require new particles.[6] Neither $\mathcal{CP}$-violation in strong interactions nor these new particles have been found experimentally. This is called the strong $\mathcal{CP}$ problem in physics.
The theory of QCD predicts the formation of a new phase of matter at very high temperatures and energy densities, called a Quark-Gluon-Plasma (QGP).[7] It has been shown that in heavy-ion collisions such a QGP can be formed.[8] One of the main physics goals of the ALICE experiment at the LHC is to study the properties of the QGP. This thesis is concerned with the properties of the QGP in strong electromagnetic fields and, indirectly, with the study of $\mathcal{CP}$-violation in the strong interaction.
In heavy-ion collisions the spectator protons, i.e. the protons that do not participate in the

collisions, fly away along the beam pipe creating a very large magnetic field. This field is in the order of $10^{18} - 10^{19}$ Gauss for LHC energies.[9] In such strong magnetic fields theory predicts certain interesting phenomena. One of these is the Chiral Magnetic Effect (CME). The CME is a charge separation along the direction of the magnetic field induced by an imbalance in chirality of a medium.[10] Since chiral imbalance in a medium is a manifestation of local parity-violation the measurement of the CME in heavy-ion collisions can give information on local $\mathcal{CP}$-violation in the strong interaction.[11]
The effects of the CME can be measured using 2- and 3-particle correlators and this has been done by the ALICE collaboration, STAR collaboration and CMS. The results of these measurements are greatly influenced by background and dependent on the strenght and lifetime of the electromagnetic field. These background sources make it hard to decouple the signal from the background and therefor make it necessary to look at other observables. The uncertainty in the electromagnetic fields hinder a clear model for the strength of the CME signal.[12, 13, 14].
A way to find a better model for the CME signal is to find constraints on the strength and lifetime of the electromagnetic field in heavy-ion collisions. This can be done by studying the charge-dependent directed flow (v_1) of particles. This charge-dependent directed flow is not dependent on the chiral imbalance of the system and can therefore be used to measure purely the electromagnetic field. The ALICE collaboration and the STAR collaboration both published papers in which they studied the charge-dependent

Chapter 2

Physics of heavy-ion collisions

Heavy-ion collision experiments are experiments in which, as the name suggests, large atoms such as Lead, Gold or Xenon are stripped of their electrons and made to collide with velocities close to the speed of light. As one can imagine the energies in these collisions are quite large. Temperatures as high as 100.000 times the temperature in the core of the sun are reached. The processes and phenomena that govern these highly energetic collision cannot be described by the laws of Newton. A new, more complex theory is needed and has been developed throughout 20^{th} century starting with the development of Quantum Mechanics all the way to creation of the Standard Model of Particle Physics and theories beyond the Standard Model.
However interesting, a complete account of this development will not be given in here for it would be a thesis on its own. This chapter will cover the most important theoretical topics in order to create a better understanding of the performed analysis and its scientific importance. First an introduction into the Standard Model of Particle Physics will be given, focusing on the theory of the strong interaction. Next a new phase of matter will be introduced: the Quark-Gluon plasma. This is the phase of matter whose properties we study in this thesis. After this the phenomenon of Anisotropic flow will be introduced. Afterwards magnetic fields, chirality and the Chiral Magnetic Effect will be discussed. We'll end this chapter by discussing directed flow in heavy ion collisions.

2.1 The Standard Model and QCD

Everything around us is made out of matter, all sorts of different molecules bound together in different ways. However when taking a closer look all these molecules are more similar than expected. All molecules consist of (a combination of) atoms, which in their turn consist of protons, neutrons and electrons. For a time scientists thought that protons, neutrons and electrons were the fundamental building blocks of nature. They were (as far as we currently know) right about the electron, but not about the protons and neutrons. In 1968 it was proven that protons and neutrons consist of even smaller particles[18, 19], called partons by Feynman. The quark model had already been proposed by Zweig[20] and Gell-Mann[21] but it had not been accepted among the entire scientific society. From this point scientist began to expand the theoretical model of quarks and their interactions with other fundamental

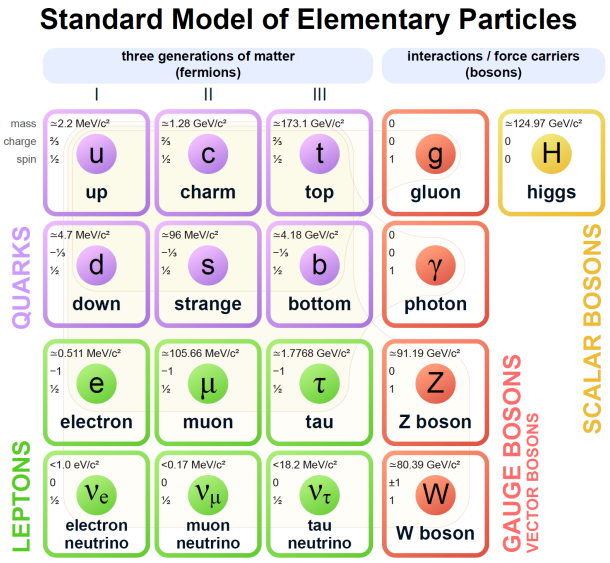

Figure 2.1: An overview of the fundamental particles in the Standard Model and their properties

particles to form what is currently called the Standard Model of Particle Physics.

2.1.1 Introduction to the Standard Model

The Standard Model of Particle physics (SM) is a relativistic quantum field theory. It describes three of the four fundamental forces of nature, the electromagnetic, weak and strong force and the fundamental particles i.e. particles not composed of other particles. The fundamental particles are divided into two categories, Fermions and Bosons.[2]
The fermionic particles, particles with half-integer spin, are the particles that make up matter. They again are divided in two categories: Quarks and Leptons. There are three generations of leptons: electrons and electron neutrino's, muons and muon neutrino's and tau with corresponding tau neutrino's. Quarks are also divided into three generations and in six flavours. The first generation consists of up(u) and down(d) quarks, the second generation consist of charm(c) and strange(s) quarks and the third generation consists of top(t) and bottom(b) quarks. The anti-quarks are denoted by a bar, e.g. $\bar{c}$.[22]
The Bosons, particles with integer spin, of the standard model are the so called force carriers. They are divided in the Gauge Bosons and Scalar Bosons. So far only the Higgs-Boson is of the second category. The Gauge Bosons are photons which carry the electromagnetic force, W^- and Z^0 bosons which carry the weak force and gluons, which carry the strong force. Each of these forces and and force carriers act on some sort of charge. The electromagnetic forces and photons act on electric charge. The weak force and the W^- and Z^0 act on flavour charge. The strong force and the gluon act on colour charge, a certain property of quarks that will be discussed in the next section.[22]
All matter is made of (a combination of) these fundamental particles. Except for dark matter, we do not know what that is made of. One can form a great number of particles out

of different combinations. The particles detected in collider experiments often are Hadrons. Hadrons are particles composed of two or three quarks. A combination of two quarks, i.e. a quark and an anti-quark, is called a Meson and it is an boson. A combination of three quarks, or three anti-quarks, is called a Baryon and it is a fermion. For example, protons and neutrons are both baryons, consisting of two up and one down quark and one up and two down quarks respectively. The mesons of interest in this thesis, the D^{*+} and D^{*-} mesons consist of $(c\bar{d})$ and $(\bar{c}d)$ respectively.[22]
The three forces in the SM can effectively be split up into two categories: The electroweak interaction and the strong interaction. The electromagnetic interaction, described by quantum electrodynamics (QED), and the weak interaction can be described as two different manifestations of the same interaction above a certain energy. This theory was developed by Weinberg[23], Salam[24] and Glashow[25]. However this energy is quite large, so at "normal" energies the symmetry is broken and we observe two different interactions. The strong interaction has not (yet) been combined into one unified interaction. It is described in the theory of Quantum Chromodynamics.

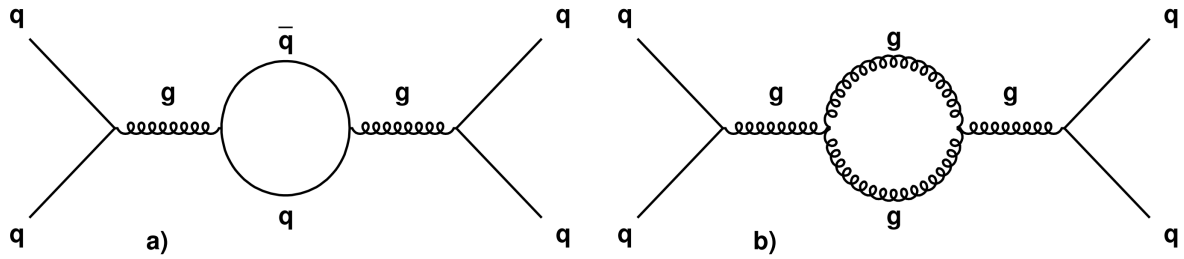

Figure 2.2: Process a) is an example of screening and process b) is an example of anti-screening. Both processes are depicted using Feynman diagrams. Figure taken from [26]

2.1.2 Quantum Chromodynamics

Quantum chromodynamics (QCD) is the theory that describes the interactions between gluons and quarks. It is a non-albelian gauge theory with SU(3) symmetry. As mentioned before gluons act on particles with colour charge. Colour charge can take on three positive values, red, blue and green, and three negative values, anti-red, anti-blue and anti-green. Quarks and gluons are the only two type of fundamental particles that carry colour charge. Quarks (anti-quarks) carry one positive (negative) colour charge and gluons carry both a positive and a negative colour charge. Since gluons act on particles with colour charge and carry colour charge themselves they can self interact[27]. QCD has two important properties that defines its dynamics, colour confinement and asymptotic freedom, which are closely related. Colour confinement stems from the fact that every observed particle is neutral in colour. In a baryon all three quarks or anti-quarks carry a different colour charge and in a meson the quark and anti-quark have colour anti-colour (eg red anti-red) combination, both resulting in a colour neutral particle. At very short distances the strong force effectively vanishes resulting in quarks and gluons acting as free particles.[26] To better understand these phenomena

we consider the coupling constant of QCD and the effect of the self interactions of gluons on the coupling constant.

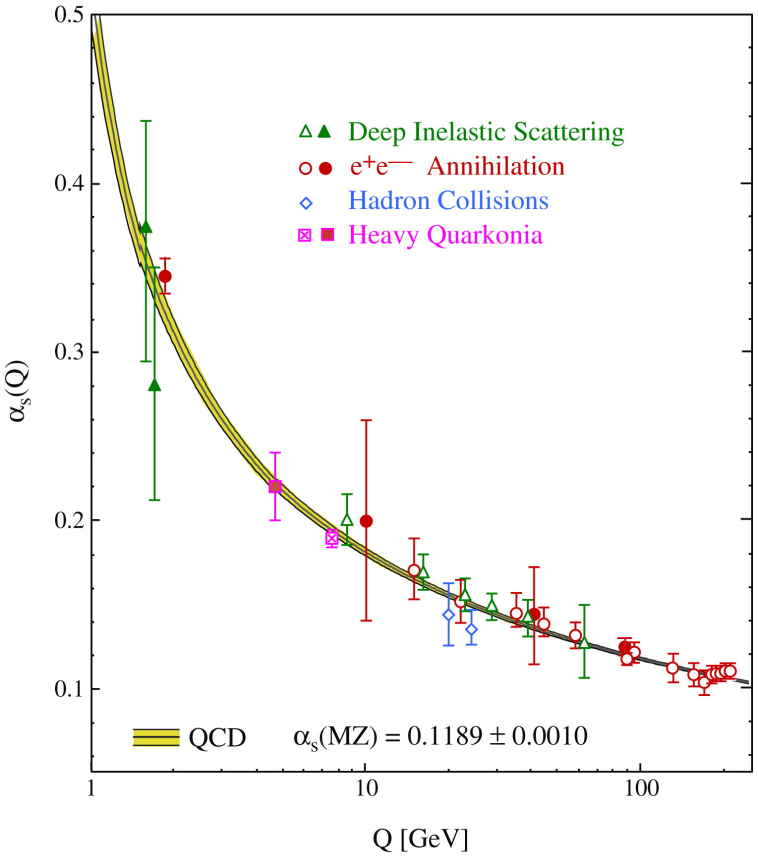

Figure 2.3: Experimental results for determining α_s using different methods up until 2006. Figure taken from [28]

The strength of the strong interaction is determined by the coupling constant α_S, which in turn is determined by two processes called screening and anti-screening. When a electromagnetic charge, example given an electron, is placed in a vacuum electron-positron pairs are created from the vacuum to shield the original charge. This process is called screening and it determines the running coupling constant of QED. The coupling constant of both QED and QCD depend on the momentum-transfer between two particles Q^2. High momentum transfer means a short distance between the two particles while low momentum transfer means a large distance between the two particles. The screening effect in QED decreases the coupling constant at large distances and increases the coupling constant at short distances. The coupling constant of QCD does exactly the opposite. It vanishes at high momentum transfer while it diverges at low momentum transfer. This is due to the process of anti-screening. If a colour charge is placed in a vacuum it can be screened by quark anti-quark pairs. However, since gluons can self interact a pair of gluons can be created. The two processes are shown in Fig. 2.2. These gluons are attracted to one another, effectively increasing the interaction strength. Anti-screening increases in strength at large distances and decreases in strength at

short distances. In QCD the process of anti-screening is leading with respect to screening. In QED anti-screening is not present since photons do not self-interact.[29] The behaviour of α_s can be seen in Fig. 2.3 and the curve is described by Eq. 2.1[22]:

$$\alpha_s(Q^2) = \frac{12\pi}{(11n - 2f)\ln(\frac{Q^2}{\Lambda^2_{QCD}})}. \tag{2.1}$$

The vanishing coupling constant means that quarks and gluons effectively behave as free particles at high momentum transfer. This is what is called asymptotic freedom. Colour confinement and the momentum transfer dependence of the coupling constant are closely related. Consider a quark anti-quark pair. If we would want to create "free" colour charge by pulling them away from each other in vacuum the coupling constant and thus the energy would increase dramatically. This energy would continue to rise up until the point it is more favourable to create a new quark anti-quark pair from the vacuum. These will combine with the original quark and anti-quark to form two mesons, preventing the formation of free colour charge.[28]

QCD in the high momentum transfer regime is well understood. Many calculations can be performed analytically using perturbation theory. Processes in this regime are called Hard QCD processes. On the other hand, QCD processes in the low energy regime cannot be calculated using perturbation theory. For this regime phenomenological descriptions or numerical models must be used. A successful, but not flawless, approach is lattice QCD (LQCD). LQCD looks at non-pertubative calculations on a discrete space-time. This approach is useful to calculate equilibrium QCD events and it can be used to study the thermodynamics and the equation of state of QCD matter.[30, 31]

2.1.3 The QCD phase-diagram

Strong interacting matter can, just like other substances such as water, be found in different phases. Strong interacting matter at ordinary everyday life densities and temperatures is found as confined hadrons. As we go to higher densities, temperatures or both we start to explore different regions of the QCD phase-diagram. The parameters considered when probing the QCD phase-diagram are Temperature T and baryo-chemical potential μ_B, which is proportional to the baryon density. The phase diagram is being explored both theoretically as experimentally. Theorist use Lattice QCD to study the phase transitions from hadronic matter to more exotic phases such as the Quark-Gluon plasma (QGP) or the super colour conducting phase (CSC).[32] These are particularly interesting phases of matter since the universe was a QGP very shortly after the Big Bang[33] and the inside of neutron stars may show CSC like properties[34]. LQCD has been able to predict the temperature at which strong interaction matter undergoes a phase transition from hadrons to QGP at zero baryon density. These conditions have been met in heavy ion collision experiments such as the LHC in Geneva and RHIC at the Brookhaven National Laboratory. This transition is a smooth crossover, a second order phase transition. Calculations at zero temperature and a finite baryo-chemical potential show a first order phase transition. This combination leads to the believe that there must be and critical point somewhere in the phase diagram.[35] In Fig.

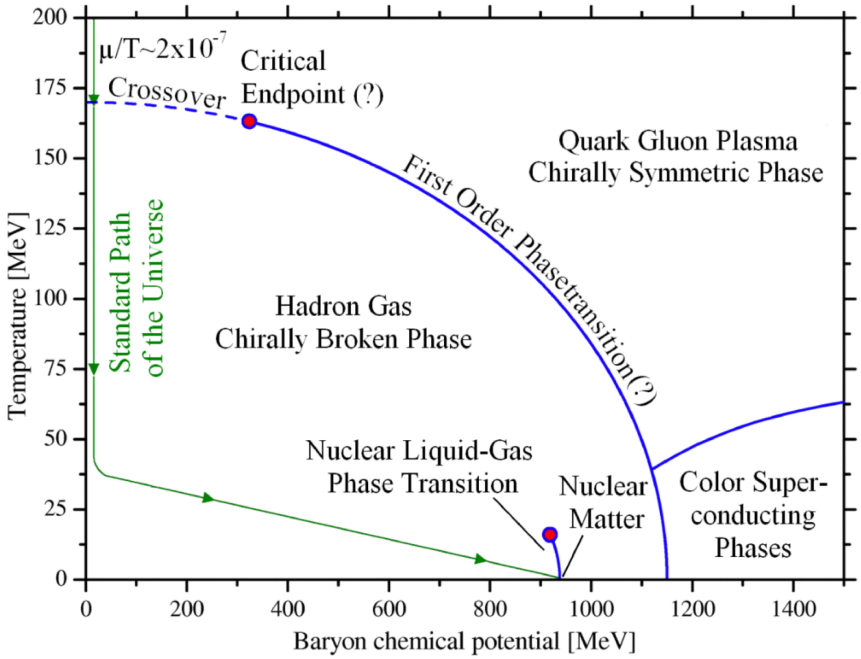

Figure 2.4: An illustration of the QCD phase diagram. Figure taken from [36]

2.4 the QCD phase diagram is shown. Heavy ion collision explore the upper left corner of the phase diagram i.e. very low baryon density and very high temperature. The search for this critical point currently is an active field of research both theoretically as experimentally. In the next section we will discuss the quark-gluon plasma in more detail, as it is the phase whose properties we study in this thesis.

2.2 Quark-Gluon plasma

In 1975, shortly after the idea of asymptotic freedom was developed, both N. Cabibo & G. Parisi[37] and J.C. Collins & M.J. Perry[38] realised that at very high temperatures and densities quarks and gluons would form a new phase of matter. In this new phase of matter quarks and gluons are deconfined and it was named the Quark-Gluon Plasma. Many experiments were performed colliding heavy ions at increasing energies to try and find this new phase of matter. In 2000 scientist had gathered enough evidence of the formation of QGP in heavy ion collisions to be able to claim that they found it at the lead beam program at CERN[8]. From this point the attention naturally shifted from finding QGP to studying its properties. It was found that the QGP formed in these heavy ion collisions is strongly coupled and it can accurately be described using relativistic hydrodynamics[39]. Another fascinating property of strongly-coupled QGP is that it acts as an almost perfect liquid with a very small specific shear-viscosity. [40] This section will first discuss the various stages of heavy ion collisions and the formation of QGP in these collisions. After this Anisotropic flow will be introduced as a way to describe the expansion of the QGP.

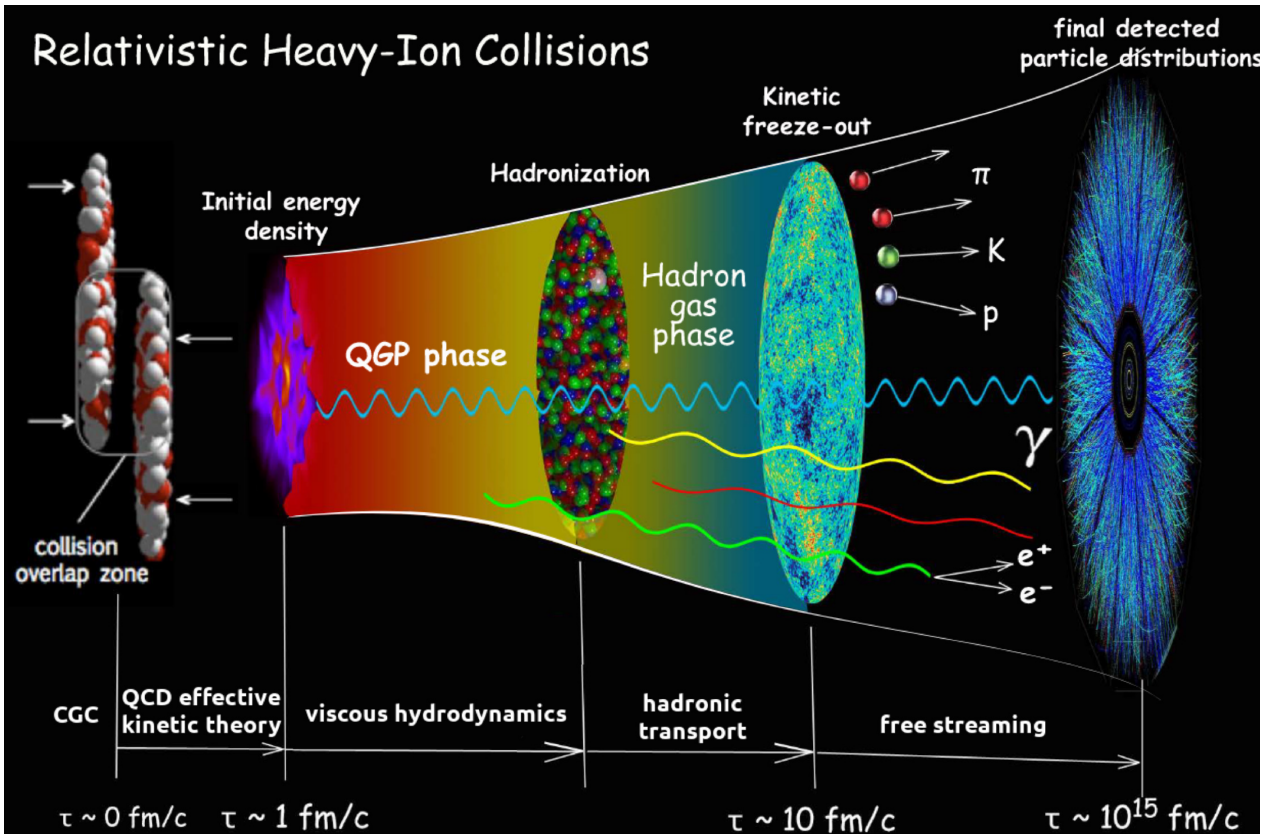

Figure 2.5: An illustration of the different phases of a heavy-ion collision. The estimated duration of each phase are also shown. Figure taken from [17]

2.2.1 QGP formation in Heavy-Ion Collisions

In Heavy-Ion Collisions (HIC) we strip two heavy atoms, for example two lead atoms, from their electrons, we accelerate them to almost the speed of light and then we let them collide. Due to Lorentz contraction the lead nuclei are no longer round but they are flat like a pancake. This of course does not happen with two lead nuclei at a time, but with bundles of lead nuclei colliding very rapidly after each other. Heavy-ion collisions happen in different, consecutive stages: the initial state, pre-equilibrium, QGP, hadronisation and rescattering. In Fig. 2.5 a schematic view is shown of the evolution of a heavy-ion collision. The initial state is described by the distribution of the quarks and gluons in the colliding nuclei. This distribution can be determined by models based on gluon saturation[41], which are quite complicated and by the more simple Monte-Carlo Glauber model.[42] During the pre-equilibrium phase the gluons from the initial state start to interact. Due to this interaction almost all the entropy is created and therefore also the multiplicity[1] of the collision is determined. Entropy creation occurs only during the pre-equilibrium process due to the low specific-viscosity of the QGP. After the pre-equilibrium phase we enter the QGP phase. As mentioned before the QGP is strongly coupled and it can be described by relativistic hydrodynamics. During this phase the QGP expands and cools down until the temperature falls below a critical temperature of

[1] the amount of particles produced

155 MeV. The system then enters the hadronisation phase. The deconfined quarks and gluons start to bundle together to form hadrons. These hadrons then scatter whilst expanding until they no longer interact. The formed hadrons are then detected by the detector. For a more complete and in-depth view of heavy-ion collisions one could check [41]. All information on all the different stages of HIC's must be deducted from this stream of hadrons. One source of information is the anisotropic flow.

2.2.2 Anisotropic flow in QGP

Heavy ion collisions are almost never head on. Most of the time there is a certain overlap region between the two ions. This overlap region determines the initial shape of the QGP. As can be seen from Fig. 2.6a the formed QGP is not isotropically distributed. This anisotropy in the initial QGP shape is transferred to an anisotropy in the momentum distribution of the produced particles as shown in Fig. 2.6b. The collective expansion of the QGP plays an important role in the distribution of momentum as well. In Experiments one considers the anisotropy in the azimuthal distribution. The azimuthal angle ϕ will be defined for the ALICE detector in the next chapter. The anisotropy in momentum can be given in so called flow coefficients v_n. These flow coefficients are the Fourier-components of the harmonic expansion of the ϕ-distribution with respect to a certain plain in the collision.[43] Anisotropic flow measurements are the measurements of these flow coefficients. Flow coefficients are defined as in equation 2.2[44]:

$$v_n = \langle cos(n[\phi - \Phi_n]) \rangle, \tag{2.2}$$

with Φ_n a plane in the collision and the brackets around the cosine denote an average over all particles. In this thesis Φ_n will be the neutron spectator plane Ψ_n. The neutron spectator plane is defined as the transverse direction in which the spectator neutrons move after the collision. These flow coefficients are called directed flow (v_1), elliptical flow (v_2), triangular flow (v_3) and so on. Each flow coefficient has its own sources and physical meanings. Directed flow, the flow coefficient of interest, will be considered later in this chapter.

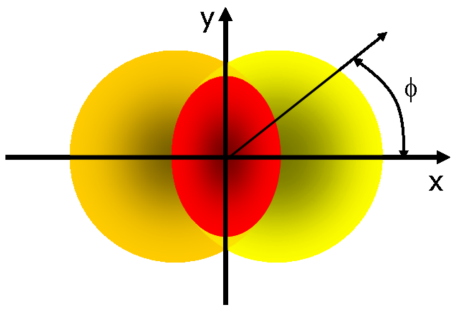

Figure 2.6(a): In a non-central HIC the overlap region, shown in red, is anisotropic in the azimuthal angle ϕ. Figure taken from [44]

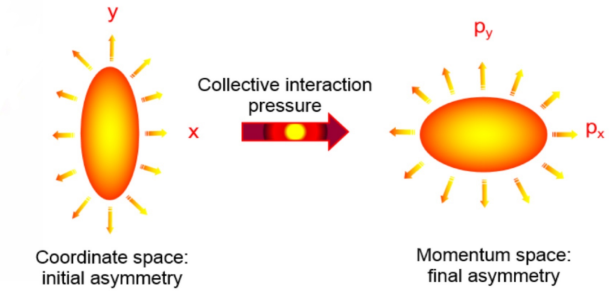

Figure 2.6(b): The initial anisotropy in shape of the interaction region is transferred to an anisotropy in momentum. Figure adapted from [17]

2.3 The Chiral Magnetic Effect

To better understand why the analysis of the charged-dependent directed flow is of scientific importance, we need to discuss the Chiral Magnetic Effect (CME) and its place in the SM. Since chirality and CME are theoretically very complicated concepts, we choose clarity over precision in order to form a clear qualitative idea of the concepts. A precise and accessible review can be found in [45].

2.3.1 Chirality

The standard model particles all have a different set of properties which we use to define and distinguish them, like mass, electrical charge and spin. However there are a lot more properties within the SM that are used to describe the behaviour and properties of the particles. In order to explain what chirality is, we will first discuss helicity since it is more straightforward to explain and related to chirality. Helicity is a property of particles, in its turn closely related to the spin of a particle. The spin of a particle is often defined using a arbitrary chosen z-axis. The helicity of a particle is the component of the spin of a particle that points along the momentum of said particle. So for a spin $\frac{1}{2}$ particle this can be $\pm\frac{1}{2}$. If the spin component in the momentum direction is $\pm\frac{1}{2}$ this is called positive(negative) helicity, denoted by an helicity of ± 1, or a right(left)-handed state. In nature not all particles can be left-handed or right-handed. In fact it is found that there exist only left-handed neutrino's and right-handed anti-neutrino's [46].[2]
Chirality is closely related to helicity, but its definition is more complicated and subtle. For particles without mass it in fact is the same as helicity. For massive particles there is a difference. One could do a Lorentz-transformation into another reference frame such that the momentum points in the opposite direction changing the sign of the helicity, while for particles without mass this cannot be done. Chiral states can be seen as a linear combination of the left-handed and right-handed state helicity states.[3].[1] For this thesis it is sufficient to think of chirality and helicity as the same property i.e. the alignment of the spin with momentum.

2.3.2 The Chiral Magnetic Effect

As we have stated before it has been proven that a QGP can be formed during high energy heavy ion collisions. In each collision or event, the formed QGP will have a small imbalance in chirality, there would be more left-handed or right-handed particles due to local $\mathcal{P}$- and $\mathcal{CP}$-violation. If a medium with a net chirality would be placed in a magnetic field this will induce a current along the magnetic field. Due to this current there will be a separation of positive and negative charges inside of the medium. In the case of QGP this will thus lead to a separation of quarks. This separation of charges is called the chiral magnetic effect and it is illustrated in Fig. 2.7.[10] This charge separation occurs early on in the collision and

[2]With the discovery if neutrino oscillations it was found that neutrino's do have mass[47], so this statement is not true strictly speaking. It does hold for photons and gluons

[3]For a more precise definition of chiral states and their background one can read Chapter 5 of [2]

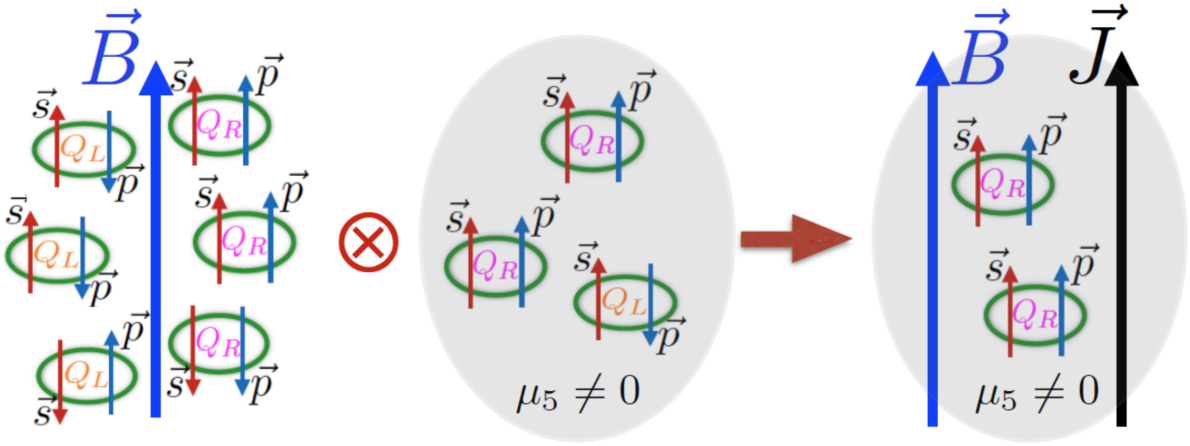

Figure 2.7: An illustration of the Chiral magnetic effect for more right-handed than left-handed particles with a positive charge. **J** is the induced current and μ_5 the chiral chemical potential, which can be seen as a measure for the amount of imbalance in the system. Figure taken from [45]

the separated quarks will be affected by the overall expansion of the system. However some traces of this separation should remain after hadronisation.[48]

Measuring the CME in heavy ion collision should in theory be possible and it will give us information on local $\mathcal{CP}$-violation in a system governed by QCD. To measure the CME we need observables sensitive to the CME. Two relative straight forward observables that can be used are charge dependent two- and three-particle correlators.[49] These observables are defined as

$$\delta_{\alpha,\beta} = \langle \cos \phi_\alpha - \phi_\beta \rangle \tag{2.3}$$

$$\gamma_{\alpha,\beta} = \langle \cos \phi_\alpha + \phi_\beta - 2\Psi_{RP} \rangle, \tag{2.4}$$

Where $\alpha, \beta = \pm$, ϕ is again the azimuthal angle and Ψ_{RP} the reaction plane.[17] The downside of these observables is that they are influenced by background. So we need to find a way to decouple the background from the signal. Also the strength and lifetime of the electromagnetic field plays an important role in creating a measurable CME signal, for without a magnetic field there can be no CME. One way to get a clearer view on the possible strength of the CME signal is to establish boundaries on the strength and lifetime of the magnetic field in heavy-ion collisions. For this we need to find an observable that is not affected by the chiral imbalance of the system, so we can measure purely the electromagnetic fields. One candidate for this is the directed flow v_1.

2.4 Directed flow in heavy ion collisions

As we have seen before, the directed flow is the first Fourier component of the harmonic expansion of the azimuthal angle ϕ. The directed flow in a heavy ion collision can be used as a measure for the response of the system to a magnetic field. We expect from lattice QCD studies that QCD matter like the QGP is electrically conductive.[50] If this is true, then we expect the formation of electromagnetic currents inside a QGP system due to the initial magnetic field caused by the spectator protons. These electromagnetic currents have a well defined effect on the directed flow that can be distinguished from background making it a suited observable to put restriction on the evolution and strength of the magnetic field.[51] In order to properly discuss this we will first give a brief recap on electromagnetism. Then the electromagnetic response of the QGP will be discussed. Afterwards the effects on and other origins of directed flow will be discussed. We will finish this section and chapter by going over the reason why we study directed flow of D^{*+} mesons.

2.4.1 Electromagnetism

The electromagnetic force is one of the four fundamental forces in nature and maybe the most well understood force in the standard model. The theory as we know it today found its origin in the end of the 19$^{\text{TH}}$ century, when James Clerk Maxwell combined the Electric force and Magnetic force into one theory consisting of four equations: Maxwell's equations. These four equations link together the electric fields and magnetic fields and have had far reaching consequences. To give and example: the idea of a constant speed of light came from the fact that in electromagnetism the speed of light in vacuum is only dependent on electrical permittivity and magnetic permeability of the vacuum.
The four equations of Maxwell are given by the following four laws:

$$\nabla \cdot \mathbf{E} = \frac{\rho}{\epsilon_0} \qquad \text{(Gauss's law)}, \quad (2.5)$$

$$\nabla \cdot \mathbf{B} = 0 \qquad \text{(Gauss's law for } \mathbf{B}\text{)}, \quad (2.6)$$

$$\nabla \times \mathbf{E} = -\frac{\partial \mathbf{B}}{\partial t} \qquad \text{(Ampère's law)}, \quad (2.7)$$

$$\nabla \times \mathbf{B} = \mu_0(\mathbf{J} + \epsilon_0 \frac{\partial \mathbf{E}}{\partial t}) \qquad \text{(Faraday's law)}. \quad (2.8)$$

In these equations $\mathbf{B}$ and $\mathbf{E}$ are the magnetic and electric field, $\mathbf{J}$ is the electric current density, ρ is the electrical charge density and μ_0 and ϵ_0 the permittivity and permeability of free space respectively. From these four equations other expressions can be derived like the expression for the Lorentz force and the Biot-Savart law[4]:

[4]This is most easily done by using writing the electric and magnetic fields in its Lorentz covariant form. The derivation is done in Chapter 8 of [52]

$$\mathbf{F} = q\mathbf{E} + q\mathbf{v} \times \mathbf{B} \qquad \text{(Lorentz Force)}, \quad (2.9)$$

$$\mathbf{B}(\mathbf{r}) = \frac{\mu_0}{4\pi} \int \frac{\mathbf{J}(\mathbf{r'}) \times (\mathbf{r} - \mathbf{r'})}{|\mathbf{r} - \mathbf{r'}|^3} d^3r' \qquad \text{(Biot-Savart)}. \quad (2.10)$$

Both these expressions will be of importance later on in this chapter when we will discuss electric and magnetic currents in context of heavy ion collisions.

2.4.2 Charged currents in heavy ion collisions

In heavy-ion collisions extremely strong and short lived magnetic fields can be created by spectator protons. In a non central HIC parts of the colliding nuclei do not participate in the collision. These nucleons are called the spectator nucleons and consist of both neutrons and protons.The spectator protons fly away from collision in both directions at speeds close to the speed of light creating an electric current. If we consider the effects of this current at the interaction point, the electric current gives rise to a magnetic field, as is illustrated in Fig. 2.8a The lifetime of this magnetic field is very short however, in the order of 1 fm/GeV. However the possible electrical conductivity can extend the lifetime of the magnetic field extensively as can be seen in Fig. 2.8b Under influence of this magnetic field the charged particles in a QCD system, the quarks, will start to generate currents according to Faraday's law. Another effect of the magnetic field is also due to the expansion of the system in the longitudinal direction. This brings about a force that is simply the Lorentz force. In Fig. 2.9 both these effects are shown and as can be seen there both effects drive particles of opposite charge in opposite directions. These directions switch sign if we consider opposite rapidities. These charged currents will lead to signals that can be measured in the form of direct flow as we will discuss next.

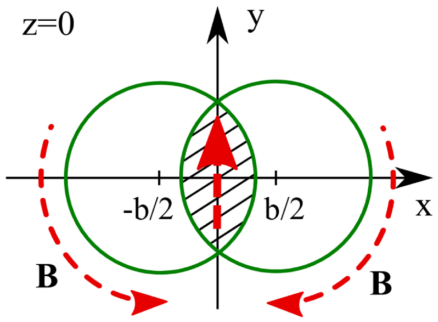

Figure 2.8(a): An illustration of the initial magnetic field in an non-central heavy-ion collision at the interaction point. The magnetic field **B** is depicted by the dashed lines. Figure taken from [17]

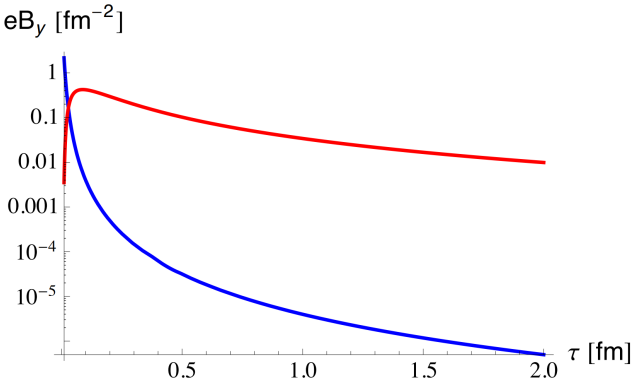

Figure 2.8(b): The strength of the magnetic field at the interaction point versus time for a QCD system without electrical conductivity (blue) and with electrical conductivity (red). The y-axis is logarithmic. Figure from [51]

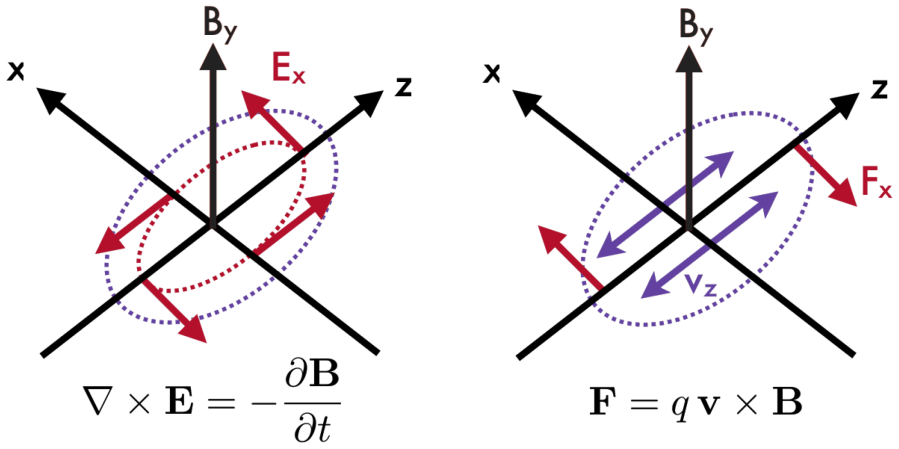

Figure 2.9: The electromagnetic response of the QCD system to the initial magnetic field. The response due to Faraday's law is shown in the left figure and the response due to the Lorentz force is shown in the right figure. The dashed purple contours represent the QCD system and the continuous lines represent the velocity. The red lines represent the EM response. Figure taken from [17]

2.4.3 Sources of directed flow in heavy ion collisions and directed flow of D^{*+} mesons

There are multiple sources of directed flow. One source of directed flow are the charged currents as discussed in the section above. In terms of directed flow these currents will lead to charge- and rapidity- odd flow

$$v_1(+,\eta) = -v_1(+,-\eta) = v_1(-,-\eta) = -v_1(-,\eta). \tag{2.11}$$

The $\pm$ refers to the electrical charge of the particle. This type of directed flow is called charge-dependent directed flow and it be measurable perpendicular to the magnetic-field plane.

Other sources of directed flow are connected to the initial tilt of the QCD-system[53] and to dipole-like fluctuations in the initial geometry of the QCD-system.[54] This is where our choice for particles comes into play. We will be analysing the directed flow of D^{*+} and D^{*-} mesons, containing a charm quark. Due to several effects the directed flow of charm containing particles is expected to be considerably larger than that of particles only containing light quarks. One of the reasons is that Charm quarks are created in hard scattering processes early on in the collision while the light quarks are mainly created later on in soft-processes. The charm quarks have a smaller initial tilt of the system leading to a larger dipole moment thus a larger directed flow.[55] Another reason is that the formation time of the charm quarks is around 0.1fm/GeV at which the initial magnetic field is at its strongest. These charm quarks are expected to carry this large initial kick with them leading to a larger directed flow.[56] Since the directed flow for the D^{*+} and the D^{*-} mesons have opposite sign the difference between the two Δv_1 will be most suited for experimental measurements.

Chapter 3

Experimental Setup

Heavy-ion collision experiments are no experiments one can do in its backyard. They require large facilities and they often are the result of a collaboration between multiple research institutes, universities and countries. The data used in this thesis was collected at the ALICE experiment, one of the four major experiments at the Cern accelerator complex, more specific at the Large Hadron Collider. This chapter will be an introduction to the Large Hadron Collider and to the ALICE experiment. First a short overview of the Large Hadron Collider and the CERN accelerator complex is given. In the second part of this chapter a more detailed overview of ALICE and the relevant sub-detectors will be given.

3.1 The Large Hadron Collider

Just outside Geneva on the French-Swiss border lies CERN, the European Organisation for Nuclear Research. At CERN they have built the largest particle accelerator in the world: The Large Hadron Collider (LHC). The LHC is a circular particle accelerator built around 100 meters underground. It consist of two beam pipes, each carrying particles in the opposite direction through a 27-kilometre-long ring. The LHC was designed to accelerate protons and lead nuclei, although it can also collide other nuclei as Xenon. For most of the time the LHC performs proton-proton collisions, but for about one month per year it performs lead-lead collisions. The LHC can reach centre-of-mass collision energies of $\sqrt{s} = 7$ TeV per proton and $\sqrt{s} = 2.76$ TeV per lead nucleus. To reach these energies the particles go through a series of accelerators before entering the LHC. Lead ions are accelerated by the linear accelerator LINAC 3, the Low Energy Ion Ring (LEIR), the Proton Synchrotron (PS) and the Super Proton Synchrotron (SPS) respectively before being injected in the LHC. Protons follow a similar path. They start in the linear accelerator LINAC 2 after which they enter the the Proton Synchrotron Booster (PSB). From here on they enter the PS and they follow the same path as the lead ions through the SPS into the LHC. In Fig. 3.1 a schematic representation of the accelerator complex is shown. A more detailed description of the LHC can be found in [57].

In the LHC there are four different interaction points where the beam pipes cross and the particles collide. At each of these four collision points a detector is located. ATLAS

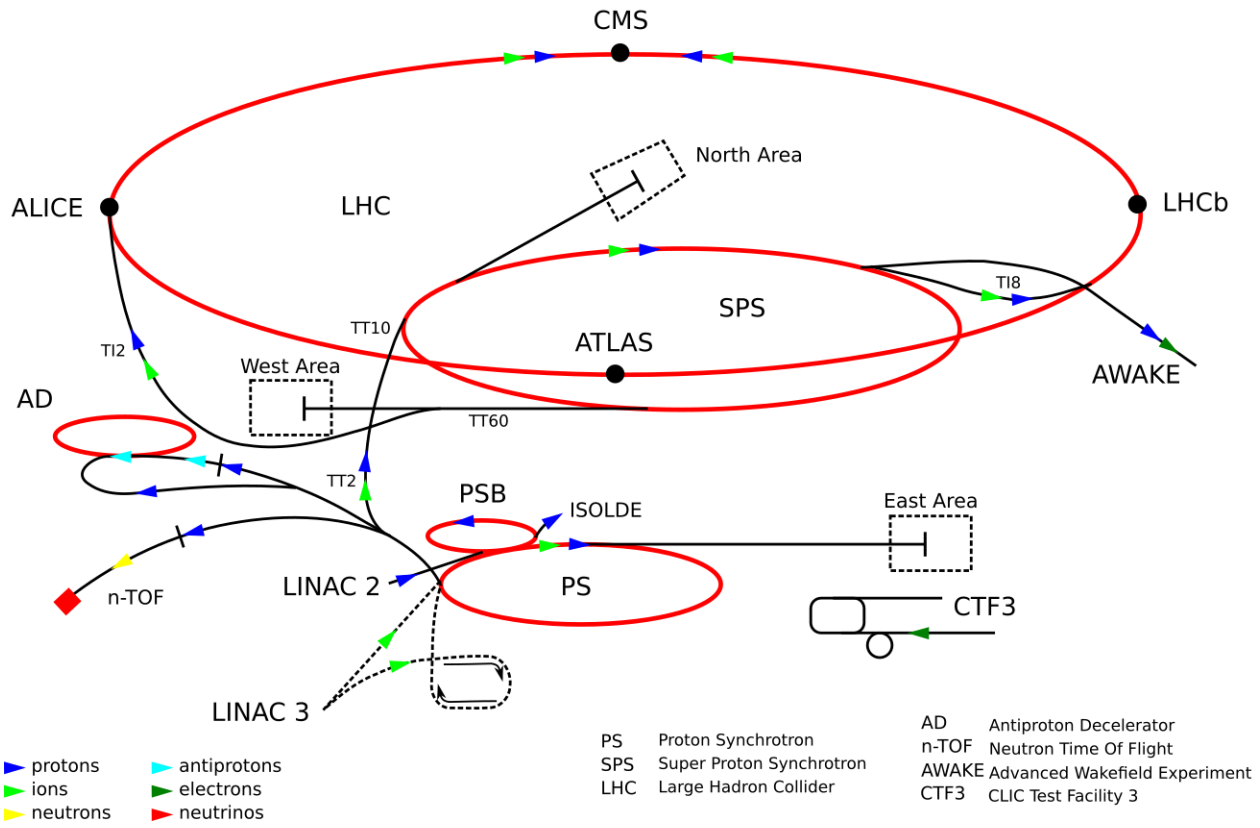

Figure 3.1: A schematic view of the accalerator complex at CERN. Figure taken from [17]

(A Toroidal LHC ApparatuS) is situated at point 1 and is a general-purpose detector [58]. ALICE (A Large Ion Collider Experiment) is situated at point 2 and it is dedicated to the study of heavy-ion collisions[59]. At point 3 the CMS (Compact Muon Solenoid), a multi-purpose detector, is located[60]. Finally a point 4 LHCb is located, an experiment dedicated to CP-violation in B-physics[61]. Besides these four major detectors there are a three smaller experiments at the LHC, TOTEM, MoEDAL and LHCf[62].

3.2 ALICE experiment

The ALICE experiment is situated at point 2 of the CERN accelerator complex and it is designed to gather data from heavy-ion collisions. The main purpose of the ALICE experiment is "to characterise the physical properties of the Quark-Gluon Plasma (QGP), a state of matter created under the extreme conditions of temperature and energy density created in nuclear collisions."[63] It consists of 18 sub-detectors, has a size of 16 x 16 x 23 m^3 and weighs around 10 000 tons. These detectors are divided mainly in two groups. One group focuses on the detection of all kinds of particles and it is build in a central barrel around the beam-pipe, embedded in a very strong magnet. The second group focuses on the detection of muons and is built to the right of the central barrel, outside the magnet. A schematic view of the ALICE detector is given in Fig. 3.2. In the following subsections four of the sub-detectors will be discussed: the ITS, TPC, V0 and ZDC. These detectors played a key-role in obtaining the

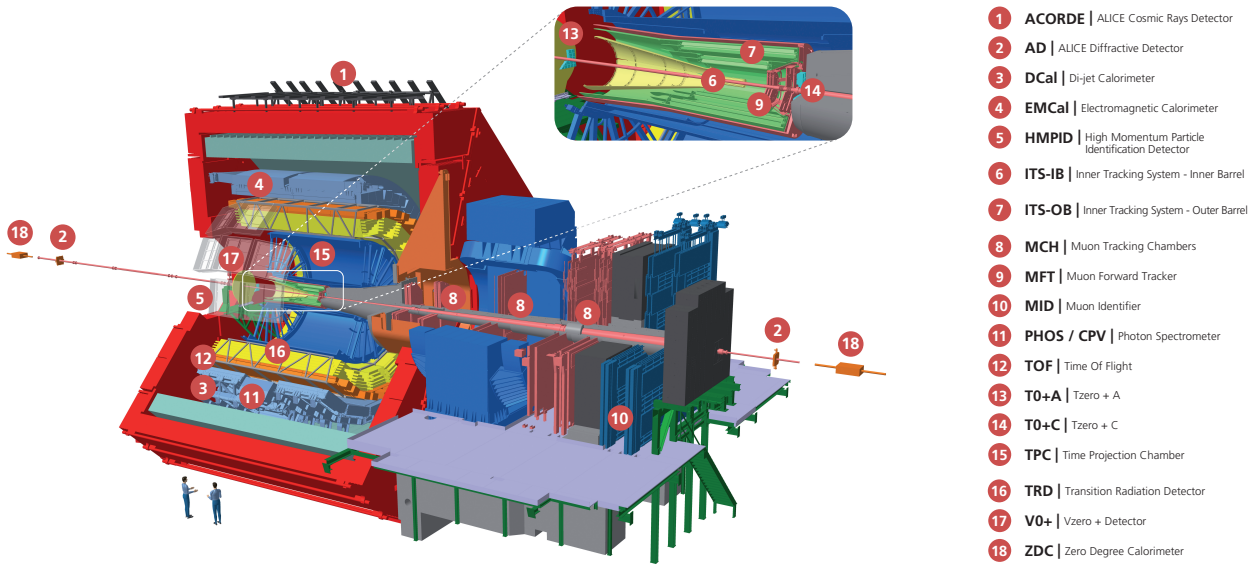

Figure 3.2: A schematic view of the ALICE detector during run 2

data used for the analysis. In these four detectors the same coordinate system is used. The z-axis points along the beam-pipe and the x-axis points towards the centre of the LHC. A more detailed description of the ALICE detector and its physics performances can be found in [59]

In the ALICE experiment the properties of the detected particles and its kinematics are given in certain parameters which need to be defined before we can discuss the detectors in more detail. These parameters are the transverse momentum, the azimuthal angle and the pseudorapidity. The transverse momentum of detected particles, p_{T}, is the magnitude of the momentum-projection in the $x-y$ plane. The azimuthal angle ϕ is the angle of the particle in the $x-y$ plane. Pseudorapidity η is defined as

$$\eta = -\ln\left(\tan\frac{\theta}{2}\right) = \frac{1}{2}\ln\left(\frac{|\vec{p}|+|p_L|}{|\vec{p}|-|p_L|}\right), \tag{3.1}$$

where θ is the polar angle i.e. the angle in the $y-z$ plane and p_L the z-component of the the three-dimensional momentum vector $\vec{p}$.

3.2.1 ITS

The Inner Tracking System (ITS) is the first detector particles encounter after a collision. The ITS consists of 6 silicon detector layers: two Silicon Pixel Detectors (SPD), two Silicon Strip Detectors (SSD) and two Silicon Drift Detectors (SDD). The main tasks of the ITS are the reconstruction of the primary and secondary vertex of charm and hyperon (baryons with one or more s quark but no c, t or b quark) hadrons, particle identification and tracking of low-momentum particles and improvement of the momentum and angle measurements of the TPC.[64]
The Silicon detectors are built concentric around the beam pipe at the interaction point.

They cover the full azimuthal range of the detector and have pseudorapidity coverage of $|\eta| < 0.9$. The first two layers (SPD) have radii of 3.9cm and 7.6cm, the next two layers (SSD) have radii of 15.0 cm and 23.9 cm and the last two layers (SDD) have radii of 38.0 cm and 43.0 cm.[65] Fig. 3.3 gives a schematic view of the ITS.

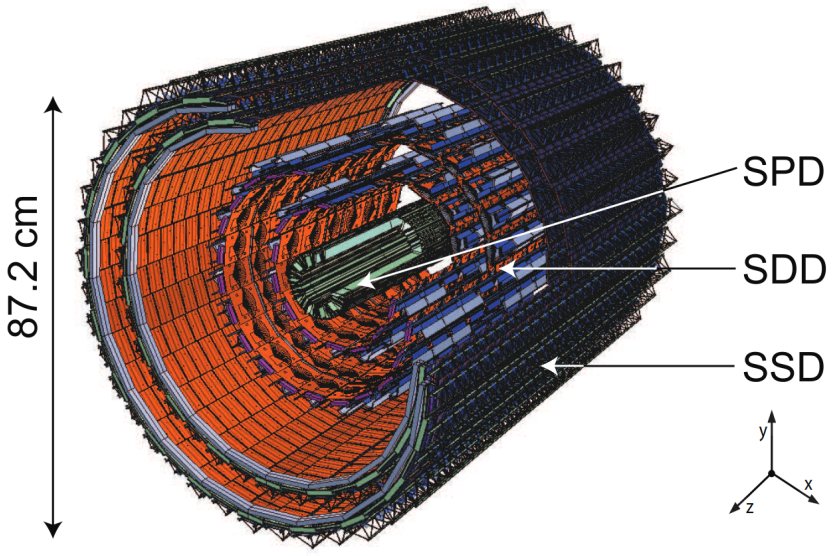

Figure 3.3: A schematic view of the ITS detector. Figure taken from [65]

3.2.2 TPC

The Time Projection Chamber (TPC) is the main tracking detector around the central barrel. It is a gaseous detector designed for tracking charged particles and particle identification (PID). The TPC is a cylindrical barrel with an inner radius of 85cm, an outer radius of 247cm and it extends 5m along the beam pipe. Like the ITS the TPC has an azimuthal coverage of 360° and a pseudorapidity coverage of $|\eta| < 0.9$. It has a volume of 90m^3 and it is filled with a gas mixture of Neon (85.7%), Carbon Dioxide (9.5%) and Nitrogen (4.8%).[66] The volume of the TPC is divided in two chambers by a cathode, creating an electric field along the z-axis pointing towards the ends of the TPC where the anodes are located. When a charged particle goes through the TPC it ionises the gas molecules. The freed electrons then flow towards the anodes at the end of the TPC chamber ionising even more gas molecules. The radial and azimuthal position can be read of directly from the signal at the end plate while the z-position of the particle can be determined through the drift time of the electrons. Since each particle type has a specific amount of freed electrons at a certain momentum, one can distinguish different particles and determine their momentum by looking at the number of electrons at the end plates.[66] The particle identification is done in combination with another detector called the time-of-flight (TOF) detector, which makes use of the time it takes for a particle to reach the TOF from the primary vertex.[67] A schematic view of the TPC can be found in Fig. 3.4

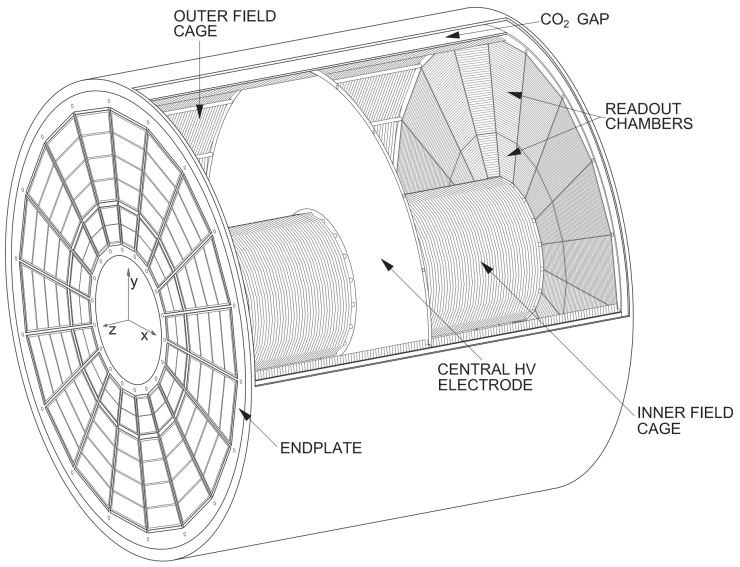

Figure 3.4: A schematic view of the TPC detector. Figure taken from [68]

3.2.3 V0

The V0 detectors are two cylindrical scintillators placed asymmetrically at opposite sides of the interaction point along the beam pipe, as can be seen in Fig. 3.5. A scintillator is material which emits a photon when a charged particle traverses it. In the V0 detector these photons are guided through optical fibres towards photo-multiplier tubes to transform the photons into an electric current. This signal can be read out and the amount of particles traversing the scintillator is proportional to the signal strength. The V0 detectors are both divided into four rings, each divided into 8 segments. The V0A detector is placed 3.3m from the interaction point and it covers a pseudorapidity range of $2.8 < \eta < 5.1$. The V0C detector is placed closer to the interaction point at distance of 0.9m. The V0C covers a pseudorapidity range of $-3.7 < \eta < -1.7$. These detectors are used for monitoring collision parameters like centrality and luminosity. Besides that the play an important role in the trigger system of the ALICE detector (triggers will be explained in chapter 4).[69]

3.2.4 ZDC

The zero-degree calorimeters (ZDC) are two hadronic calorimeters placed on opposite side of and at a distance of 115m from the interaction point at beam axis rapidity. They both are divided into two separate calorimeters, a proton and a neutron calorimeter. The ZDC's measure the energy of spectator protons and neutrons and it is mainly used for measuring the collision centrality, determining spectator plane and as a part of the ALICE trigger system. The neutron calorimeter is placed in between the two beam-pipes and the proton calorimeter is placed just outside the beam-pipe since spectator protons are deflected by the magnetic field inside the central barrel. Their placement with respect to the beam-pipe can be seen in Fig. 3.6a When an incoming nucleon hits the absorber material of the calorimeter it generates a cascade of particles. When these particles traverse the Quartz fibers embedded

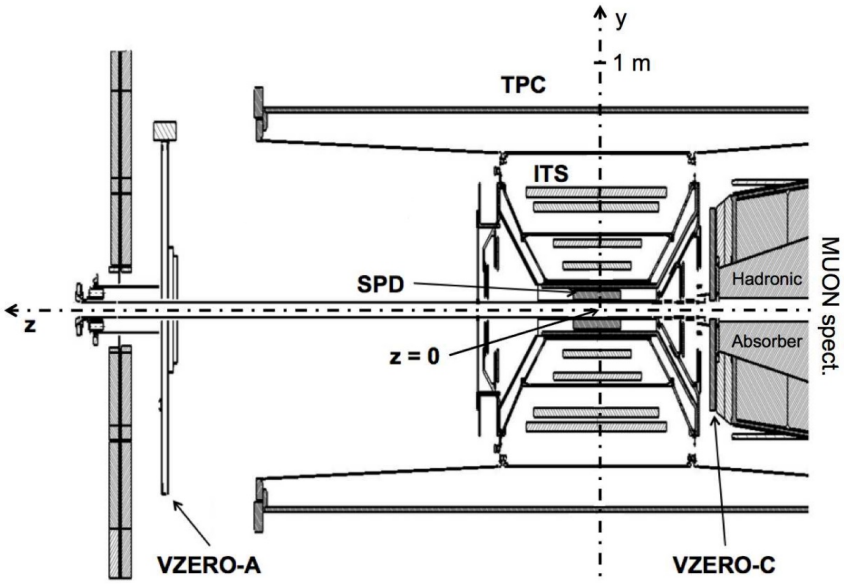

Figure 3.5: A schematic view of the V0 detectors placing in the central barrel. Figure taken from [69]

in this absorber material, Cherenkov radiation, which consists of photons, is generated. These photons are guided through optical fibers towards photo-multiplier tubes where the light is transformed into a signal. These signals can then be read out.[70, 71]
In this thesis we work with data from the neutron ZDC's so we will consider these in a bit more detail. The neutron ZDC has dimensions of 7 x 7 x 100 cm^3 in the x-, y- and z-direction. The ZDC is divided into 4 segments each containing 1 bundle of optical fibers. One extra bundle of optical fibers is spread out over all four segments, creating 5 different channels or towers.[70] This can be seen in Fig. 3.6a

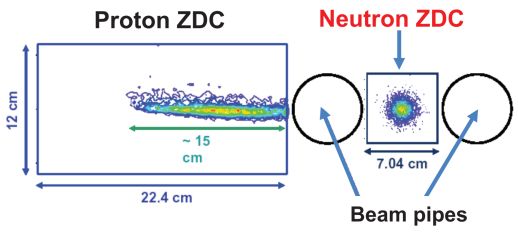

Figure 3.6(a): In this figure the placement of the Neutron and proton ZDC with respect to the beam pipe can be seen. Figure taken from [71]

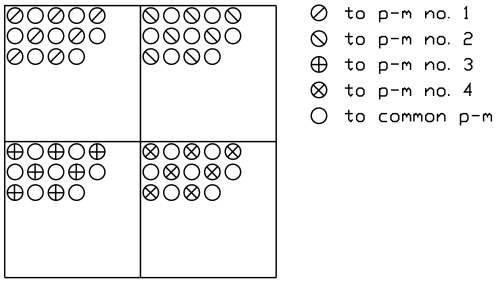

Figure 3.6(b): A schematic view of the five separate towers inside the neutron ZDC's. Figure taken from [70]

Chapter 4

Analysis Methods

In heavy ion collisions thousands of particles are produced in each event. The ALICE detector gathers about 1 petabyte of data each year. All this data is processed and stored later to be used for studies just like this one. The question is, how do we retrieve the information that we need from this large heap of information. In this Chapter the steps taken in this analysis will be discussed. First the method for measuring the directed flow of particles will be covered. Then the process of selecting the D^{*+} and D^{*-} mesons from all this data will be discussed. Afterwards the process of cut optimisation, in which the selection criteria for the D^{*+} particles are going to be optimised, and various sources systematic uncertainty in this measurement will be considered, which will conclude the section on the directed flow measurement. The next section describes the calibration of the ZDC Q-Vectors for the 2018 data. Finally an overview will be given of the analysis framework used by the ALICE collaboration.
This analysis has been done for the D^0-meson[15], so in order to be able to compare the results the same line of reasoning as in this paper will be used. Besides that many of the same definitions and selection criteria will be used, when possible. To perform this analysis the code available to the ALICE collaboration had to be updated to accommodate the D^{*+} analysis. The code used for the ZDC calibration has been built from scratch. Precise overviews of the data-set and the sets of code used in this analysis are given Appendix A and Appendix B respectively.

4.1 Measuring charge-dependent directed flow

To be able to measure the charge-dependent directed flow we first need to define it in terms of observables we can measure in the ALICE detector. Multiple ways to measure directed flow have been developed. In this analysis v_1 is measured using so called flow vectors or Q-vectors and the scalar-product method, which will both be discussed hereafter. The directed flow of the D-mesons is ultimately determined using a simultaneous fit of the invariant mass of the particle and the v_1. To create a better understanding of this process invariant mass plots will briefly be discussed as to what they are, how they are created and what they look like.

4.1.1 Q-vectors and the scalar product method

As mentioned above, in the analysis Q-vectors will be used as a framework to determine the directed flow. To be more precise, Q-vectors built using data from the neutron ZDC-detectors which gather information about the deflected spectator neutrons. These Q-vectors are defined as:[72]

$$Q_{x,y}^{A,C} = \frac{\sum_{i=1}^{4}(x_i, y_i) \cdot E_i^{A,C}}{\sum_{i=1}^{4} E_i^{A,C}}, \tag{4.1}$$

where in $Q_{x,y}^{A,C}$ the A and C represent the two sides of the ZDC detectors and x, y represent the x and y component of the Q-Vector. The summation over i is over the four segments of each of the ZDC-detectors and (x_i, y_i) correspond to the position of these segments with respect to the centre of the detector. Finally $E_i^{A,C}$ is the energy in the i^{th} segment of the ZDC detector on the A or C side.

When the LHC performs its lead-lead collisions this is done in so called runs. All these runs have a slightly different the position of the collision point.[15] Therefore the constructed Q-vectors have to be re-centred to compensate for this. The re-centring is done with respect to collision centrality and vertex position[1]. The procedure for re-centring is explained in more detail in [17]. The direction of the spectator neutrons is then determined using these corrected Q-vectors for each event. From the way these Q-vectors are constructed one expects a certain correlation between the Q^A and Q^C vectors. The expected correlations are $\langle Q_x^A Q_x^C \rangle = \langle Q_y^A Q_y^C \rangle < 0$ and $\langle Q_x^A Q_y^A \rangle = \langle Q_x^C Q_y^C \rangle = 0$. During the re-centring it was noticed that these correlations for the re-centred Q-vectors did not act as expected for collisions with a centrality larger than 40%. For that reason the chosen centrality interval for this analysis is 10%-40%. The lower limit of 10% will be discussed later on when discussing the track selection and topological cuts.

Constructing these Q-vectors is the first step towards determining the directed flow of the D^{*+} and D^{*-} mesons. Next the observable v_1 must be defined according to the scalar product method.[73] According to this method v_1 on the A or C side of the ZDC detector is defined as

$$v_1^{A,C} = \frac{\langle u_x Q_x^{A,C} + u_y Q_y^{A,C} \rangle}{\sqrt{|\langle Q_x^A Q_x^C + Q_y^A Q_y^C \rangle|}}, \tag{4.2}$$

with u_x and u_y the two components of the of the unit flow vector $\vec{u} = (\cos\phi, \sin\phi)$ for the D^{*+} or D^{*-} meson. The directed flow relative to the neutron spectator plane is then defined as

$$v_1^{odd} = \frac{1}{2}(v_1^A - v_1^C). \tag{4.3}$$

This is the so-called odd component of the directed flow. The odd-component of the directed flow is sensitive to both initial state fluctuations as to the initial tilt of the system, while the

[1]To be more precise: the vertex position with respect to the centre of the ALICE detector

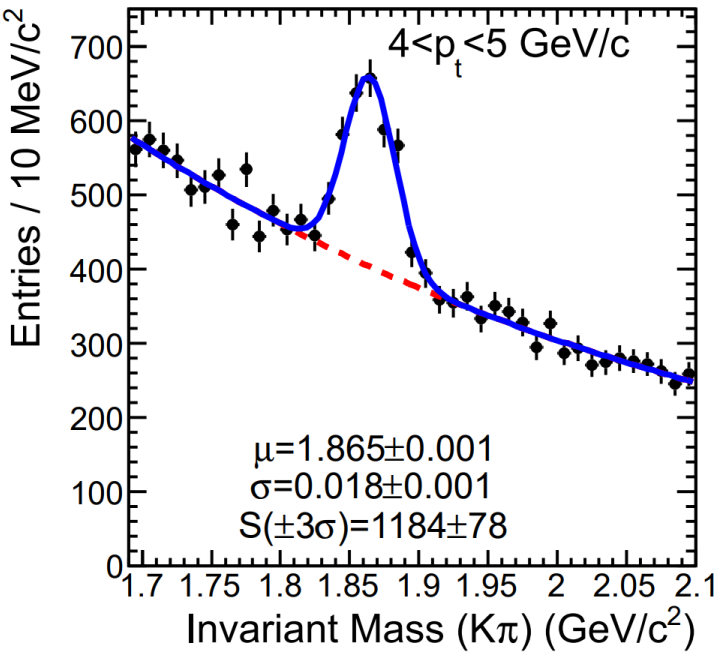

Figure 4.1: An example of an invariant mass plot for the D^0 meson in proton-proton collisions. The red-dotted line represents the background of the measurement and the blue-line represents the background plus the signal. Figure adapted from [74]

even component of the directed flow is not sensitive to the initial tilt of the system.[72] The sign of the directed flow is chosen relative to the ZDC-A detector (at positive η). From this point on when the directed flow of particles is mentioned in this thesis v_{odd}^1 is meant.

4.1.2 Invariant mass analysis

In order to perform the analysis not only a definition of the directed flow is needed, invariant mass plots are also necessary to determine the directed flow. An invariant mass plot is used to show that a particle is present in a measurement. Each particle has a certain specific invariant mass. To perform an invariant mass analysis the particle we are looking for will be selected from all the data using certain restrictions specific to that particle. These restrictions depend on what kind of particle one is searching for. The specific restrictions for the D^{*+}-meson will be discussed in the next section. Not all selected particles, often called candidate particles, are the particle that is being searched for. A large part of the candidates are background particles and in an invariant mass analysis they for the background signal, whose shape is particle specific as well. The candidate particles which indeed are the particles that are being searched for build up a signal around the theoretical invariant mass. This signal has the shape of a Gaussian distribution[2] and is found on top of the background

[2]The natural shape of an invariant mass peak would be a Breit-Wigner distribution, however due to the momentum resolution effects the observed shape is best described by a Gaussian distribution

signal. If no Gaussian peak is observed it is possible that the restriction applied were not successful in selecting the particle and allowed too much background signal or the statistics of the measurements were too poor. In this case it is very well possible the particle was created in the collisions, it is only hidden in the background noise.
An example of an invariant mass analysis for the D^0 meson can be found in Fig. 4.1. The peak-position of the Gaussian, denoted with μ, then corresponds to the invariant mass of the particle. Each particle and each decay topology can lead to a different kind of invariant mass plot with a different background function and a specific peak position μ and peak width σ

The invariant mass analysis of the D^{*+} meson is performed in a slightly different way. For detecting the D^{*+} meson the difference in mass between the D^{*+} and D^0 meson, one of its decay products[3], is used to create an invariant mass plot. This procedure reduces the background contribution significantly.[74] The invariant mass plot of a D^{*+} has a background shape that can best be described using a power exponential function combined with a Gaussian for the peak signal. The equation for the background function is:

$$N_{bkg}(x) = \alpha\sqrt{x - m_\pi} \cdot e^{-\gamma\cdot(x-m_\pi)}, \tag{4.4}$$

where α and γ are free parameters and m_π the theoretical mass difference between the D^{*+} and D^0. This is the background function that will be used for the invariant mass plots in the simultaneous fits.

When considering invariant mass plots there are certain terms that are often used and reported. These are Signal, Background, Signal over Background and Significance. Each of them will be discussed briefly. The Background of an Invariant mass plot, often denoted by B, is simply the integral under the background function (The red dotted line in Fig. 4.1). Signal, often denoted by S, is the integral under the Gaussian peak minus the Background. Signal over Background, often denoted by S/B, is the ratio of signal over background. The Significance of the peak is given by $\frac{S}{\sqrt{S+B}}$. All of these are usually reported for a region three standard deviations (σ) from the peak position.

4.1.3 Simultaneous fit

To find the directed flow of the D-mesons a simultaneous fit is performed on the invariant mass plot and the calculated v_1 separately for the D^{*+} and D^{*-}. The functions used to fit the invariant mass and the directed flow are the following:

$$N(m) = N_{D^{*+}}(m) + N_{bg}(m), \tag{4.5}$$

$$v_1(m) = \frac{v_1^{D^{*+}} N_{D^{*+}}(m) + v_1^{bg}(m) N_{bg}(m)}{N_{D^{*+}}(m) + N_{bg}(m)}, \tag{4.6}$$

with reported value of the directed flow is $v_1^{D^{*+}}$ and $N_{D^{*+}}(m)$ and $N_{bg}(m)$ are the number of D-mesons and the number of background particles as a function of the invariant mass. As

[3] In the section on track selection and topological cuts the decay of the D^{*+} meson will be discussed in more detail

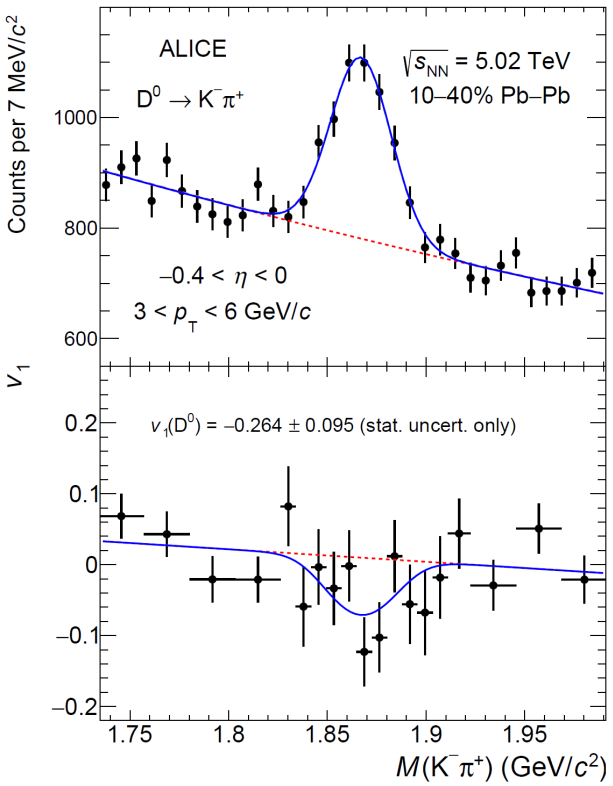

Figure 4.2: An example of a simultaneous fit of the invariant mass (top panel) and the directed flow (bottom panel) for the D^0 measurement. The red-dotted line represents the background of the measurement and the blue-line represents the background plus the signal. Figure taken from [15]

mentioned before the background function for the D^{*+} invariant mass is given by Eq. 4.4. The background function for the directed flow fit is given by a linear fit. In Fig. 4.2 an example from the directed flow measurement of the D^0 meson is shown. These measurements are then done for two transverse momentum intervals, $3 < p_T < 6$ GeV/c and $3 < p_T < 36$ GeV/c, and in four pseudorapidity intervals being $-0.8 < \eta < -0.4, -0.4 < \eta < 0, 0 < \eta < 0.4$ and $0.4 < \eta < 0.8$.

The final results for the charge-dependent directed flow will be given in the form of the difference between the directed flow of the D^{*+} and D^{*-} mesons:

$$\Delta v_1 = v_1(D^{*+}) - v_1(D^{*-}). \tag{4.7}$$

This Δv_1 will then be plotted as a function of pseudorapidity for both transverse momentum regions. These will then be fitted with a linear function as it is expected from theory that Δv_1 shows linear behaviour in the used pseudorapidity interval. The parameter of the linear fit can then be used to deduce information on the electric and magnetic field.[75]

4.2 Track Selection and Topological cuts

Up to this point it was discussed how to perform the analysis in general, but we need to focus now how the D^{*+} and D^{*-} mesons can be selected from all the data that is gathered in each event. First the behaviour of the D^{*+} meson must be discussed when it is produced in an event and how it decays. The D^{*+} meson is a particle with a very short lifetime so upon creation it immediately decays into a π^+ and a D^0. The D^0 meson in its turn decays into a π^+ and a K^-. The branching ratio's[4] for these two decay modes are[76]:

$$D^{*+} \longrightarrow D^0 + \pi^+ \qquad \text{(Strong Decay)} \qquad BR = (67.7 \pm 0.5)\% \quad (4.8)$$

$$D^0 \longrightarrow K^- + \pi^+ \qquad \text{(Weak Decay)} \qquad BR = (3.89 \pm 0.04)\%. \quad (4.9)$$

The D^{*+} decays immediately upon creation at the interaction point. This point is also called the primary vertex. From this primary vertex the D^0 meson than flies away in a certain direction for its lifetime and then decays. This point is called the secondary vertex. A schematic drawing of the decay topology, as it is called in particle physics, is shown in Fig. 4.3. Since both the D^{*+} and the D^0 meson decay so quickly, only the Pions and Kaons are measured in the ALICE detector. Using the decay topology of the D^{*+} meson several selection criteria can be imposed upon the properties of these Pions and Kaons. These are so called topological cuts. From these topological cuts the decay topology is then reconstructed by combining candidate Pions and Kaons that fulfil our conditions. If the reconstruction can be done a D^{*+} candidate was found. The decay properties change as a function of transverse momentum and the selection criteria are never air-tight. This means you will never select only D^{*+}-mesons. There will always be a certain amount of background present in the measurement, as can be seen in Fig. 4.1. If a collision is head-on or central (0%-10% centrality) the amount of background increases greatly. Therefore the lower limit in centrality is chosen to be 10% in this analysis. Too much background in present in these data sets to perform this analysis.

In this analysis a total of 16 topological cut variables are used. All sixteen are listed below with a short description.[78] The values used as a starting point in this analysis correspond to the values used in the analysis of the nuclear-modification factor in the $30\% - 50\%$ centrality region from [79]. As mentioned above the decay topology depends among other things on the transverse momentum, so the topological cut variables are set in certain transverse momentum bins. These values were then optimised in the process of cut optimisation, which will be discussed in the next section. The eventual cut values used in the analysis can be found in the Appendix.

- The invariant mass of the D^0-meson
- The distance of closest approach (D_{ca}). This is the distance between the primary and secondary vertex.
- The cosine of the angle between the Kaon and the Pion from the D^0 decay in the rest frame of the D^0 θ^*

[4] A branching ratio is the chance of a particle to decay via that channel, given in percentages.

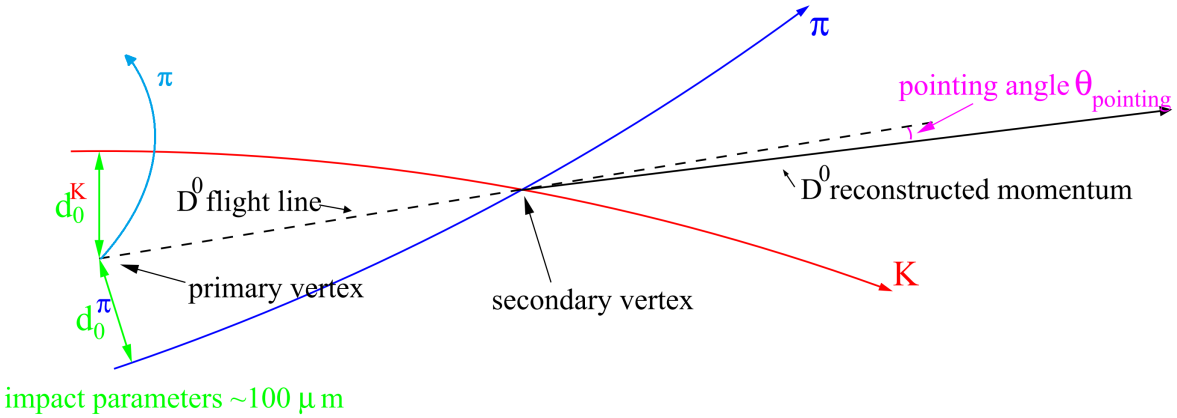

Figure 4.3: An illustration of the decay of a D^{*+}-meson into a D^0-meson and a Pion. Some topological cut variables are also illustrated in the figure such as the impact parameter d_0 and the pointing angle θ_P. Figure adapted from [77]

- The transverse momentum of the Kaon and the Pion produced in the D^0 decay
- The impact parameter of the Kaon (d_0^K) and the Pion (d_0^π) produced in the D^0 decay. This is the shortest distance from the flight line of the Kaon to the primary vertex. This cut variable is illustrated in Fig. 4.3.
- The product of the impact parameter of the Pion and the Kaon ($d_0 d_0$)
- The cosine of the angle between the D^0 flight line and the reconstructed momentum of the Pion and Kaon called the pointing angle (θ_P)
- The invariant mass half width of the D^{*+}
- The half width of the difference in invariant mass of the D^{*+} and the D^0
- The minimum and maximum transverse momentum of the soft-pion.
- "theta, angle between the soft-pion and decay plane of the D0 [rad]"
- The absolute value of the projection of $\cos\theta_P$ on the x, y-plane.
- The projection of the decay length on the x, y-plane divided by the uncertainty in the decay length projected in x, y-plane (Norm L_{XY}).

Besides the selections set because of the decay topology selections also have to be made based on the quality of the data gathered by the ALICE detectors. Not every particle that is created and goes through the detectors is measured perfectly. For a wild variety of reasons these particles are sometimes only measured partly. Therefor selections also must be made based on the quality of the selected and reconstructed tracks. The Pion- and Kaon-tracks are reconstructed using the ITS and TPC detectors and the particle identification is done using information from the TPC and the TOF detector.

For the track reconstruction of the π^+ and K^- from the D^0 decay a hit was required in at least three out of the six ITS layers, a minimum of 70 hits in the TPC out of a maximum of 159 and a $p_T > 0.1$GeV/c. For the soft-pion also three hits were required in the ITS, but only 50 hits in the TPC and there were no requirements for the transverse momentum of the soft-pion. For all tracks it was required that $|\eta| < 0.8$ since this corresponds with the acceptance of the ALICE detector.
All the selection criteria described above let us select both D^{*+} and D^{*-} mesons. The distinction between the two, necessary to determine Δv_1, was made by considering the charge of the soft-pion. If the soft-pion was positively charged the particle was labelled a D^{*+} and if the soft-pion was negatively charged the particle was labelled a D^{*-}. These labels were then used to perform the simultaneous fit on either only the D^{*+} mesons or only the D^{*-} mesons.

4.3 Cut Optimisation

The starting point of this analysis was a set of topological cuts optimised for the analysis of the nuclear-modification factor in the 30%-50% centrality region. This set of cuts was used as a basis from which a cut optimisation was done to create a new set of cuts suited for the directed flow analysis. This optimisation process goes as follows.
From the 16 cutting variables a certain amount of variables will be chosen to be optimised. In explaining the process it was chosen to optimise three variables, but this can easily be extended to more than three.[5] Depending on what the current value of the cutting variables is, either a tighter or a looser set of cuts is needed.[6]. Since our analysis is performed in the 10%-40% centrality region more background signal is expected than in an analysis in the 30%-50% centrality region, since the collisions are more head-on. Thus it is expected that the optimised value for the cutting variables will be tighter than the current one. For the three variables that are going to be optimised a tighter value is chosen than the current one for each p_T-interval. The code used for the cut optimisation than varies these three variables in eight steps, creating a set of cuts for each combination in each p_T interval. So in the end there will be 512 combinations for each p_T bin.
One then creates invariant mass plots for all of these combinations in all the transverse momentum bins. All these invariant mass plots are then analysed and fitted. The Signal, Background, Signal over Background and Significance are then stored. Using the data from all these fits one can select the combination of topological cuts given an optimised S, S/B or significance.

[5]One cannot optimise all 16 variables in the time one has for its bachelor thesis. Cut optimisation is a process which costs a lot of time and computing power, therefore one usually optimises only a couple of the variables. Besides that some cutting variables are more powerful than others.

[6]Tighter cutting variables means the variables are chosen in such a way that more background is removed. However, in doing so also some signal is lost. Looser cutting variables have opposite effect, they allow for more background and signal. This however leads to a less pronounced Gaussian signal or even no signal at all

4.4 Systematic uncertainties

A measurement performed by any detector is never without uncertainty. Even if one could have access to such a large amount of data making the statistical uncertainty of a measurement negligible, there would still be a certain amount of uncertainty due to the detector itself and due to the analysis method. For our analysis various sources of uncertainty connected to the ALICE detector, the Q-vector construction, the track selection criteria and the analysis method will be considered. The analysis will be repeated with variations in the extraction of the signal from the invariant mass plots and the directed flow plots to check the stability of the simultaneous fit. The stability of the chosen cutting variables is also checked by repeating the analysis with both tighter and looser cutting variables. The influence of the polarity of the magnetic field will be considered as well as the uncertainty in the Q-vector x and y component from the ZDC's. Finally the effect of the p_{T} dependence of the efficiencies[7] of the D^{*+} mesons was taken into consideration.

4.5 ZDC calibration

As mentioned before, the Q-vectors built using data from the ZDC detectors must be re-centred. This process has been done for the data-set we use for this analysis. However, in order to perform this analysis using the data of the 2018 lead-lead run the re-centring of the Q-Vectors needs to be repeated for this data-set as well. A new framework was constructed to perform these calibrations, so they could easily be repeated for future runs. The same steps were taken as in [17], nevertheless will they be briefly explained below.

The calibration of the Q-vectors is done in two steps, gain equalisation and re-centring. For this thesis the focus was set on the re-centring. The first step in the re-centring is to compute the Q-vectors according to Eq. 4.1. Then the re-centring is performed by computing the average of a component and subtracting that from the corresponding Q-vector:

$$Q_{x,y}^{A',C'} = Q_{x,y}^{A,C} - \langle Q_{x,y}^{A,C} \rangle, \tag{4.10}$$

in which A and C stand for the two ZDC detectors. It was found in the re-centring of the 2015 data a strong dependence on run number, centrality and vertex position was found for all components as well as some correlation between them all. Besides that we have a limited amount of statistics to our disposal. Therefore the re-centring is chosen to be performed in three steps:

1. re-centre as a function of centrality (1% intervals) and run number.
2. re-centre as a function of centrality (5% intervals) and vertex positions (v_x, v_y and. v_z)
3. re-centre as a function of vertex positions (v_x, v_y and v_z).

[7] Efficiencies are a measure of the ability of ALICE and of our track selection settings and topological cuts to detect particles. If these efficiencies are not uniform with respect to a variable like transverse momentum a correction can be applied for this.

Since there is a run-dependent variation of the collision vertex position, the vertex positions are re-centred around zero for each run:

$$v_i \longrightarrow v_i - \langle v_i \rangle_{run}. \tag{4.11}$$

The re-centring is performed by running over the data multiple times. In the first run one computes the Q-vectors and the averages needed for step 1 of the re-centring (centrality and run number). In the second run again the Q-vectors are computed and the averages needed for step 1 are computed. Then using the averages from the first run the Q-vectors are re-centred with respect to centrality and run number. These re-centred Q-vectors are then used to compute the averages needed for step 2 of the re-centring(centrality and vertex position). This process is repeated until all re-centring steps are performed.

4.6 Analysis framework of the ALICE collaboration

As one can imagine, analyses as described in this Chapter cannot be performed using one computer with excel. The analyses performed for the ALICE collaboration all have a similar structure and they are written in the same programming language. In this section first the the framework for the codes, Root and Aliroot, will be discussed. Then a short overview of the structure of an analysis code will be given. Finally the grid, all combined computing power of CERN and the ALICE collaboration, will be discussed.

4.6.1 ROOT and AliRoot

All four major collaborations at cern (ATLAS, CMS, LHCb and ALICE) use the same data analysis framework, ROOT. ROOT is a framework for processing data used in high energy physics. It is based on the programming language C++ and makes use of Object Oriented Programming. It offers many pre-built classes often used in data analysis such as Histograms, Functions and Graphs and the tools to visualise these. AliRoot is the extension of ROOT containing specific classes used in the ALICE collaboration.[80]

4.6.2 Building an Analysis Task

To perform an entire analysis often multiple codes are needed to get to the final results. In general, two types of code are mainly used in a data-analysis. To perform smaller tasks that do not require a lot of computing power macros are used. A macro is a code with a .C extension that can be run locally on a computer or laptop. It is used to perform tasks that do not require to analyse the data directly from the ALICE detector such as performing an invariant mass fit or to determine the directed flow. The second type of code is an analysis task and these are used to process the data from the ALICE detector. These tasks must process a lot of data and this takes an immense amount of computing power. They therefor are ran on the grid, which will be discussed later on. These analysis tasks are used to create the invariant mass plots or to construct the Q-vectors which then can be further analysed using macros.

Analysis tasks are divided into three categories of code:

1. AnalysisTask.h: This is the header file of the analysis task. The header file contains the prototypes of functions and it contains the definitions of all the class members used in the analysis task.

2. AnalysisTask.cxx: This is the implementation file of the analysis task. It is the core of the task and contains the code needed to perform the analysis.

3. AddTask.C: This is a macro used to configure the task and to define the input and output. This macro is built following a certain convention to be able to run the analysis task on the grid.

All the codes used within the ALICE collaboration are bundled into AliPhysics. AliPhysics contains all the Analysis Tasks and macros approved by the collaboration. All AliPhysics codes can be found in the GitHub repository, which is used to monitor updates to the codes. Updates to existing tasks (or entirely new tasks) have to be tested thoroughly before they can be committed to the AliPhysics libraries.[81]

4.6.3 Running the Analysis Task

The analysis tasks process large amounts of data and require immense amounts of computing power. If one would want to perform the analysis on its own computer each analysis would take a couple of months. To tackle this problem the ALICE collaboration makes use of the LHC computing grid (Also called the grid). The grid contains computing centres all over the world that can be used to process and store data for members of the ALICE collaboration.

There are three modes of running an analysis task: local, private jobs and the Lego trains. If the analysis is run locally, a small amount of data is downloaded and processed locally on the computer. This is done to test the code and to check if additions or changes applied to the code do not yield errors and to check if everything is running smoothly. The next step often is to run the code in private jobs on the grid. The analysis can then be performed over a subset of all the runs from a certain data set (example given 2015 Pb–Pb). The analysis is split up into small packages and sent to different computing centres to reduces the time needed to perform the analysis. This mode is chosen for more thorough testing of the adapted or new code. In both local mode and in private jobs it is possible to run an analysis not present in the AliPhysics library. The third mode for running the analysis task is by using the LEGO train system. The LEGO train system is used to perform analysis over full data-sets. This is the standard way of running the analysis and it is done by setting up so called wagons that contain your analysis task. These wagons can then be attached to a certain data set (train) and when ready be analysed. This is done by train operators, which monitor the wagons and make sure everything is running smoothly. In order to use the LEGO train system the analysis task must be part of AliPhysics. The advantage of using the LEGO trains is that the computing resources of the grid can be used more efficiently.[81]

Chapter 5

Results

In this chapter the results of the performed analysis are presented. First the results on the charge dependent directed flow analysis of D^{*+} and D^{*-} mesons are presented. Afterwards the most recent results on the re-centring of the ZDC Q-vectors will be presented. For both the directed flow measurement and the ZDC calibration new code had to be written, so each section starts with a description of the new code. Additional figures and pieces of code will be placed in the Appendices if necessary.

5.1 Charge-dependent directed flow of D^{*+}- and D^{*-}-mesons

The charge-dependent directed flow of the D^{*+} and D^{*-} was determined according to method described in Chapter 4. Before the results are presented an overview of the additions to the code used to perform the analysis will be given.
First the simultaneous fits were performed selecting the D^{*+} and D^{*-} mesons using the topological cuts that were optimised for the nuclear modification factor analysis in the $30\% - 50\%$ centrality region. In the next part of the analysis these cuts were optimised and, using these optimised set of cuts, the analysis was repeated. The best set of cuts, leading to the smallest statistical error was chosen as our final set of cuts. In addition some test were performed to analyse the acceptance of the ALICE detector in the large η region for the soft-pions. Finally the systematic uncertainties for this analysis were determined leading to our final results.

5.1.1 Additions to the AliPhysics library

In order to perform the charge dependent directed flow analysis for D^{*+} and D^{*-} mesons the existing code from the AliPhysics library had to be updated. In the original code it was not possible to select either the D^{*+} or the D^{*-} meson candidates, but only to select them both at once. A selection was applied based on the charge of the soft-pion. If the soft-pion of the meson candidate had a positive charge the candidate was labelled as a D^{*+} meson and if the soft-pion had a negative charge it was labelled a D^{*-} meson. This information was stored, together with the other information like the invariant mass or the η bin, in a

```
if(fDecChannel==2){
        //D* -- Robert,Yifei, Alessandro
        nmasses=1;
        masses=new Float_t[nmasses];
        masses[0]=((AliAODRecoCascadeHF*)d)->DeltaInvMass();
}
```

```
if(fDecChannel==2){
        //D* -- Robert,Yifei, Alessandro
        nmasses=2;
        masses=new Float_t[nmasses];
        if(((AliAODRecoCascadeHF*)d)->GetBachelor()->Charge() > 0){
         masses[0]=((AliAODRecoCascadeHF*)d)->DeltaInvMass();
        }
        if(((AliAODRecoCascadeHF*)d)->GetBachelor()->Charge() < 0){
         masses[1]=((AliAODRecoCascadeHF*)d)->DeltaInvMass();
        }
}
```

```
if(fFlowMethod==kSP) {

        Double_t scalprod[2]={-2.,-2.};
        scalprod[0] = TMath::Cos(fHarmonic*phiD)*QB[0]+TMath::Sin(fHarmonic*phiD)*QB[1];
        Double_t sparsearray[5] = {scalprod[0], masses[0], ptD, etaD, 0.5};

        ((THnSparseD*)fOutput->FindObject(Form("hMassScalProduQA_centr%d_%d",icentrmin,icentr)))->Fill(sparsearray);
.....
  }
  else {
    ((TH2F*)fOutput->FindObject(Form("hMc2deltaphi_pt%dcentr%d_%d",ptbin,icentrmin,icentr)))->Fill(TMath::Cos(fHarmonic*deltaphi),masses[0]);
.....
  }
  ((TH2F*)fOutput -> FindObject(Form("hMPtCandcentr%d_%d", icentrmin, icentr))) -> Fill(d->Pt(),masses[0]);
```

```
if(((AliAODRecoCascadeHF*)d)->GetBachelor()->Charge() > 0){
  if(fFlowMethod==kSP) {
    massDstar_or_Dstarbar = kmassDstar;
        Double_t scalprod[2]={-2.,-2.};
        scalprod[0] = TMath::Cos(fHarmonic*phiD)*QB[0]+TMath::Sin(fHarmonic*phiD)*QB[1];
        Double_t sparsearray[6] = {scalprod[0], masses[0], ptD, etaD, 0.5, static_cast<double>(massDstar_or_Dstarbar)};
        ((THnSparseD*)fOutput->FindObject(Form("hMassScalProduQA_centr%d_%d",icentrmin,icentr)))->Fill(sparsearray);
.....
  }
  else {
    ((TH2F*)fOutput->FindObject(Form("hMc2deltaphi_pt%dcentr%d_%d",ptbin,icentrmin,icentr)))->Fill(TMath::Cos(fHarmonic*deltaphi),masses[0]);
.....
  }
  ((TH2F*)fOutput -> FindObject(Form("hMPtCandcentr%d_%d", icentrmin, icentr))) -> Fill(d->Pt(),masses[0]);
}
if(((AliAODRecoCascadeHF*)d)->GetBachelor()->Charge() < 0){
  if(fFlowMethod==kSP) {
    massDstar_or_Dstarbar = kmassDstarbar;
        Double_t scalprod[2]={-2.,-2.};
        scalprod[0] = TMath::Cos(fHarmonic*phiD)*QB[0]+TMath::Sin(fHarmonic*phiD)*QB[1];
        Double_t sparsearray[6] = {scalprod[0],masses[1],ptD,etaD,1.5,static_cast<double>(massDstar_or_Dstarbar)};
        ((THnSparseD*)fOutput->FindObject(Form("hMassScalProduQA_centr%d_%d",icentrmin,icentr)))->Fill(sparsearray);
.....
  }
  else{
        ((TH2F*)fOutput -> FindObject(Form("hMc2deltaphi_pt%dcentr%d_%d",ptbin,icentrmin,icentr)))->Fill(TMath::Cos(fHarmonic*deltaphi),masses[1]);
.....
  }
  ((TH2F*)fOutput->FindObject(Form("hMPtCandcentr%d_%d",icentrmin,icentr)))->Fill(d->Pt(),masses[2]);
}
```

Figure 5.1: The changes in applied to the AliPhysics code. The top part shows the adaptions (on the right) to the original (on the left) function calculating the invariant mass and the bottom part shows the adaption to the function filling the D^{*+} and D^{*-} multi-dimensional histograms. The lines of code highlighted in red were removed and the lines of code highlighted in green were added to the code.

multi-dimensional histogram. This gives us the ability to extract this information later on in the analysis. This selection was applied twice in the code, once during the calculation of the invariant masses and once during the filling of the multi-dimensional histograms. In Fig. 5.1 the differences between in the old code and the new code is shown.[1] These additions to the code were thoroughly tested and a presentation showing the effects was given to the ALICE wide D2H research group. The code was then committed to the AliPhysics library on GitHub and approved. The code with the additions is now the standard code in AliPhysics.

[1] A lot of complicated classes and names are used in the code. In the appendix I show which codes I've used to perform the analysis. Besides that AliRoot has an extensive online documentation, so using these you can figure out exactly how the code works.

5.1.2 Simultaneous fits

The odd component of the directed flow of each D^{*+} and D^{*-} candidate was determined using the scalar product method. The directed flow was plotted as a function of invariant mass and an invariant mass plot was created for the D^{*+} and D^{*-} candidates in four pseudorapidity intervals ($-0.8 < \eta < -0.4, -0.4 < \eta < 0, 0 < \eta < 0.4$ and $0.4 < \eta < 0.8$.). The directed flow of the D^{*+} and D^{*-} mesons was then determined by performing a simultaneous fit. This was done in two transverse momentum intervals: $3 < p_T < 6\,\mathrm{GeV}/c$ and $3 < p_T < 36\,\mathrm{GeV}/c$. In Fig. 5.2 the simultaneous fits for the D^{*+} meson in the $3 < p_T < 36\,\mathrm{GeV}/c$ region and in all four η bins is shown. The topological selection criteria used for filtering out the candidate mesons can be found in a table in appendix A. As can be seen in the bottom panel of all four figures in Fig. 5.2 a larger bin width was chosen in the v_1 versus invariant mass plot for smaller and larger invariant masses than the D^{*+} mass-peak. This was done to stabilise the fluctuations in the background signal. In the range of the mass peak a finer binning was chosen to allow the effect of the D^{*+} mesons on the directed flow to be seen. In table 5.1 and table 5.2 the results for both the D^{*+} and the D^{*-} mesons in the low and high transverse momentum intervals are reported respectively. The simultaneous fit figures of the D^{*+} meson in the high transverse momentum region and of the D^{*-} meson in both transverse momentum regions can be found in appendix C.

Table 5.1: The directed flow values of D^{*+}-meson and D^{*-}-meson in the transverse momentum region $3 < p_T < 6\,\mathrm{GeV}/c$ including statistical errors.

$3 < p_T < 6\,\mathrm{GeV}/c$	D^{*+}-meson	D^{*-}-meson
$-0.8 < \eta < -0.4$	0.094 ± 0.264	0.101 ± 0.392
$-0.4 < \eta < 0$	-0.198 ± 0.271	0.063 ± 0.312
$0 < \eta < 0.4$	-0.084 ± 0.345	-0.257 ± 0.271
$0.4 < \eta < 0.8$	0.062 ± 0.323	0.101 ± 0.252

Table 5.2: The directed flow values of D^{*+}-meson and D^{*-}-meson in the transverse momentum region $3 < p_T < 36\,\mathrm{GeV}/c$ including statistical errors.

$3 < p_T < 36\,\mathrm{GeV}/c$	D^{*+}-meson	D^{*-}-meson
$-0.8 < \eta < -0.4$	-0.011 ± 0.178	-0.056 ± 0.217
$-0.4 < \eta < 0$	-0.036 ± 0.178	0.020 ± 0.162
$0 < \eta < 0.4$	-0.043 ± 0.170	-0.299 ± 0.166
$0.4 < \eta < 0.8$	-0.133 ± 0.184	0.132 ± 0.158

In order to reduce the amount of statistical uncertainty in the measurement an attempt was made to optimise the cuts used for the analysis. The results of the cut optimisation process will be discussed in the next section.

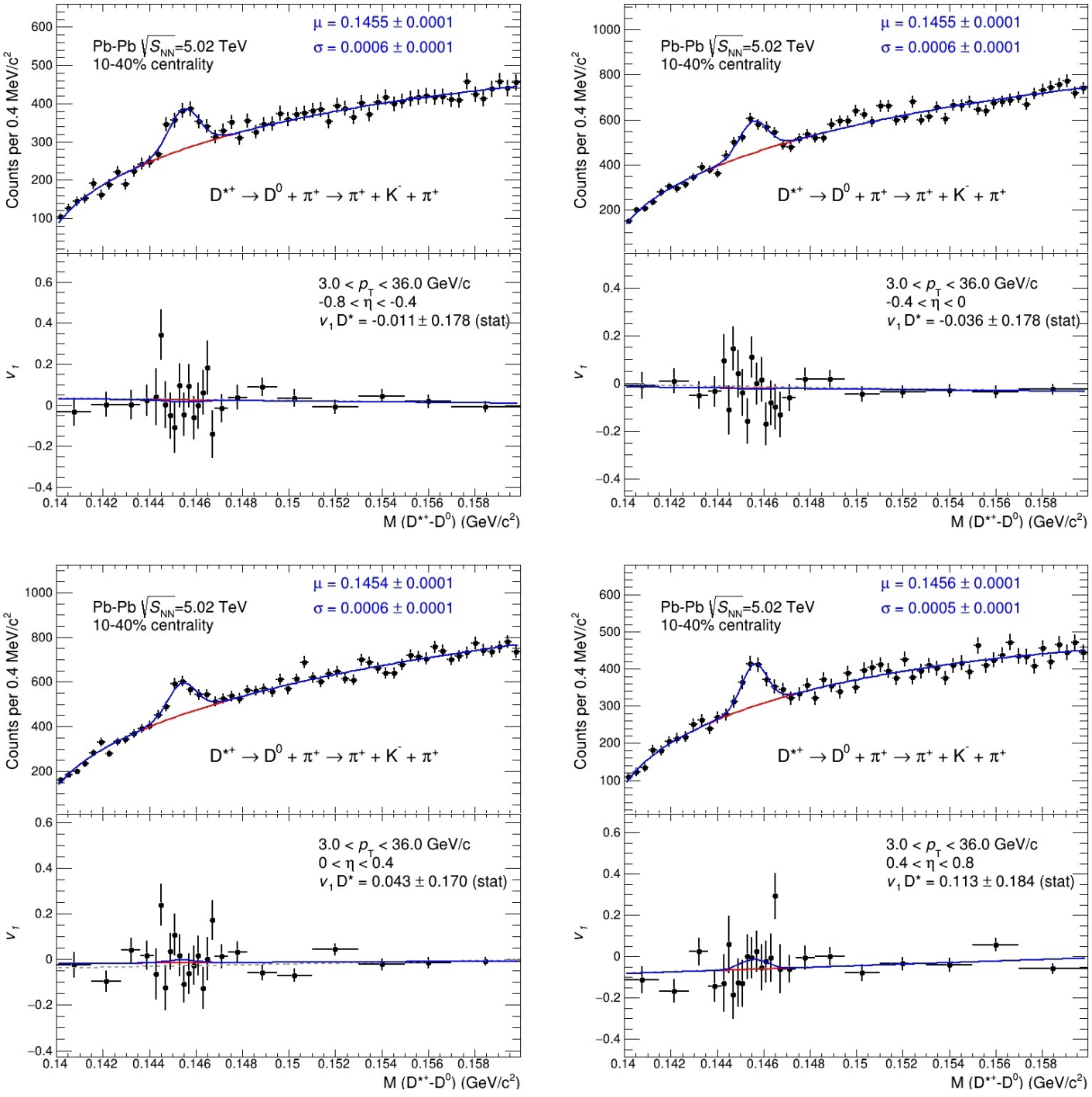

Figure 5.2: Simultaneous fits for the D^{*+} meson in the transverse momentum region $3 < p_T < 36\,\mathrm{GeV}/c$. The top left figure is the $-0.8 < \eta < -0.4$ bin, the top left figure is the $-0.4 < \eta < -0.0$ bin, the bottom left figure is the $0 < \eta < 0.4$ bin and the bottom right figure is the $0.4 < \eta < 0.8$ bin. The red line in the figures corresponds to the background and the blue line in the figures corresponds to the background plus signal. In the bottom panel of some of the figures one can see a grey dashed line. This line shows the background signal from the pre-fit.

5.1.3 Cut optimisation

The criteria based on the decay topology of the D^{*+} meson, used for selecting the D^{*+} mesons out of the data, were optimised using the process of cut optimisation as described in the analysis methods. The cutting variables optimised in this analysis are: the distance of closest approach (DCA), the product of the impact parameters (d0d0), the cosine of the theta star angle ($\cos\theta*$), the cosine of the pointing angle ($\cos\theta_p$) and the normalised decay length (NormDec). Since the original cutting parameters were used for an analysis in the 30%-50% centrality region, the expectation is the optimal values for the cutting parameters are more tight than the original ones. Therefore the choice was made to find the optimal value for these five parameters in interval between the original value and a tighter value.

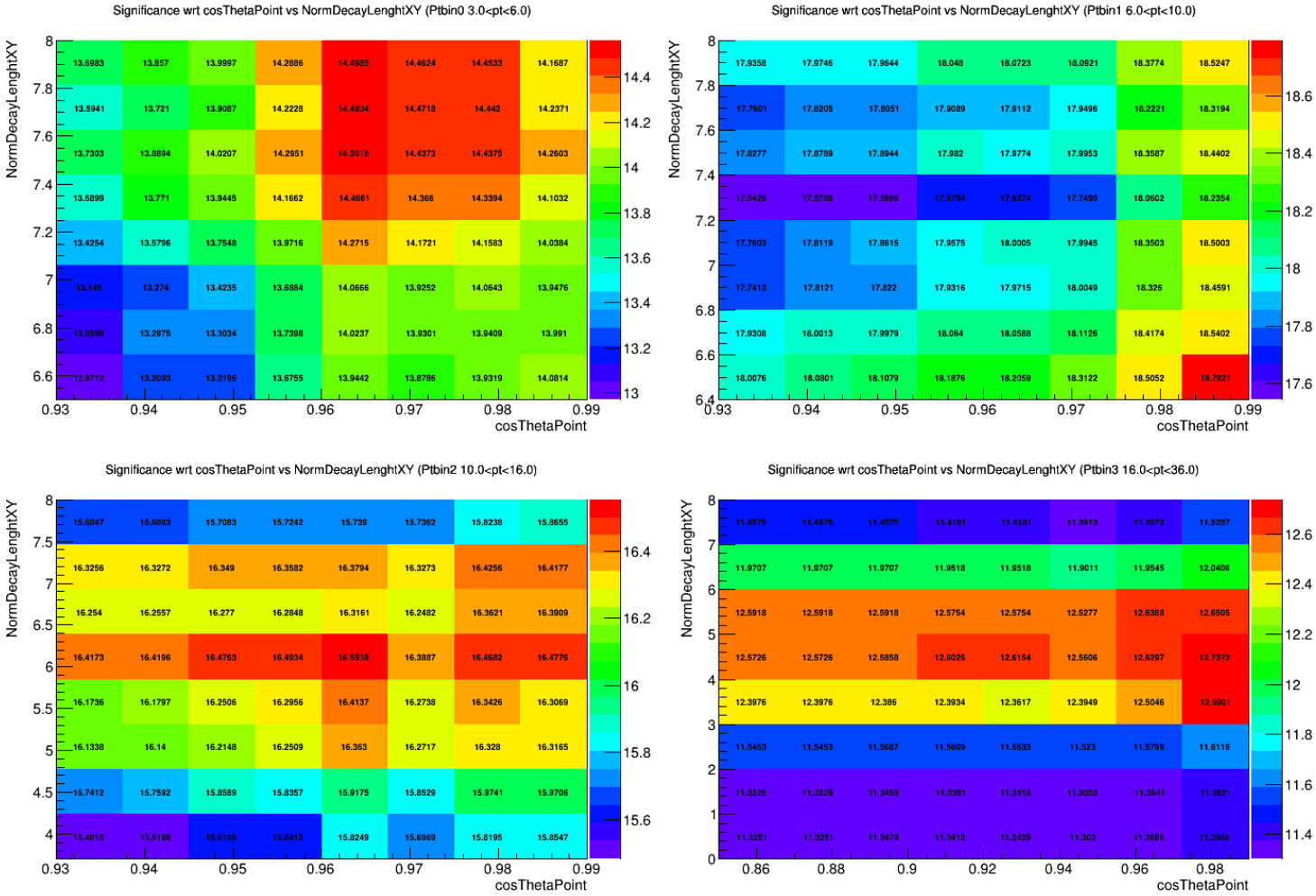

Figure 5.3: Heat-maps showing the significance of the invariant mass plots created using varied values for the $\cos\theta_{point}$ and the Norm L_{XY} in each transverse momentum bin ([3-6], [6-10], [10-16], [16-24] and [24-36] in GeV/c). On the right of each heat map the legend for that specific figure is shown.

Table 5.3: The list of starting values and tighter values for the optimisation of the parameters in all transverse momentum bins.

p_{T} (GeV/c)/variable	[3-6]	[6-10]	[10-16]	[16-36]	Tighter value
DCA	0.022	0.021	0.021	0.021	0.017
$\cos\theta^*$	0.8	1	1	1	0.5
d_0d_0	-0.0003	-0.0001	-7.5e-05	0.0004	-0.0005
$\cos\theta_{point}$	0.93	0.93	0.93	0.85	0.99
Norm L_{XY}	6.5	6.4	3.7	0	8

In order to reduce computation time a coarser transverse momentum binning was chosen with respect to the original binning. The transverse momentum bins in which the optimisation took place were [3-6], [6-10], [10-16], [16-24] and [24-36] in GeV/c. The starting value of the parameters in the new transverse momentum binning was chosen as follows: The value of a parameter in the transverse momentum bin in the centre of the coarser binning intervals was taken as the starting value. For instance the starting value for the [3-6] p_{T} bin was the value from the [4-5] p_{T} bin. For all five variables the tighter value chosen, independent of the transverse momentum bin, are reported in Table 5.3. As described in the analysis methods the difference between the original value and tighter value of each parameter is divided into 8 steps and for each possible combination of variations a set of cuts is created. For each set of cuts an invariant mass plot is created and fitted. From these fits the signal, background and significance is determined and stored to select the combination of parameters with the optimal value.

In Fig. 5.3 the effect of varying the normalised decay length and the cosine of the pointing angle on the significance is presented in all transverse momentum bins using a heat-map. The colour of each block in the eight by eight heat-map corresponds to the significance of that combination of those two parameters. The value of the other 3 parameters not represented in the heat-map are automatically set to the optimal value. These heat-maps are created for all possible combinations of parameters that were varied. Not only heat-maps showing the significance of the combinations can be created, but also the background, signal and signal over background can be presented using these heat-maps. From these heat-maps the optimal value for the parameters can be chosen and the effects of varying the parameters on e.g. the significance in every transverse momentum bin could be checked. The invariant mass plots and their fits corresponding to the optimal set of parameters were checked on validity. No

Table 5.4: Original and optimised values for the DCA, reported in centimetres

p_{T} (GeV/c)\DCA	Original	Significance	Signal
[3-6]	0.022	0.0201	0.0214
[6-10]	0.021	0.0185	0.0205
[10-16]	0.021	0.018	0.019
[16-36]	0.021	0.0181	0.0174

abnormalities were found. Two sets of cuts were created using the results of the cut optimisation process. One of the cuts used parameter values producing invariant mass plots with the highest signal. The other set of cuts used parameter values producing invariant mass plots with the highest significance. In table 5.4 the new values for the DCA are presented side by side with the old ones. For the other parameters the optimised values can be found in appendix B2.

The directed flow analysis was repeated in the same way using the two new sets of cuts. The simultaneous fits of the two new analyses were compared with the first analysis to see which set of cuts would yield the smallest statistical errors on the measurement. In Fig. 5.5 the simultaneous fits of the D^{*-} meson in the $3 < p_T < 6\,\mathrm{GeV}/c$ and the D^{*+} meson in the $3 < p_T < 36\,\mathrm{GeV}/c$ both in the $0.4 < \eta < 0.8$ bin of the original measurement and of the two analyses using the optimised sets of cuts are presented. The statistical errors of the analysis using the cuts optimised for an optimal significance were comparable to the statistical errors in the original measurement, however the statistical errors of the analysis using the cuts optimised for an optimal signal were larger than the statistical errors in the original measurement. Since there was no significant improvement in the statistical errors the set of cuts used for the first analysis were used as our final result. The optimised sets of cuts were used in determining the systematic errors on the analysis.

5.1.4 Soft-pion efficiencies

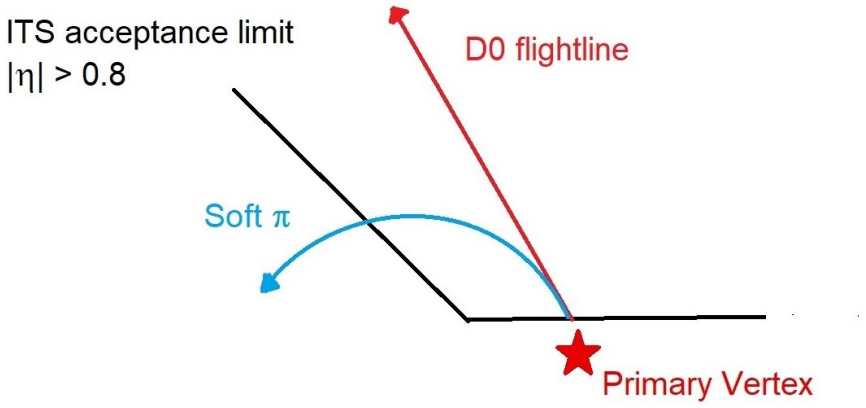

Figure 5.4: A sketch of the decay of a D^{*+} meson produced at the primary vertex, showing the D^0 flight line in red and the π_s flight line in blue. The π_s flies outside the acceptance of the ITS-detector.

An additional check was performed on the efficiency of the ALICE detector in measuring soft-pions in the high η regions. Compared to the D^0 meson, the π_s has a low transverse momentum. If a D^{*+} meson is produced in the direction of the edge of the detector, the created π_s could travel outside the acceptance of the ALICE detector. A sketch of situation is shown in Fig. 5.4. This could lead to a significant deviation in the number of detected

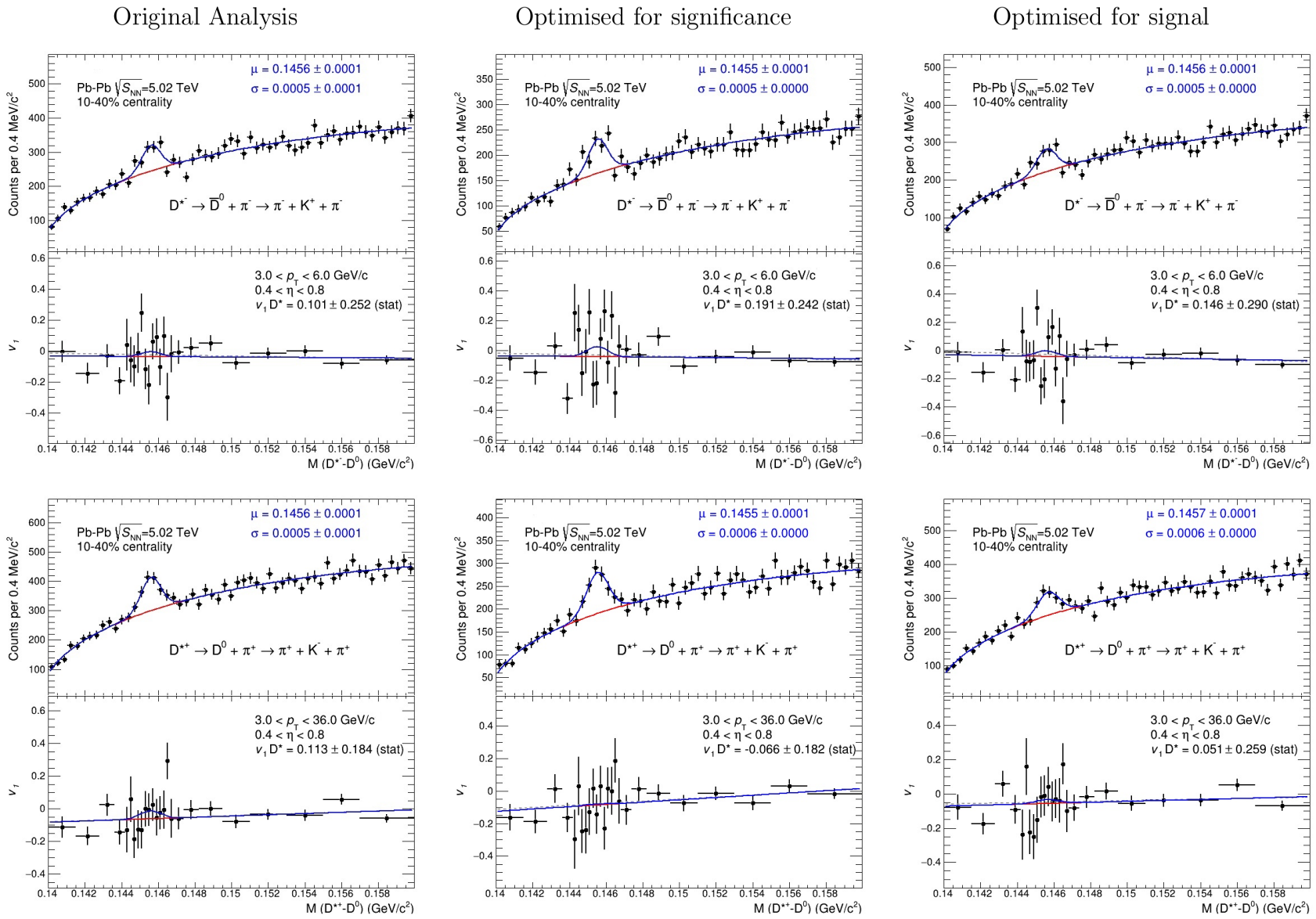

Figure 5.5: A comparison of the simultaneous fits of the original analysis with the analyses using the optimised sets of cuts. The top row corresponds to the D^{*-} meson in the $3 < p_T < 6\,\mathrm{GeV}/c$ region and the bottom row corresponds to the D^{*+} meson in the $3 < p_T < 36\,\mathrm{GeV}/c$ region. Boths rows show data from the $0.4 < \eta < 0.8$ pseudorapidity bin. The left column contains the simultaneous fits from the original analysis, the centre column from the significance optimised analysis and the right column from the signal optimised analysis.

D^{*+} mesons in the outer pseudorapidity bins ($0.8 < |\eta| < 0.4$) with respect to inner pseudorapidity bins ($0.4 < |\eta| < 0$). If such a difference would be present a correction should be applied to compensate for this effect. In short the efficiency calculates the fraction of particles one detects with respect to the total number of particles produced in a collision. Since this procedure demands a tremendous amount of computing time, these analyses are performed using data from Monte-Carlo simulations of Pb–Pb collisions. A distinction can be made between D^{*+} mesons produced directly from Charm quarks and D^{*+} mesons produced in the decay of Beauty quarks, called the Charm and Beauty fraction respectively.

In Fig. 5.6 the results of the efficiencies are presented. The efficiencies for the Beauty fraction show a strong pseudorapidity dependence after applying the selection of the number of ITS clusters required. The efficiency is significantly lower in the outer pseudorapidity bins compared to the inner bins. The charm fraction shows a dependency on pseudorapidity as well. However the efficiency is higher in the outer pseudorapidity bins. After applying the topological cuts, the efficiency of the Beauty fraction is flattened out. No significant pseudorapidity dependence is detected. The pseudorapidity dependence of the Charm fraction does remains the same. The outer pseudorapidity bins have a higher efficiency than the inner bins. Even though a pseudorapidity dependence was found in the efficiencies, it was decided not to correct for this effect.

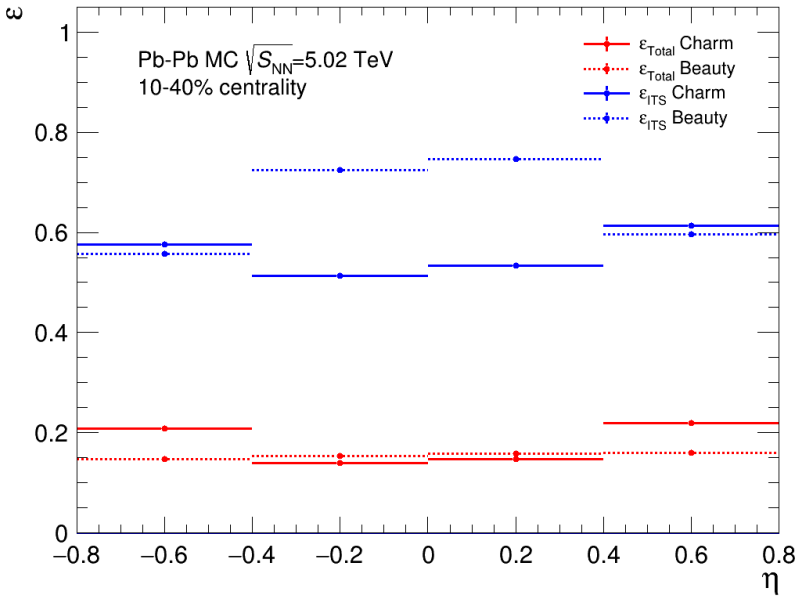

Figure 5.6: The efficiencies for D^{*+} mesons originating from Charm quarks (solid line) and from the decay of Beauty quarks (dashed line). The efficiencies were calculated for the detected particles after applying the selection on the number of ITS clusters (blue) and after applying the topological cuts (red)

5.1.5 Systematic uncertainties

The systematic uncertainties on the performed measurement were determined by considering various sources which could contribute to a systematic deviation. The results for the contribution of the signal extraction methods and the cut variation process to the total systematic uncertainty are presented below. Because of the poor statistics compared to the D^0 analysis the contribution to the total systematic error due to the influence of the polarity of the magnetic field, the uncertainty in the Q-vector x and y component from the ZDC's as well as the systematic uncertainty due to the p_T-dependence of the efficiencies will be taken from the directed flow measurement of the D^0 meson, as described in [15]. These contributions will be discussed at the end of this section, after which the total systematic uncertainty will be determined.

Signal extraction

To determine the signal extraction contribution the simultaneous fits were repeated varying a range of parameters in the fitting procedure. The signal extraction systematic considers the stability of the parameters used to perform the simultaneous fit. The effects of bin width of the invariant mass plot and of the directed flow plot were considered, the fit interval was varied and the background functions of the invariant mass plot and the directed flow plot were varied. The chosen background function variations for the invariant mass plot was a power function. The chosen variations for the directed flow background function were a zeroth and second degree polynomial. The simultaneous fits of all variations were checked and if it was clear the fit was not valid[2], than that result was not taken into account. For example the fit using a power background function in the $3 < p_T < 6\,\mathrm{GeV}/c$ momentum region and in the $0.4 < \eta < 0.8$ pseudorapidity bin for the D^{*-} meson clearly does not give a valid fit for both the directed flow plot as well as the invariant mass plot. This can be seen in Fig. 5.7. In appendix C.3 an example of the all variations are presented to clarify the effect each variation has on the simultaneous fit.

Table 5.5: The systematic uncertainties assigned to the directed flow D^{*+} mesons and D^{*-} mesons due to the signal extraction.

	D^{*+} meson	D^{*-} meson
$3 < p_T < 6\,\mathrm{GeV}/c$	0.005	0.005
$3 < p_T < 36\,\mathrm{GeV}/c$	0.0025	0.0025

As a means to determine the contribution of the signal extraction to the total systematic uncertainty, the difference between the measured value of the directed flow in the original measurement and in the variation is taken. The root mean square (RMS) is then taken of all the variations and scaled to the value of the directed flow. In this analysis a directed flow value of 0.1 was chosen as reference used to scale the contributions to the total systematic

[2]There are several reasons to declare a fit invalid. For example a fit is not valid if the significance of the invariant mass is lower than 3 or if the fit clearly fits a statistical fluctuation.

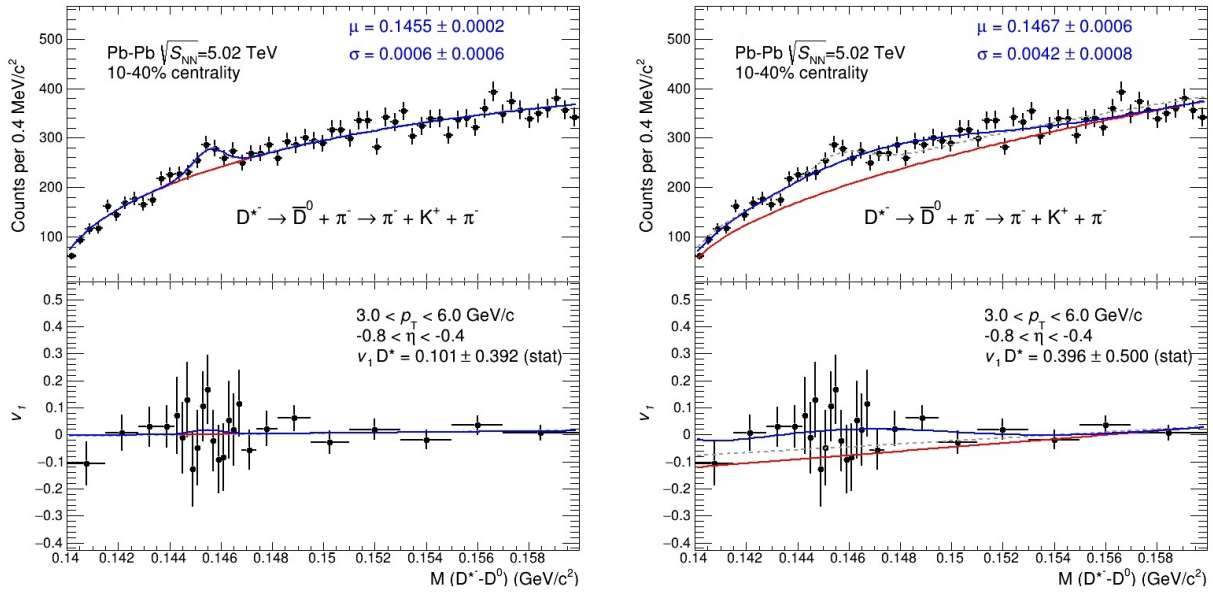

Figure 5.7: Comparison of the simultaneous fit using a power function as background function for the mass plot (right figure) and the original simultaneous fit using Eq. 4.4 as background function for the mass plot (left figure). The transverse momentum and pseudorapidity bins are $3 < p_{\mathrm{T}} < 6\,\mathrm{GeV}/c$ and $0.4 < \eta < 0.8$ respectively and the analysed particle is a D^{*-} meson.

uncertainty to. In the left panel of Fig. 5.8 the results for the signal extraction are presented for the D^{*+} meson in the $3 < p_{\mathrm{T}} < 36\,\mathrm{GeV}/c$ region. The top panel shows the results of all the variations of the simultaneous fits. The bottom panel shows the difference between the value of the directed flow of the variation with the original value. The RMS of the variations is shown as a coloured bar in the bottom panel of the figure. The results for the other transverse momentum region and for the D^{*-} meson are presented in appendix C.3. The values for the systematic uncertainty assigned due to the signal extraction are reported in table 5.5

Table 5.6: Original, significance optimised and looser cut values for the DCA, reported in centimetres

p_{T} (GeV/c)\DCA	Original	Significance	Looser
[3-6]	0.022	0.0201	0.0238
[6-10]	0.021	0.0185	0.02375
[10-16]	0.021	0.018	0.024
[16-36]	0.021	0.0181	0.024

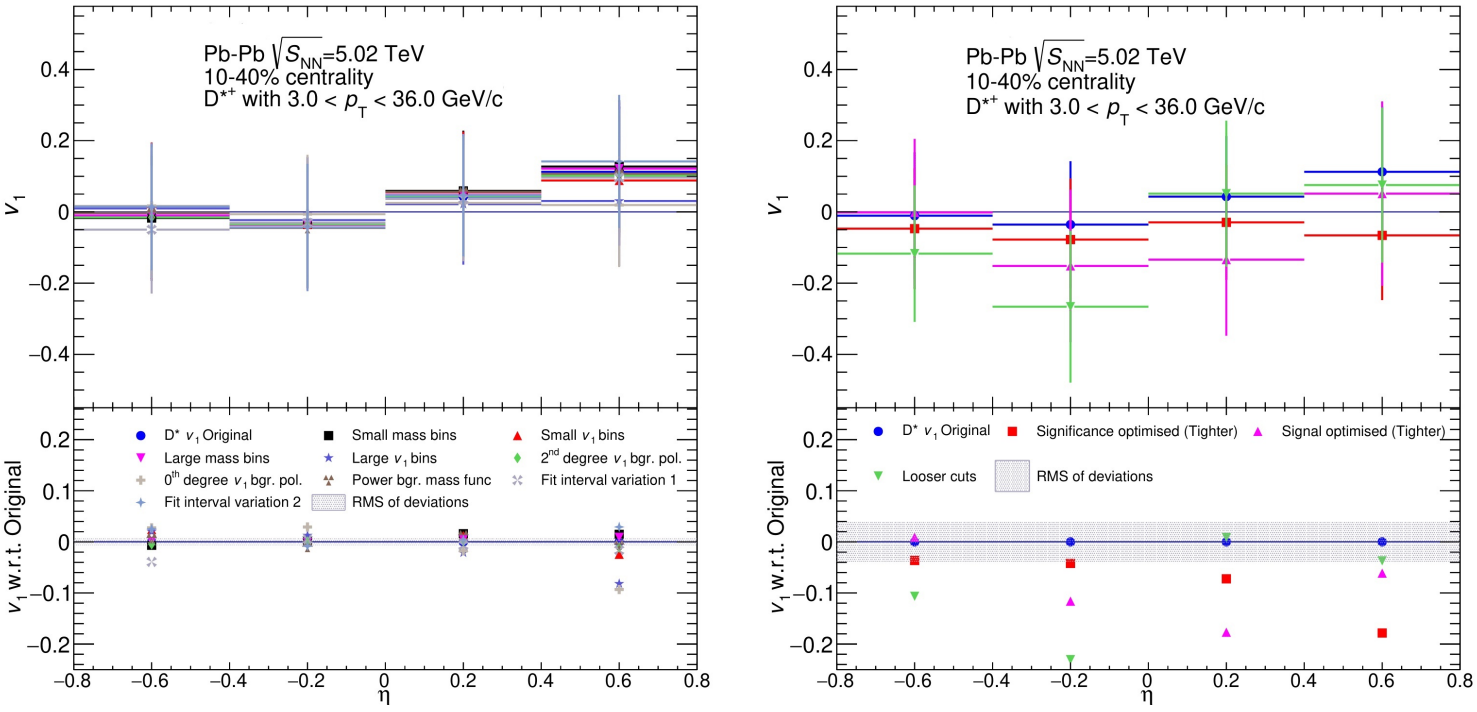

Figure 5.8: Directed flow values for the D^{*+} meson signal extraction (left panel) and cut variation (right panel) in the transverse momentum region $3 < p_T < 36\,\mathrm{GeV}/c^2$. The top part of the figure show the directed flow value for the variations and the bottom part of the figure shows the difference in directed flow of the variation with respect to the original value. The coloured band in the bottom panel is the contribution to the systematic uncertainty.

Cut variation

Another source of systematic uncertainty that was considered is the cut variation. With the cut variation the stability of the chosen topological cutting parameters is tested. The way the contribution of the cut variation was determined is analogous to the signal extraction. The analysis was repeated using three different sets of topological cuts, two sets of tighter cuts and one set of looser cuts. The two sets of tighter cuts are the two optimised cuts from the cut optimisation. The set of looser cuts was created in the following way: The cutting variables that were changed during the cut optimisation were set looser with the same amount as they were set tighter for the set of cuts optimised for significance. As an example the the variation in the DCA is presented in table 5.6.

The simultaneous fit results of the cut variation were all checked on the validity of the simultaneous fits, as was done for the signal extraction. Two simultaneous fits of the looser cut variation were not taken into account as the invariant mass fits did not yield proper fits. These two fits were both in the $3 < p_T < 6\,\mathrm{GeV}/c$ region. The D^{*+} simultaneous fit for $-0.8 < \eta < -0.4$ and the D^{*-} simultaneous fit for $0 < \eta < 0.4\,\mathrm{GeV}/c$. In Fig. 5.9 the simultaneous fits of both are presented. Both Gaussian signal peaks of the looser cut

Original

Looser cut

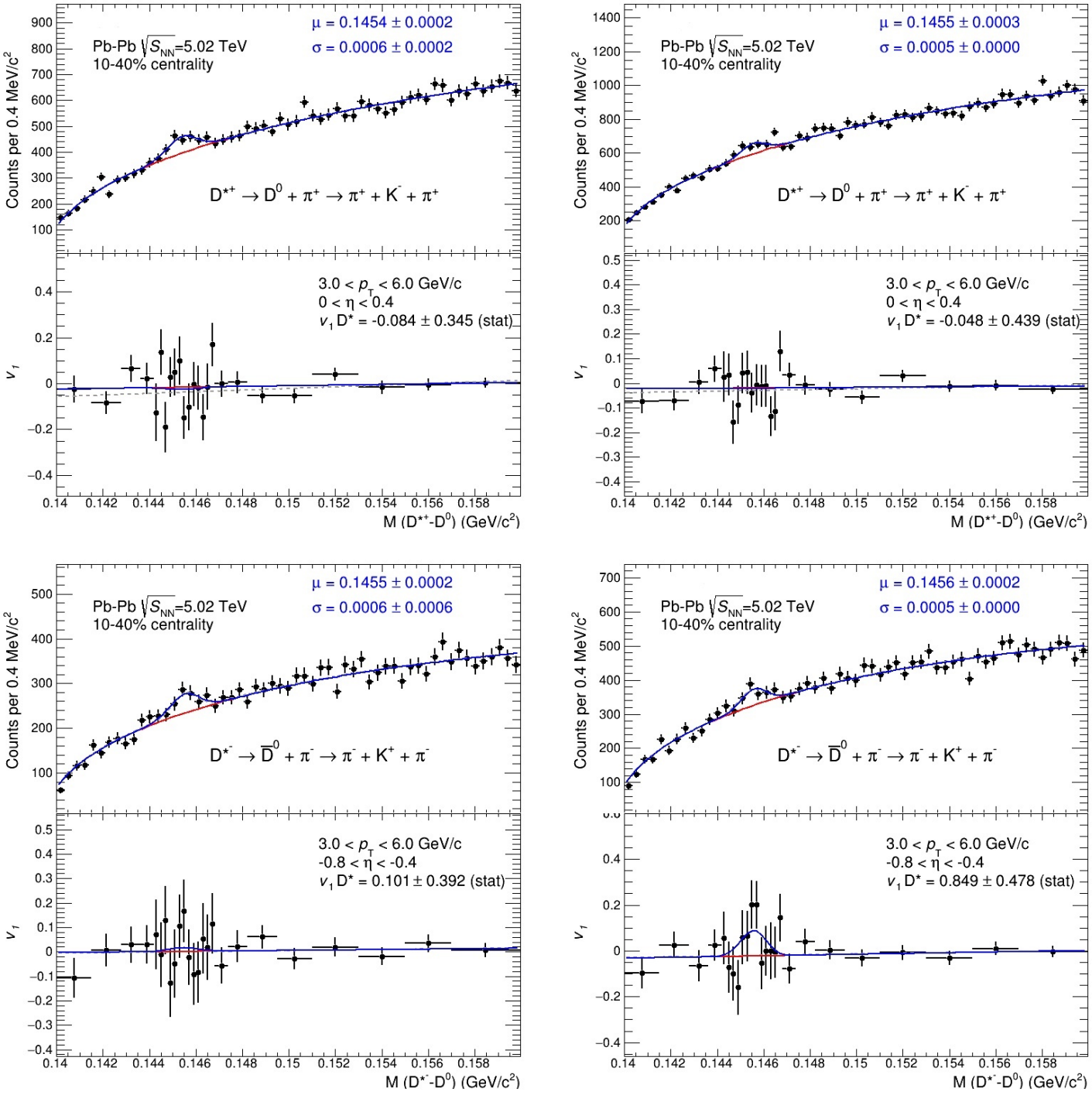

Figure 5.9: Comparison between the simultaneous fits of the original measurement (left figures) and the looser cut variation (right figures) that were not taken into account because of their poor invariant mass fits.

variation had a very low significance (lower than 3) and were largely governed by fluctuations. Furthermore, all invariant mass plots of the cut variations were fitted using a fixed peak width sigma corresponding to a Monte-Carlo analysis of the invariant mass plots of the original topological cuts. This was done to stabilise the invariant mass fits.

The contribution of the cut variation systematic was determined in the same manner as for the signal extraction. The directed flow of the variation was determined and plotted together with the original values in the top panel of the right figure of Fig. 5.8. In the bottom panel of the right figure the differences with respect to the original values are presented. The contribution to the total systematic uncertainty is again taken as the RMS of the differences scaled to a directed flow value of 0.1. As before this is plotted as a coloured bar in the lower panel. The values for the systematic uncertainty assigned due to the cut variation are reported in table 5.7

Table 5.7: The systematic uncertainties assigned to the directed flow D^{*+} mesons and D^{*-} mesons due to the cut variation.

	D^{*+} meson	D^{*-} meson
$3 < p_T < 6\,\mathrm{GeV}/c$	0.015	0.01
$3 < p_T < 36\,\mathrm{GeV}/c$	0.01	0.01

Polarity of the magnetic field

During the data-taking of the Pb–Pb collisions at $\sqrt{s} = 5.02$ TeV the polarity of the magnetic field was switched. The analysis for the D^0 measurement was repeated using only data with either a positive or negative polarity. It was observed that a clear hierarchy was present in the directed flow measurement of the D^0 mesons when comparing results of both polarities. The directed flow determined in the data with a negative polarity was higher than the directed flow measured during the positive polarity of the magnetic field. The directed flow determined using the full data was found to be in between the directed flow of the two separate analyses. Despite this clear hierarchy the results were within statistical uncertainty. It was decided to assign a systematical uncertainty due to this effect of 0.02 for the D^0 measurement, scaled to a directed flow value of 0.1. This value was also assigned in this analysis.

x and y components of the ZDC Q-vectors

The directed flow of the D^{*+} mesons was determined using Q-vectors built from data of the ZDC detectors, as in Eq. 4.2. There, however, is a residual asymmetry in the x-component and y-component of the Q-vectors after the ZDC re-centring. The systematic uncertainty due to this asymmetry was determined by calculating the directed flow using either only the x-component of y-component of the Q-vectors. A systematic uncertainty of 0.02, scaled to a

Table 5.8: The total systematic uncertainties assigned to the directed flow D^{*+} mesons and D^{*-} mesons.

	D^{*+} meson	D^{*-} meson
$3 < p_T < 6\,\mathrm{GeV}/c$	0.034	0.032
$3 < p_T < 36\,\mathrm{GeV}/c$	0.032	0.032

directed flow value of 0.1 was assigned in the D^0 analysis and will be assigned in this analysis as well.

p_T dependence of the D^{*+} efficiencies

It is well known that D-mesons efficiencies show a very strong transverse momentum dependency.[82] Applying corrections for this p_T dependence in the D^0 measurement yielded an increase in statistical uncertainty. No significant bias was found in the directed flow values. Therefor a systematical uncertainty was added of 0.01, scaled to a directed flow value of 0.1. This systematical uncertainty was also added in this analysis, since the D^{*+} meson a similar transverse momentum of the efficiencies.

Total systematic uncertainty

In determining the total systematic uncertainty on the directed flow measurement it was assumed all contributions are not correlated. Therefor all separate contributions were added in quadrature. The total assigned systematic uncertainty is reported in table 5.8.

5.1.6 Final results

In Fig. 5.10 the results for the odd component of the directed flow of the D^{*+} and D^{*-} mesons are presented as a function of pseudorapidity. Finally the difference in directed flow, Δv_1 was determined via Eq. 4.7 and fitted to linear function. The results are presented in Fig. 5.11. Both statistical and systematic uncertainties are propagated as not correlated for the Δv_1. The results for the slope of the linear fit are reported in table 5.9. Finally the results for Δv_1 for both transverse momentum regions are presented in Fig. 5.12 in one figure. The results hint towards a positive slope, however the statistical uncertainty in the measurement prevents a solid conclusion.

Table 5.9: The values for $\mathrm{d}\Delta v_1/\mathrm{d}\eta$ from the linear fits for $3 < p_T < 6\,\mathrm{GeV}/c$ and $3 < p_T < 36\,\mathrm{GeV}/c$.

	$3 < p_T < 6\,\mathrm{GeV}/c$	$3 < p_T < 36\,\mathrm{GeV}/c$
$\mathrm{d}\Delta v_1/\mathrm{d}\eta$	$0.09 \pm 0.49\,(\mathrm{stat.}) \pm 0.05\,(\mathrm{syst.})$	$0.07 \pm 0.29\,(\mathrm{stat.}) \pm 0.05\,(\mathrm{syst.})$

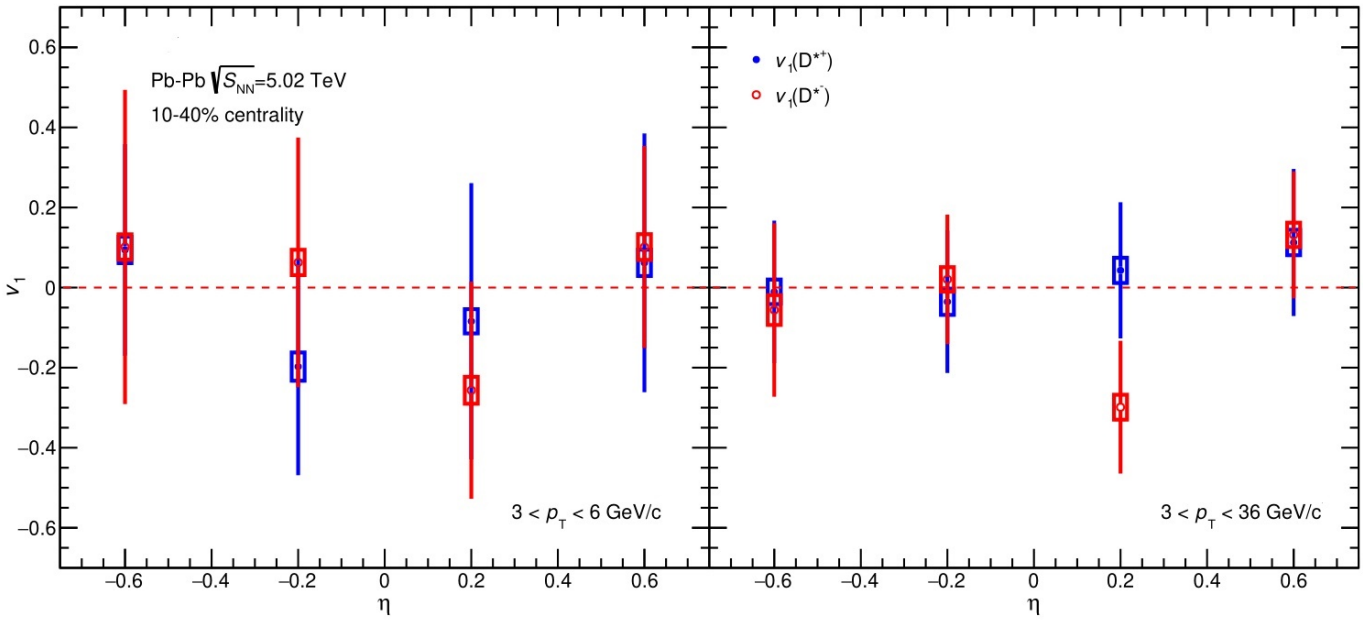

Figure 5.10: v_1 as a function of η for D^{*+} mesons (Blue) and D^{*-} mesons (Red) in $3 < p_T < 6\,\mathrm{GeV}/c$ (left panel) and $3 < p_T < 36\,\mathrm{GeV}/c$ (right panel). The box around the data points represent the systematic uncertainty and the vertical lines represent the statistical uncertainties.

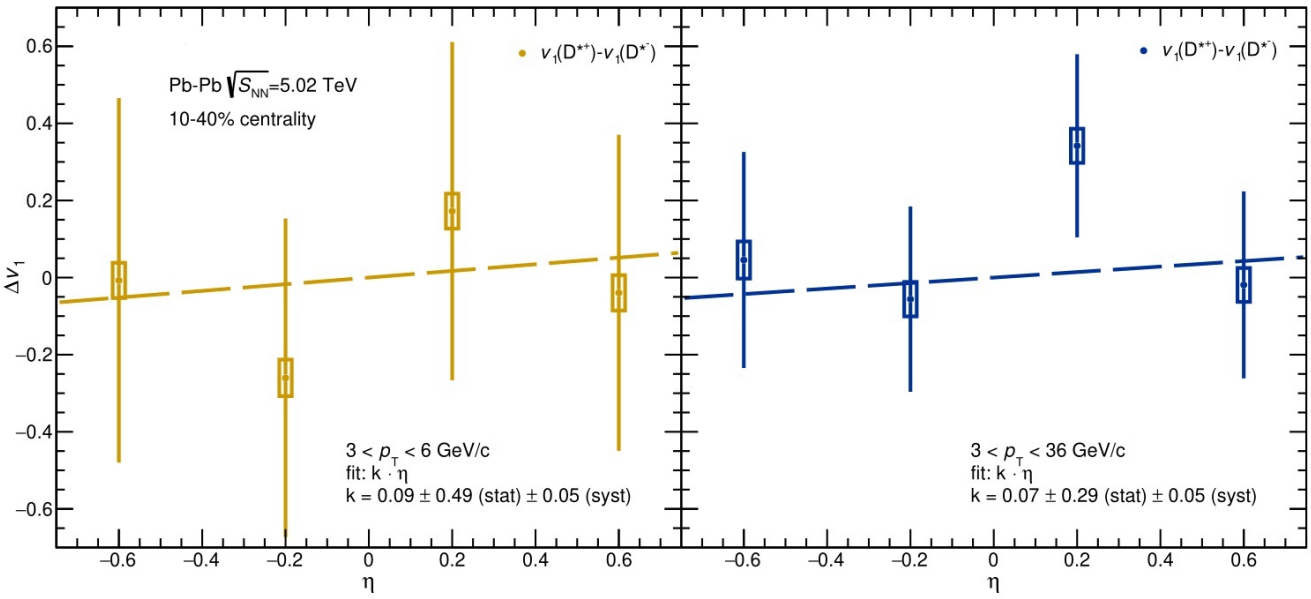

Figure 5.11: Δv_1 as a function of η for $3 < p_{\mathrm{T}} < 6\,\mathrm{GeV}/c$ (left panel) and $3 < p_{\mathrm{T}} < 36\,\mathrm{GeV}/c$ (right panel) with a linear fit (dashed line).

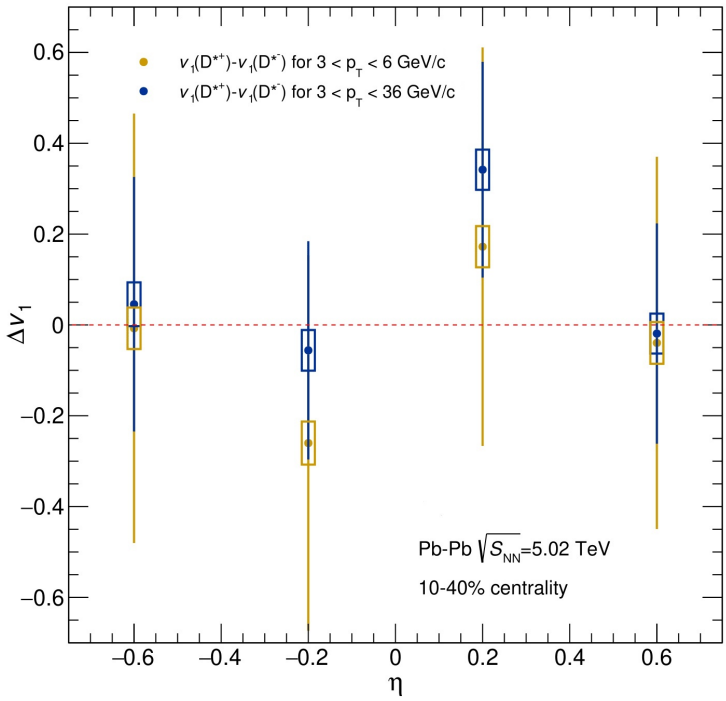

Figure 5.12: Δv_1 as a function of η for $3 < p_{\mathrm{T}} < 6\,\mathrm{GeV}/c$ (yellow) and $3 < p_{\mathrm{T}} < 36\,\mathrm{GeV}/c$ (Blue)

5.2 ZDC calibration

In this section the most recent results of the calibration of the ZDC Q-vectors are presented[3]. The re-centring of the Q-vectors is performed in the steps as described in the analysis methods. The correction of the run-based variations of the vertex position has not yet been implemented. First a description is given of how the code was build and what features it has. Afterwards the results produced using the code as described are presented.

5.2.1 Building the code

The code used for the ZDC-Calibration was built from scratch, using only parts of the previous calibration code. It was not possible to use the previous code entirely since it lacked proper documentation on how to use it and it could only be used in the 2015 Pb–Pb data set. The new code was built in such a way that the calibration can in general be performed in any data-set. All information and histograms are created dynamically needing only the run numbers as input. In this way the code can be easily re-used in future data sets without needing to make rigorous changes. As every analysis task this task consists of three parts: a header file (AnalysisTaskQnZDC.h), an implementation file (AnalysisTaskQnZDC.cxx) and an AddTask.C (Currently still built in the .cxx file). To create a better understanding of how the code works, it is important to understand how the data is analysed. All the data from the ALICE detector is saved per collision or event[4]. This analysis task is then performed for each event, each time storing the data needed from that event.

The calibration is performed in multiple steps. For each step the analysis has to be performed over the entire data set we want to calibrate. Below an overview is given of the flow of the code and how the calibration is performed:

- In the first run, called step 0, the Q-vectors are constructed and the average components needed for the first calibration step are computed and stored in an output file.
- In the second run, called step 1, everything from step 0 is repeated. Then, using the results from the output file from step 0, the first step of the calibration is performed. These partly calibrated Q-vector components are then used to compute the averages needed for the second calibration step. The averages for step 1 and step 2 are both stored in a new output file.
- In the third run, called step 2, everything from step 0 and step 1 is repeated. Then, using the results from the output file from step 1, the second step of the calibration is performed. These further calibrated Q-vector components are then used to compute the averages needed for the third calibration step. The averages for step 1, step 2 and step 3 are all stored in a new output file.

[3]The calibration process is a long and complicated one, and there was no time to finish it completely. The steps that need to be taken in the future will be discussed in the Outlook

[4]All these events are stored together in larger AOD.root files, but this is not important for now.

- In the fourth and final run over the entire data set, called step 3, everything from the previous steps is repeated. Using the output from step 3 the final calibration step can be performed. The calibrated Q-vectors are then ready to be used for further analyses.

Before performing a certain step of the analysis there are a couple of settings that must be chosen. In a separate .yaml file the basic settings for the histograms storing the averages must be set like range and number of bins. The step number and the name of the corresponding input file must be included as well. If the code must perform the calibration up to and including the second step the task needs the output file from step 1. It is also possible to toggle between showing the calibration results or not. If this option is enabled the task creates and stores the histograms showing the average Q-vector components as a function of centrality and vertex position for each run number before and after the calibration. If this option is disabled only the histograms needed for performing the calibration are stored.

Now that the general flow of the code and the different options have been explained, the actual code will be discussed in a bit more detail. The most important parts of the code will be shown explicitly, other parts will only be mentioned since the code is too elaborate to show in its entirety. Before the code is presented a couple of terms must be explained to better understand the code.

- Profiles: Profiles are a histogram class storing the average of a certain variable, in our case the Q-vector components, as a function of some other variables like centrality of vertex position. All information needed to perform the calibration is stored in one or three dimensional profiles.

- Maps: A map is an object storing elements formed by a combination of two objects. In our code some profiles must be created for all run numbers, so maps were created linking the run number to the corresponding the profiles.

- Templates: A template is a generic function able to work with generic classes. In our case the template function CreateMapProfile will be able to work with maps to profiles independent of their dimension

The code starts with defining the output containers and loading in the data from the previous step (unless we perform step 0, then this part is skipped). In the next part of the code, called the UserCreateOutputObjects(), the objects in which all information will be stored are created. The part of the code where the profiles used to store the Q-vector component averages are created, is presented below. The profiles for step 2 and 3 are created analogous to this.

```
if (fStep >= 0) {
  if (fShowCalib){
     CreateMapProfile(fRun_VtxXQPreCalib, fRunList,
                      fgkNameStep.at(0) + "PreCalibX",
                      fHistConfig.fVertexX.fNBins,
                      fHistConfig.fVertexX.fMin,
                      fHistConfig.fVertexX.fMax);
```

```
     CreateMapProfile(fRun_VtxYQPreCalib, fRunList,
                      fgkNameStep.at(0) + "PreCalibY",
                      fHistConfig.fVertexY.fNBins,
                      fHistConfig.fVertexY.fMin,
                      fHistConfig.fVertexY.fMax);
    CreateMapProfile(fRun_VtxZQPreCalib, fRunList,
                      fgkNameStep.at(0) + "PreCalibZ",
                      fHistConfig.fVertexZ.fNBins,
                      fHistConfig.fVertexZ.fMin,
                      fHistConfig.fVertexZ.fMax);
    AddToOutput(fRun_VtxXQPreCalib, fOutput);
    AddToOutput(fRun_VtxYQPreCalib, fOutput);
    AddToOutput(fRun_VtxZQPreCalib, fOutput);
  }
   CreateMapProfile(fRun_CentQ, fRunList, fgkNameStep.at(0),
                    fHistConfig.fCentrality.fNBins,
                    fHistConfig.fCentrality.fMin,
                    fHistConfig.fCentrality.fMax);
}

if (fStep >= 1) {
  if (fShowCalib) {
    CreateMapProfile(fRun_CentQCalib, fRunList,
                     fgkNameStep.at(0) + "Calib",
                     fHistConfig.fCentrality.fNBins,
                     fHistConfig.fCentrality.fMin,
                     fHistConfig.fCentrality.fMax);

    AddToOutput(fRun_CentQCalib, fOutput);
  }
  CreateMapProfile(fCent_VtxXYZQ, bins_cent, fgkNameStep.at(1),
                    fHistConfig.fVertexX.fNBins,
                    fHistConfig.fVertexX.fMin,
                    fHistConfig.fVertexX.fMax,
                    fHistConfig.fVertexY.fNBins,
                    fHistConfig.fVertexY.fMin,
                    fHistConfig.fVertexY.fMax,
                    fHistConfig.fVertexZ.fNBins,
                    fHistConfig.fVertexZ.fMin,
                    fHistConfig.fVertexZ.fMax);
  AddToOutput(fCent_VtxXYZQ, fOutput);
}
```

The code is built is such a way that only the necessary objects are created, depending on the step and on if we want to show the calibration results. The function CreateMapProfile() is a template function creating the a map of the profiles. All objects and template functions have been pre-defined in the header file. CreateMapProfile() needs as input the following variables: The name of the map, the run number or the 5% centrality bin, the name corresponding to the step, number of bins in the profile, lower boundary of the profile an the upper boundary of the profile. These are all set in either the header file or the .yaml configuration file. The AddToOutput() function adds the maps to the output container.

The next part of the code is the UserExec(). This is the core of the code, containing the "working steps" of the analysis. The UserExec() starts by saving the run number corresponding to the event currently being analysed. The next step is constructing the Q-Vectors. This part of the code was mainly inspired by the former calibration code, but needed some adaptions to get it to run in the new version of ROOT[5]. The Q-vector construction is performed by the function ComputeQvectors(). Some parts of this function are presented below.

```
void AliAnalysisTaskQnZDC::ComputeQvectors() {
  auto aod = dynamic_cast<AliAODEvent *>(InputEvent());
  auto aodZDC = dynamic_cast<AliAODZDC *>(aod->GetZDCData());

  const Double_t *fTowZNCraw1 = aodZDC->GetZNCTowerEnergy();
  const Double_t *fTowZNAraw1 = aodZDC->GetZNATowerEnergy();

  for (Int_t i = 0; i < 5; i++) {
    fTowZNCraw[i] = fTowZNCraw1[i];
    fTowZNAraw[i] = fTowZNAraw1[i];
  }

  const Double_t fx[4] = {-1.75, 1.75, -1.75, 1.75};
  const Double_t fy[4] = {-1.75, -1.75, 1.75, 1.75};

  Double_t zncEnergy = 0., znaEnergy = 0.;
  for (Int_t i = 0; i < 5; i++) {
    zncEnergy += fTowZNCraw[i];
    znaEnergy += fTowZNAraw[i];
  }
```

Above the start of the ComputeQvectors() function is presented. First the data from the event (AliAODEvent) is retrieved and stored. From there the ZDC-specific information is retrieved. From the ZDC-specific information the energy of the separate towers is stored and the total energy of each side is determined. Also the x and y positions of the ZDC-towers are defined.

```
for (Int_t i = 0; i < 4; i++) {
    // get energy
    EZNC = fTowZNCraw[i + 1];
    SumEZNC += EZNC;

    fZDCGainAlpha = 0.395;

    // build centroid
    wZNC = TMath::Power(EZNC, fZDCGainAlpha);
    numXZNC += fx[i] * wZNC;
    numYZNC += fy[i] * wZNC;
    denZNC += wZNC;

    // get energy
```

[5]The old code was built for ROOT 5, however a large update to ROOT 6 took place making it necessary to change the code

```
    EZNA = fTowZNAraw[i + 1];
    SumEZNA += EZNA;

    // build centroid

    wZNA = TMath::Power(EZNA, fZDCGainAlpha);
    numXZNA += fx[i] * wZNA;
    numYZNA += fy[i] * wZNA;
    denZNA += wZNA;
}
```

Then using information based on the ZDC gain equalisation process corrections to the energy are applied[6]. Using these corrected energies the Q-vectors are constructed. In the next step of the analysis the function EventInfo() is created to retrieve information on the event, such as centrality and vertex position. Also the values of the separate Q-vector components are stored in this function.

Finally, now that all information needed to perform the calibration has been gathered, the actual re-centring is performed. This part of the code is also built in such a way that it only performs the calibration up to an including the step set in the beginning.

```
if (fStep >= 0){
  if(fShowCalib){
    FillProfiles(&fRun_VtxXQPreCalib,fEvInfo.fRunNum, fEvInfo.fVtxX);
    FillProfiles(&fRun_VtxYQPreCalib,fEvInfo.fRunNum, fEvInfo.fVtxY);
    FillProfiles(&fRun_VtxZQPreCalib,fEvInfo.fRunNum, fEvInfo.fVtxZ);
  }
  FillProfiles(&fRun_CentQ, fEvInfo.fRunNum, fEvInfo.fCent);
  }
if (fStep >= 1) {
  auto means = GetMeansProfiles(fAvr_Run_CentQ, fEvInfo.fCent);
  SubtractMeanFromQVectors(means, fEvInfo.fRunNum);

  if (fShowCalib) FillProfiles(&fRun_CentQCalib,
  fEvInfo.fRunNum, fEvInfo.fCent);

  FillProfiles(&fCent_VtxXYZQ, fEvInfo.fCentBin,
  fEvInfo.fVtxX, fEvInfo.fVtxY, fEvInfo.fVtxZ);
}
```

FillProfiles(), GetMeansProfiles() and SubstractMeanFromQVectors() are template functions used for filling the profiles, retrieving the average Q-vector components from the previous calibration file and subtracting the averages from the current Q-vector components respectively. As before these functions have been defined in the header file. This part of the header file is presented below, together with the definition of the CreateMapProfile().

[6]We have not performed the gain equalisation process for the current data set. There are some corrections that were applied based on the gain equalisation of the 2015 data-set.The assumption was made that these corrections can also be applied here.

```
\\Defintion of the FillProfiles function
template <typename Profile, typename... DependendVariables>
void AliAnalysisTaskQnZDC::FillProfiles(std::map<TupleInt, Profile> *p_map,
                                        Int_t bin_tuple,
                                        DependendVariables... args) {
  p_map->at(std::make_tuple("A", "Re", bin_tuple)).Fill(args...,
                                                        fEvInfo.fQARe);
  p_map->at(std::make_tuple("A", "Im", bin_tuple)).Fill(args...,
                                                        fEvInfo.fQAIm);

  p_map->at(std::make_tuple("C", "Re", bin_tuple)).Fill(args...,
                                                        fEvInfo.fQCRe);
  p_map->at(std::make_tuple("C", "Im", bin_tuple)).Fill(args...,
                                                        fEvInfo.fQCIm);
}

\\Defintion of the SubtractMeanFromQVectors function
template <typename Tuple>
void AliAnalysisTaskQnZDC::SubtractMeanFromQVectors(std::map<Tuple,
                                                    Double_t> means,
                                                    int bin) {
  fEvInfo.fQARe -= means.at(std::make_tuple("A", "Re", bin));
  fEvInfo.fQAIm -= means.at(std::make_tuple("A", "Im", bin));

  fEvInfo.fQCRe -= means.at(std::make_tuple("C", "Re", bin));
  fEvInfo.fQCIm -= means.at(std::make_tuple("C", "Im", bin));
}

\\Defintion of the CreateMapProfile function
template <typename Profile, typename... AxisContructor>
void AliAnalysisTaskQnZDC::CreateMapProfile
                           (std::map<TupleInt, Profile> &profile,
                            std::vector<Int_t> fBinsList,
                            std::string base_name,
                            AxisContructor... axis_contructor_args) {

  for (auto side : fgkSides) {
    for (auto component : fgkComponents) {
      for (auto bin : fBinsList) {
        std::stringstream name;
        name << std::to_string(fStep) << "_";
        name << side << "_" << component << "_" << std::to_string(bin);
        name << "-" << base_name;
        auto name_str = name.str();

        auto hist = Profile(name_str.c_str(), name_str.c_str(),
                            axis_contructor_args...);

        profile.emplace(std::make_tuple(side, component, bin), hist);
      }
    }
  }
}
```

```
template <typename Tuple, typename Profile, typename... BinType>
std::map<Tuple, Double_t> AliAnalysisTaskQnZDC::GetMeansProfiles(
    std::map<Tuple, Profile> &profile_map, BinType... BinValues) {
  std::map<Tuple, Double_t> means;
  for (auto &x : profile_map) {
    auto &key = x.first;
    auto &hist = x.second;
    means.emplace(key, hist.GetBinContent(hist.FindBin(BinValues...)));
  }
  return means;
};
```

The code presented is work in progress and it will be adjusted and updated as the calibration process continues. The code as presented here was used to create the results in the next section. When the code has been completed and the calibration is complete the code will be available for the ALICE collaboration.

5.2.2 Calibration results

The data used to create the presented results consists of a small subset of the total 2018 Pb–Pb data set, run lists 279588, 279890 and 279595. Since the code is under construction it is not possible to run it via the LEGO train system, so private jobs were used. In Fig. 5.13 and Fig. 5.14 the results for the re-centring of the Q-vectors are presented. The calibrated figures present the averages after all three calibration steps. As can be seen from the figures the event variable dependent variations of the Q-Vector components are removed during the calibration. In Fig. 5.14 it becomes clear the run-based variations of the vertex position are still present.
An additional check was performed on the correlations between the Q-vectors components $\langle Q_x^A Q_x^C \rangle$,$\langle Q_y^A Q_y^C \rangle$, $\langle Q_x^A Q_y^A \rangle$ and $\langle Q_x^C Q_y^C \rangle$. The results for the correlations in this sub-set of the 2018 data as well as the comparison of the 2018 calibration with the 2015 calibration are presented in Fig. 5.15. The results clearly show the effect of the calibration steps. The correlations behave as expected except for $\langle Q_x^A Q_x^C \rangle$, which has positive values while negative values would be in agreement with both the 2015 calibration procedure, as can be seen in the bottom two panels of Fig. 5.15, as well as with the theory mentioned briefly in the Analysis Methods.

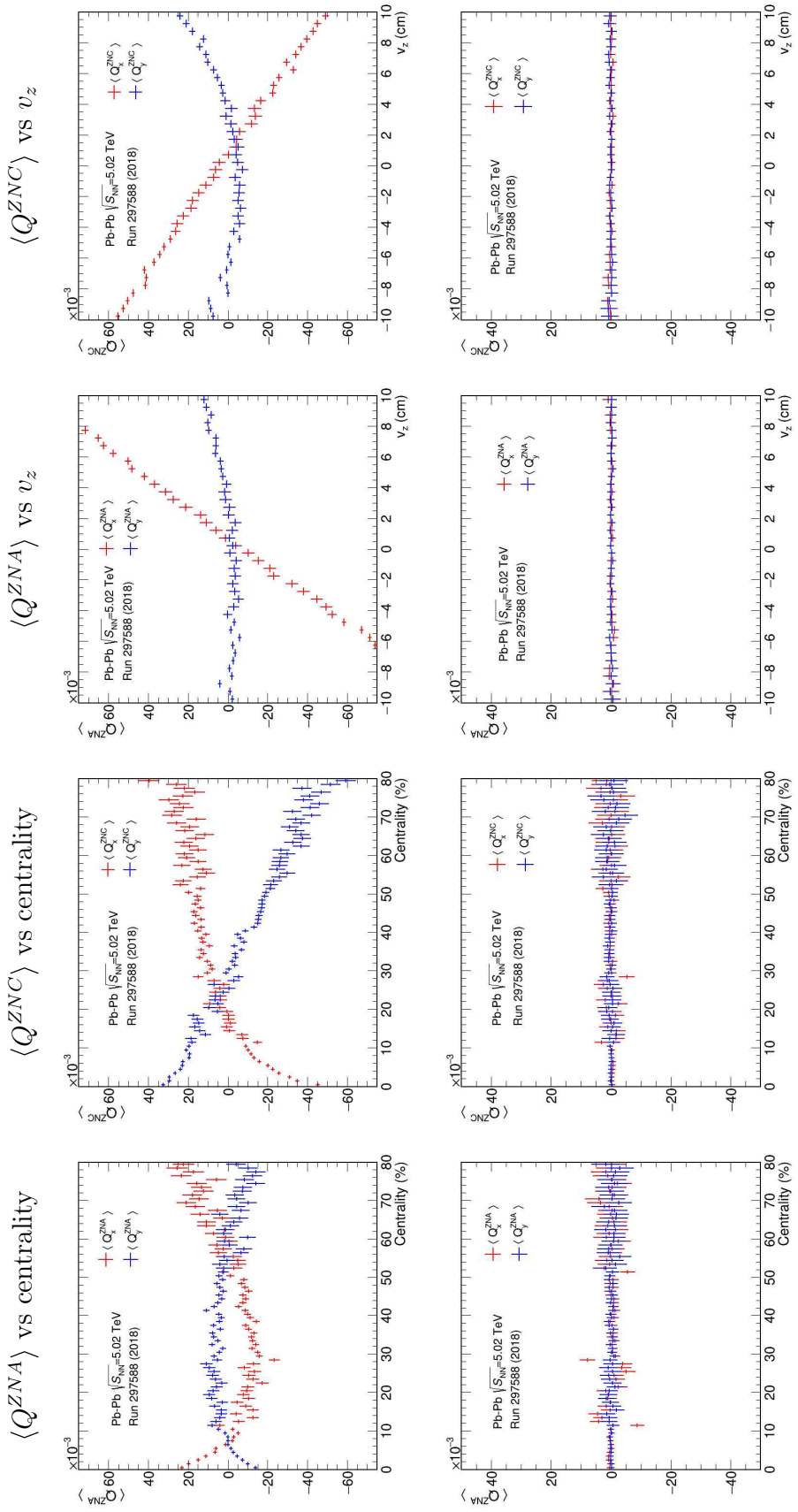

Figure 5.13: The values for $\langle Q_x^{ZN} \rangle$ (Red) and $\langle Q_y^{ZN} \rangle$ (Blue) as a function of centrality (left) and v_z (right) before (top) and after (bottom) the re-centring steps for run 279588

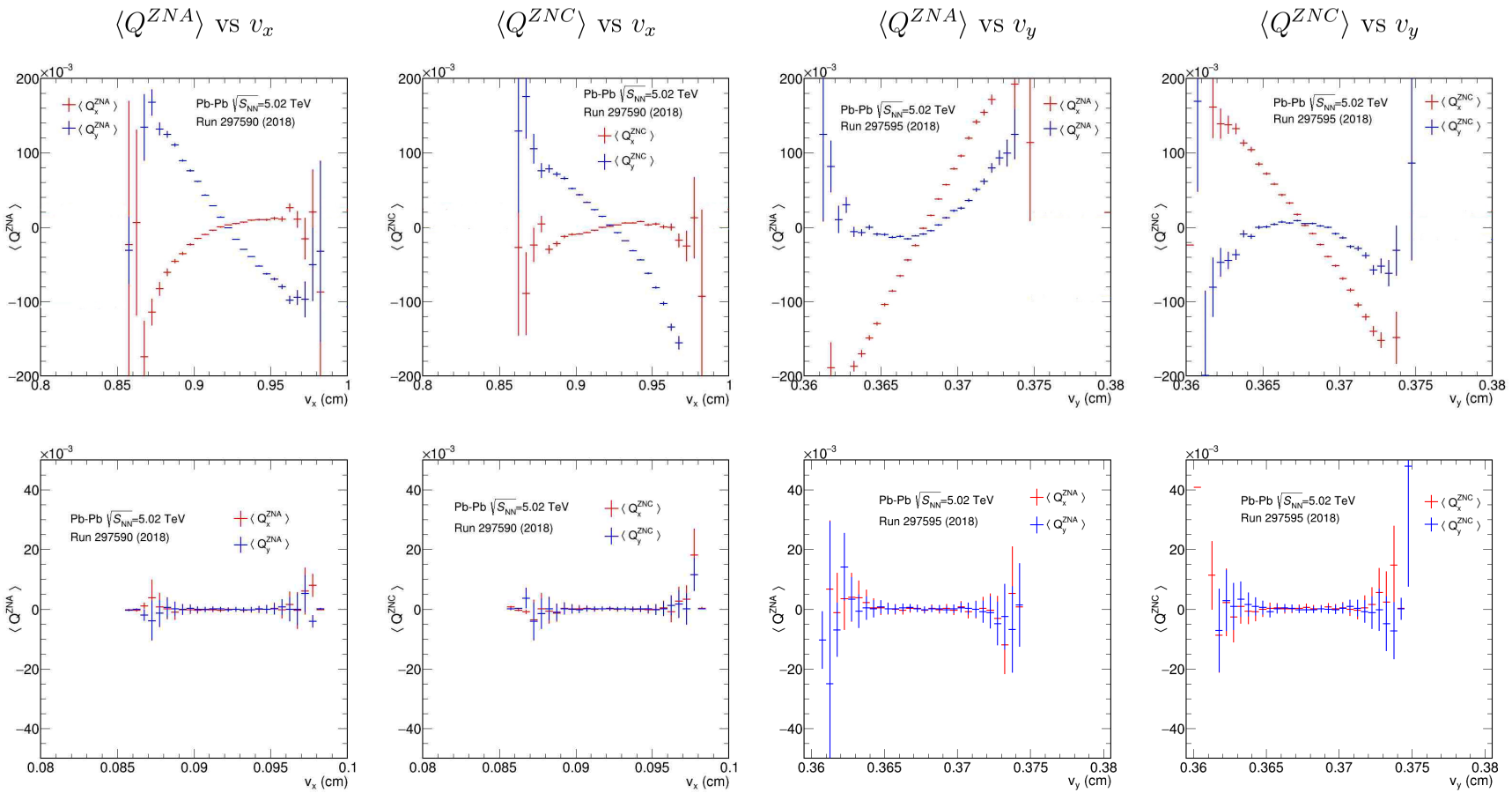

Figure 5.14: The values for $\langle Q_x^{ZN} \rangle$ (Red) and $\langle Q_y^{ZN} \rangle$ (Blue) as a function of v_x (left) and v_y (right) before (top) and after (bottom) the re-centring steps for run 279590 (v_x) and run 279595 (v_y)

Before calibration

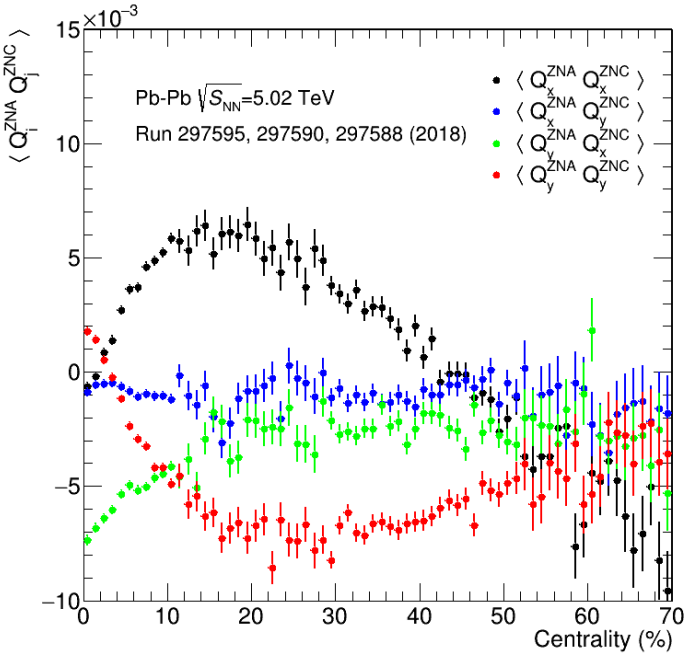

After calibration

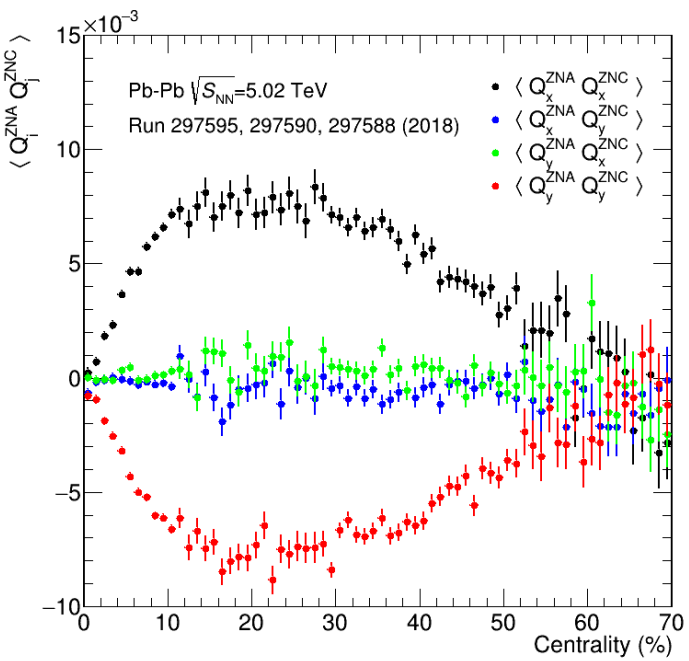

2015 calibration

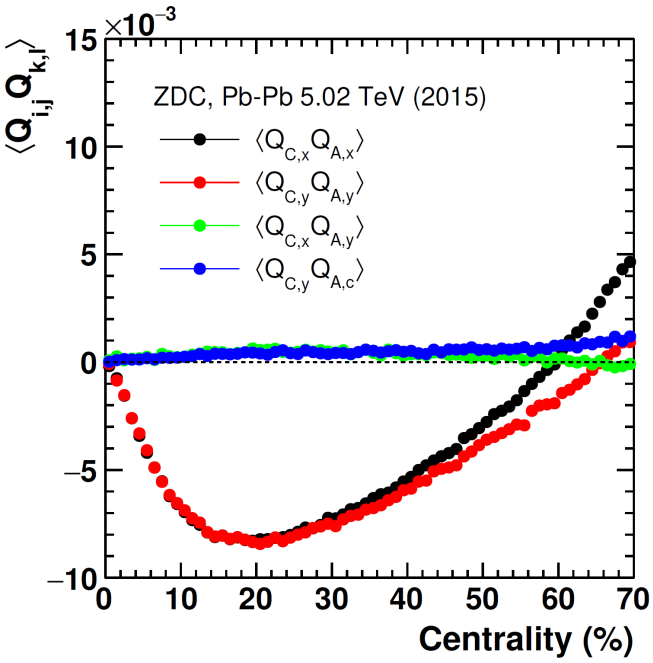

2018 calibration

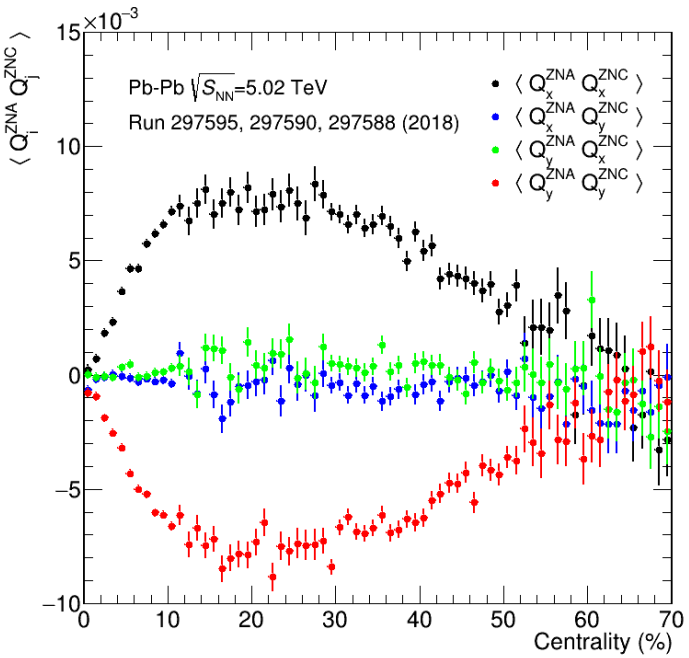

Figure 5.15: The top two figures show the comparison between the correlations of the Q-vector components before (left) and after (right) the calibration procedure in a subset of the 2018 data set. The bottom two figures show a comparison between the calibration results of the correlations between the Q-vector components in the 2015 data set (left, figure taken from [17]) and in a subset of the 2018 data set (right).

Chapter 6

Discussion

In this chapter the results of the directed flow measurements and the ZDC-calibration process presented in the previous chapter will be discussed.

6.1 On the directed flow measurement

The simultaneous fits

It was noticed in the first analyses of the simultaneous fits in the $3 < p_{\mathrm{T}} < 6\,\mathrm{GeV}/c$ transverse momentum region that there was a limited amount of statistics. The D^{*+} and D^{*-} mesons are relatively rare mesons, and the branching ratio of decay into a D^0 and a soft-pion is also small (3.9%). Besides that we needed to split up the available data into four pseudorapidity bins, further reducing the statistics. On top of this comes some loss of statistics from the ZDC calibration. For some events it is impossible to construct proper Q-vectors and if no Q-vector can be constructed, the directed flow of the candidate cannot be determined. This results in a further drop in statistics. All these factors combined lead to the poor statistics presented in these results. The poor statistics in the low transverse momentum region has two important effects. First of all it reduces the quality of the invariant mass peaks, leading to less accurate mass fits. Furthermore the reduced statistics in both the invariant mass peak and in the background of the invariant mass plot lead to a larger effect of statistical fluctuations in the directed flow plot. This eventually results in a larger statistical uncertainty in the final reported value of the directed flow.
The statistics in the $3 < p_{\mathrm{T}} < 36\,\mathrm{GeV}/c$ transverse momentum region are significantly better, but still limited. The invariant mass peaks are more pronounced and the background signal is more stable, which is reflected in the reduced statistical uncertainty.

The cut optimisation process

The process of optimising the cuts did not lead to a significant decrease of the statistical uncertainties. The invariant mass peaks were more pronounced in both the optimised sets of cuts. The background signals however showed more fluctuations. Since the directed flow fit is highly dependent on the background of the invariant mass, the reduced background

stability leads to an increase in the uncertainty. This however can again be lead back to the problem of the limited statistics.
The cut optimisation was also performed only once with one set of variables. It is possible that another set of variables would have been more suited. Furthermore a choice must always be made with respect to the number of steps and the interval in which the variables are varied. Since only a limited amount of time is available it was not possible to do further fine tuning on the set of cuts. However, even with improved cutting variables we would still have the problem of the limited statistics that cannot be solved by only improving the cuts.

The Δv_1 results

The results of the charge dependent directed flow as presented in Table 5.9 also show the effects of the limited statistics. As can be seen from the corresponding figure (Fig .5.11) no significant slope is found within the statistic uncertainty for both transverse momentum regions. The Δv_1 seems to fluctuate around zero. The directed flow measurement on D^0 and $\overline{\mathrm{D}_0}$ mesons ($3 < p_{\mathrm{T}} < 6\,\mathrm{GeV}/c$ transverse momentum region and $10\% - 40\%$ centrality) yielded a slope of $\mathrm{d}\Delta v_1/\mathrm{d}\eta = [4.9 \pm 1.7\,(\mathrm{stat.}) \pm 0.6\,(\mathrm{syst.})] \cdot 10^{-1}$ and show a clear hint to a positive slope.[15] The results presented in this thesis neither prove nor disprove the results from the D^0 measurements since the statistical uncertainties are too large compared to the signal. The systematic uncertainties between the D^{*+} and the D^0 measurement are very similar. This is as expected since the analyses were performed in an analogous way.
A comparison with theoretical models describing the directed flow of charm mesons as in [56] cannot be made. Both the theoretical models and the presented experimental results have too large uncertainties. Before we are able to make comparisons between theory and experiment and before we can start constraining theoretical parameters using experimental results a lot more work is needed on both the theoretical an experimental side. Future data sets like the 2018 Pb–Pb run at the LHC will provide a large boost in statistics that will reduce the uncertainties in the measurements.

6.2 On the ZDC-calibration

The calibration of the ZDC is, as mentioned before, an ongoing process. The results presented in the previous chapter only used 3 run numbers out of the total data-set, which consists of 216 run numbers. The re-centring of the Q-vector components was performed successfully as can be seen from both Fig. 5.13 and Fig. 5.14. The correlations between the Q-vector components do not all behave as expected from the calibration results of the 2015 data set and from a theory perspective. The correlations $\langle Q_y^A Q_y^C \rangle < 0$ and $\langle Q_x^A Q_y^A \rangle = \langle Q_x^C Q_y^C \rangle = 0$ all three show the expected behaviour, although since only a small subset of the data set is used there is still a significant amount of statistical uncertainty. The correlations $\langle Q_x^A Q_x^C \rangle$ does not show the expected behaviour. The shape of the correlation as a function of centrality does correspond to the 2015 results, but it has the opposite sign. This sign switch could have multiple reasons. The first possibility is an error somewhere in the code. If the analysis would be repeated over a (sub)set of the 2015 data using the code that was built, it could be checked if the difference arises from the code or from the data set. The parts of the code where the Q-vectors are built from both the newly built calibration code and the

old calibration code were thoroughly compared, but no apparent differences that could lead to a switched sign were found. Another option would be that the difference arose because corrections for the ZDC tower energies were used based on the ZDC gain equalisation of the 2015 data set. The Q-vector components are heavily dependent on the energy data from the tower so this could lead to a bias in the results. However the results as presented strongly indicate that the re-centring of the Q-vector components is performed with success. A third possibility is that the switch in sign does not come from mistakes or misplaced corrections in the code, but that there is a physical reason that this occurs. To find which of these causes the sign switch, a lot more testing is needed.

Apart from the switched sign in the $\langle Q_x^A Q_x^C \rangle$ correlation, there is still quite some room for improvement. The Q-vector components suffering from border effects from the detector are not yet removed, no correction is yet applied for the run-based variation of the mean vertex position and the ZDC gain-equalisation has not yet been performed. As mentioned above, in the code some corrections based on the gain-equalisation results from the calibration of the 2015 data set are in place. In the results presented it is assumed these corrections can be applied to the 2018 data set as well. This however is almost certainly not the case and a the calibration process can be greatly improved by performing the gain equalisation.

Chapter 7

Conclusion

The conclusions of the analysis performed in this thesis are presented below. First the conclusion on the charge dependent directed flow is given. Afterwards the conclusion on the ZDC calibration is given.

7.1 The charge dependent directed flow

No significant charge dependent directed flow was found for D^{*+} mesons in both the $3 < p_{\mathrm{T}} < 6\,\mathrm{GeV}/c$ and the $3 < p_{\mathrm{T}} < 36\,\mathrm{GeV}/c$ transverse momentum regions. The Δv_1 fluctuates around zero and within the statistical uncertainty no positive or negative $\mathrm{d}\Delta v_1/\mathrm{d}\eta$ could be found. Because of the poor statistics the uncertainties were too large for a significant comparison of these results with either the D^0 measurements or theoretical models. An increase in statistics is necessary in order to reduce the uncertainties and to find a significant result for $\mathrm{d}\Delta v_1/\mathrm{d}\eta$.

7.2 The ZDC calibration

From the presented results we can come to the conclusion that the re-centring of the Q-vector components is performed by the code. However, an anomaly is present in the sign of the $\langle Q_x^A Q_x^C \rangle$ correlation that not yet can be explained. Besides that a lot of additional steps must be taken to perform the entire calibration and to make the code usable as a dependency for e.g. the directed flow analysis.

Chapter 8

Outlook

In this chapter the future studies that can be done on the charge dependent directed flow as well as the work that needs to be done to complete the ZDC calibration will be discussed. In contrast with the previous chapters we will first discuss the ZDC calibration before we discuss the future of the directed flow measurements, since the calibration must be completed before directed flow analyses can be performed in new data sets.

8.1 On the ZDC calibration

As mentioned before the calibration of the ZDC detector is work in progress. A good start has been made on the re-centring of the Q-vectors, however the project is far from complete. To begin with, the gain equalisation of the ZDC-tower energies must be performed in the 2018 data. After this has been done the corrections from this equalisation must be incorporated into the code constructing the Q-vectors. Furthermore the Q-vector re-centring must be completed.

In order to complete the re-centring of the Q-vectors a number of things must be performed. The run-dependent variations on the vertex positions must be determined and must be corrected for. Then the Q-vectors built with data from "bad"-vertex positions i.e. built with data from collisions that are on the boundaries of the detector must be removed from the data set. If this all is incorporated into the code the core of the task is complete. It is possible that additional re-centring steps must be applied, but this depends on the effect of the re-centring steps in the 2018 data set.
A number of extra features must be incorporated into the code before it can be used as a dependency for other codes. As the code is presented at the moment it will always show a number of histograms. An extra command or variable must be put into the code to set the code to "calibration" mode, in which no new histograms are filled and the only output of the task are the re-centred ZDC Q-vectors. To accommodate this after each calibration step the Q-vectors must be updated as well. Furthermore the calibration must be performed using the entire 2018 data set and all steps of the calibration must be checked for anomalies, including the correlations between the different components. As mentioned in the discussion an anomaly is present in the sign of the $\langle Q_x^A Q_x^C \rangle$ correlation. The reason for this sign switch

must be investigated further as well. In addition one could also consider implementing new re-centring steps to further improve the calibration process. For example the Q-vector component averages could be re-centred as a function of the total energy. As a final step the code must be accepted by the ALICE collaboration and be incorporated into the AliPhysics library, for it to be usable as a dependency for other analyses like the directed flow analysis.

8.2 On the directed flow measurement

Once the ZDC-calibration framework has been completed and the calibration is done for the 2018 Pb–Pb data set the directed flow analysis of both the D^{*+} and the D^0 mesons as well as the directed flow analysis of charged hadrons (also described in [15]) can be repeated in this data. However, additional checks can also be performed in the current data.

The cutting parameters used for the analysis described in this thesis are not optimised. It was attempted to optimise the cuts but this was not successful. Different parameters could be optimised and one could perform multiple optimisation processes each time choosing a smaller interval. In this way the cuts would be fine tuned to create an optimal set of cuts. Besides improving the cut optimisation one could see what the effect would be if a correction was applied for the slight dependence of the efficiencies on pseudorapidity. In this thesis no correction was applied but additional checks can be performed to see what the effect would be is the corrections were applied.

The future of the charge dependent directed measurements however lies in the 2018 Pb–Pb data set (and future data sets). The 2018 data set contains around 30 times more data which results in a significant decrease of the statistical uncertainty. If more precise results are available a proper comparison with theory can be made. These future results could provide important restrictions on parameters from theoretical models and could, in the end, lead to boundaries on the strength and lifetime of electromagnetic fields formed during heavy ion collisions. This however does not lie in the near future and would require many more studies. Nevertheless the subject of charge-dependent directed flow is one with a bright future and one in which a lot of advances can be made.

Bibliography

[1] B.R. Martin. *Nuclear and Particle Physics. an introduction*. Second Edition. John Wiley Sons Ltd, 2009.

[2] W.N. Cottingham and D.A. Greenwood. *An Introduction to the Standard Model of Particle Physics*. Second Edition. Cambridge University Press, 2013.

[3] J. H. Christenson *et al.*. "Evidence for the 2π Decay of the K_2^0 Meson". In: *Phys. Rev. Lett.* **13** (1964). 138. DOI: 10.1103/PhysRevLett.13.138.

[4] M. Kobayashi and T. Maskawa. "CP-Violation in the Renormalizable Theory of Weak Interaction". In: *Progress of Theoretical Physics* **49** (2 1973). DOI: 10.1143/PTP.49.652.

[5] T. Mannel. "Theory and Phenomenology of CP Violation". In: *Nuclear Physics B - Proceedings Supplements* **176** (2007). DOI: 10.1016/j.nuclphysbps.2006.12.083.

[6] R. D. Peccei and Helen R. Quinn. "CP Conservation in the Presence of Pseudoparticles". In: *Phys. Rev. Lett.* **38** (1977). 1440. DOI: 10.1103/PhysRevLett.38.1440.

[7] E. V. Shuryak. "Theory of Hadron Plasma". In: *Zh. Eksp. Theor. Fiz.* **74** (1978). 408.

[8] U. Heinz, M. Jacob. *Evidence for a New State of Matter: An Assessment of the Results from the CERN Lead Beam Programme*. preprint at arXiv:nucl-th/0002042. 2000.

[9] K. Tuchin. ""Particle production in strong electromagnetic fields in relativistic heavy-ion collisions"". In: *Adv. High Energy Phys.* **2013** (2013). 490495, arXiv:1301.0099 [hep-ph].

[10] K. Fukushima, D. E. Kharzeev, H. J. Warringa. "The Chiral Magnetic Effect". In: *Phys. Rev. D* **78** (2008). 074033, arXiv:0808.3382 [hep-ph]. DOI: 10.1103/PhysRevD.78.074033.

[11] **STAR** Collaboration, B. I. Abelev *et al.*. "Observation of charge-dependent azimuthal correlations and possible local strong parity violation in heavy-ion collisions". In: *Phys. Rev. C* **81** (2010). 054908, arXiv:0909.1717 [nucl-ex]. DOI: 10.1103/PhysRevC.81.054908.

[12] **ALICE** Collaboration, A. Betti *et al.*. "Charge separation relative to the reaction plane in Pb–Pb collisions at $\sqrt{s_{\mathrm{NN}}} = 2.76$ TeV ". In: *Phys. Rev. Lett.* **110** (2013). 012301, arXiv:1207.0900 [nucl-ex]. DOI: 10.1103/PhysRevLett.110.012301.

[13] **STAR** Collaboration, L. Adamczyk *et al.*. "Fluctuations of charge separation perpendicular to the event plane and local parity violation in $\sqrt{s_{\mathrm{NN}}} = 200$ GeV Au–Au collisions at the BNL RHIC". In: *Phys. Rev. C* **88** (2013). 064911, arXiv:1302.3802 [nucl-ex]. DOI: 10.1103/PhysRevC.88.064911.

[14] **CMS** Collaboration, V. Khachatryan *et al.*. "Observation of charge-dependent azimuthal correlations in p–Pb collisionsand its implication for the search for the chiral magnetic effect". In: *Phys. Rev. Lett.* **118** (2017). 122301, arXiv:1610.00263 [nucl-ex]. DOI: 10.1103/PhysRevLett.118.122301.

[15] **ALICE** Collaboration, A. Shreyasi *et al.*. *Probing the effects of strong electromagnetic fields with charge-dependent directed flow in Pb–Pb collisions at the LHC*. 012301, arXiv:1910.14406 [nucl-ex]. 2019.

[16] **STAR** Collaboration, J. Adam *et al.*. "First observation of the directed flow of D^0 and $\overline{\mathrm{D}_0}$ in Au–Au collisions at $\sqrt{s_{\mathrm{NN}}} = 200$ GeV ". In: *Phys. Rev. Lett.* **123** (2019). 162301, arXiv:1905.02052 [nucl-ex].

[17] J. Margutti. "Rotating Planes, Flucuating Shapes. Anisotropic Flow and Magnetic Fields in Heavy-Ion Collisions". PhD thesis. Utrecht University, 2018.

[18] J. D. Bjorken. "Asymptotic Sum Rules at Infinite Momentum". In: *Phys. Rev.* **179** (1969). 1547. DOI: 10.1103/PhysRev.179.1547.

[19] J. D. Bjorken and E. A. Paschos. "Inelastic Electron-Proton and -Proton Scattering and the Structure of the Nucleon". In: *Phys. Rev.* **185** (1969). 1975. DOI: 10.1103/PhysRev.185.1975.

[20] G. Zweig. "An SU_3 model for strong interaction symmetry and its breaking". In: *Developments in the Quark Theory of Hadrons* **1** (1980). First published as a Cern Report (CERN-TH-401) on January 17, 1964.

[21] M. Gell-Mann. "A schematic model of baryons and mesons". In: *Phys. Lett.* **8** (1964). DOI: 10.1016/S0031-9163(64)92001-3.

[22] D. Griffiths. *Introduction to Elementary Particles*. Second, Revised Edition. Wiley-VCH, 2008.

[23] S. Weinberg. "A model of leptons". In: *Phys. Rev. Lett.* **19** (1967). 1264. DOI: 10.1103/PhysRevLett.19.1264.

[24] A. Salam and J.C. Ward. "Electromagnetic and weak interactions". In: *Phys. Lett* **12** (1964). 2. DOI: 10.1016/0031-9163(64)90711-5.

[25] S.L. Glashow. "Partial-symmetries of weak interactions". In: *Nucl. Phys.* **22** (1961). 4. DOI: 10.1016/0029-5582(61)90469-2.

[26] G. Martinez. *Advances in Quark Gluon Plasma*. arXiv:1304.1452 [nucl-ex]. 2011.

[27] D. J. Gross and F. Wilczek. "Asymptotically free gauge theories I". In: *Phys. Rev. D* **8** (1973). 3633. DOI: 10.1103/PhysRevD.8.3633.

[28] S. Bethke. "Experimental tests of asymptotic freedom". In: *Prog. Part. Nucl. Phys.* **58** (2007). DOI: 10.1016/j.ppnp.2006.06.001.

[29] A. Deur, S. J. Brodsky and G.F. de Teramond. "The QCD Running Coupling". In: *Prog. Part. Nucl. Phys.* **90** (2016). arXiv:1607.08082 [hep-ph]. DOI: 10.1016/j.ppnp.2016.04.003.

[30] C. Ratti. "Lattice QCD and heavy ion collisions: a review of recent progress". In: *Rep. Prog. Phys.* **81** (2018). 084301. DOI: 10.1088/1361-6633/aabb97.

[31] F. Karsch. "Lattice QCD at High Temperature and Density". In: *Plessas W., Mathelitsch L. (eds) Lectures on Quark Matter. Lecture Notes in Physics* **583** (2002). DOI: 10.1007/3-540-45792-5_6.

[32] M. A. Stephanov. "QCD Phase Diagram: An Overview". In: *PoS LAT2006:024* (2006). arXiv:hep-lat/0701002.

[33] B. V. Jacak and B. Mülller. "The Exploration of Hot Nuclear Matter". In: *Science* **337** (2012). DOI: 10.1126/science.1215901.

[34] M. G. Alford et Al.. "Color superconductivity in dense quark matter". In: *Rev. Mod. Phys.* **80** (2008). DOI: 10.1103/RevModPhys.80.1455.

[35] M. A. Stephanov. "QCD Phase Diagram and the Critical Point". In: *Intern. J. Mod. Phys. A* **20** (2005). DOI: 10.1142/S0217751X05027965.

[36] C. Patrignani et Al. [Particle Data Group]. "Review of Particle Physics". In: *Chin Phys. C* **40** no. 10 (2016). DOI: 10.1088/1674-1137/40/10/100001.

[37] N. Cabibo and G. Parisi. "Exponential Hadronic Spectrum and Quark Liberation". In: *Phys. Lett. B* **59** (1975). DOI: 10.1016/0370-2693(75)90158-6.

[38] J.C. Collins and M.J. Perry. "Superdense Matter: Neutrons or Asymptotically Free Quarks?" In: *Phys. Rev. Lett.* **34** (1975). DOI: 10.1103/PhysRevLett.34.1353.

[39] U. Heinz and R. Snellings. "Collective Flow and Viscosity in Relativistic Heavy-Ion Collisions". In: *Ann. Rev. Nucl. PArt. Phys.* **63** (2013). DOI: 10.1146/annurev-nucl-102212-170540.

[40] E. Shuryak. "Strongly coupled quark-gluon plasma in heavy ion collisions". In: *Rev. Mod. Phys.* **89** (2017). DOI: 10.1103/RevModPhys.89.035001.

[41] W. Busza, K. Rajagopal and W. van der Schee. "Heavy Ion Collisions: The Big Picture and the Big Questions". In: *Ann. Rev. Nucl. Part. Sci.* **68** (2018). DOI: 10.1146/TBD.

[42] B. Alver et Al.. *The PHOBOS Glauber Monte Carlo*. ArXiv:0805.4411 [nucl-ex]. 2008.

[43] S. Voloshin and Y. Zhang. "Flow study in relativistic nuclear collisions by Fourier expansion of azimuthal particle distributions". In: *Z Phys C - Particles and Fields* **70** (1996). DOI: 10.1007/s002880050141.

[44] A. Bilandzic. "Anisotropic Flow Measurements in ALICE at the Large Hadron Collider". PhD thesis. Utrecht University, 2012.

[45] D.E. Kharzeev et Al.. "Chiral Magnetic and Vortical Effects in High-Energy Nuclear Collisions — A Status Report". In: *Prog. Part. Nucl. Phys* **88** (2016). arXiv:1511.04050 [hep-ph]. DOI: 10.1016/j.ppnp.2016.01.001.

[46] G. Backenstoss et Al.. "Helicity of ⁻ Mesons from π-meson decays". In: *Phys. Rev. Lett.* **6** (1961). DOI: 10.1103/PhysRevLett.6.415.

[47] Y. Ashie et Al.. "Evidence for an Oscillatory Signature in Atmospheric Neutrino Oscillations". In: *Phys. Rev. Lett.* **93** (2004). DOI: 110.1103/PhysRevLett.93.101801.

[48] G.L. Ma and B. Zhang. "Effects of final state interactions on charge separation in relativistic heavy ion collisions". In: *Phys. Lett. B* **700** (2011). arXiv:1101.1701 [nucl-th]. DOI: 10.1016/j.physletb.2011.04.057.

[49] S.A. Voloshin. "Parity violation in hot QCD: how to detect it". In: *Phys. Rev. C* **70** (2004). arXiv:hep-ph/0406311. DOI: 10.1103/PhysRevC.70.057901.

[50] O. Kaczmarek and M. Müller. "Temperature dependence of electrical conductivity and dilepton rates from hot quenched lattice QCD". In: *PoS LATTICE* **2013** (2014). arXiv:1312.56091 [hep-lat].

[51] U. Gursoy, D. Kharzeev and K. Rajagopal. "Magnetohydrodynamics, charged currents and directed flow in heavy ion collisions". In: *Phys. Rev. C.* **89** (2014). arXiv:1401.3805 [hep-ph]. DOI: 10.1103/PhysRevC.89.054905.

[52] D. E. Soper. *Classical Field Theory*. Dover Edition. Dover Publication Inc., 2008.

[53] P. Bozek and I. Wyskiel. "Directed flow in ultrarelativistic heavy-ion collisions". In: *Phys. Rev. C.* **81** (2010). arXiv:1002.4999 [nucl-th]. DOI: 10.1103/PhysRevC.81.054902.

[54] M. Luzum and J. Ollitrault. "Directed flow at midrapidity in heavy-ion collisions". In: *Phys. Rev. Lett.* **106** (2011). arXiv:1011.6361 [nucl-ex]. DOI: 10.1103/PhysRevLett.106.102301.

[55] S. Chatterjee and P. Bozek. "Large directed flow of open charm mesons probes the three dimensional distribution of matter in heavy ion collisions". In: *Phys. Rev. Lett.* **120** (2018). arXiv:1712.01189 [nucl-th]. DOI: 10.1103/PhysRevLett.120.192301.

[56] S.K. Das et Al.. "Directed Flow of Charm Quarks as a Witness of the Initial Strong Magnetic Field in Ultra-Relativistic Heavy Ion Collisions". In: *Phys. Lett. B* **768** (2018). arXiv:1608.02231 [nucl-th]. DOI: 10.1016/j.physletb.2017.02.046.

[57] L. Evans and P. Bryant. "LHC Machine". In: *JINST* **3** (2008). S08001. DOI: 10.1088/1748-0221/3/08/S08001.

[58] **ATLAS** Collaboration, G. Aad *et al.*. "The ATLAS Experiment at the CERN Large Hadron Collider". In: *JINST* **3** (2008). S08003. DOI: 10.1088/1748-0221/3/08/S08003.

[59] **ALICE** Collaboration, K. Aamodt *et al.*. "The ALICE Experiment at the CERN LHC". In: *JINST* **3** (2008). S08002. DOI: 10.1088/1748-0221/3/08/S08002.

[60] **CMS** Collaboration, S. Chatrchyan *et al.*. "The CMS Experiment at the CERN LHC". In: *JINST* **3** (2008). S08004. DOI: 10.1088/1748-0221/3/08/S08004.

[61] **LHCb** Collaboration, A. A. Alver Jr. *et al.*. "The LHCb Detector at the LHC". In: *JINST* **3** (2008). S08005. DOI: 10.1088/1748-0221/3/08/S08005.

[62] **CERN**. URL: https://home.cern/science/experiments.

[63] **ALICE** Collaboration. URL: http://alice.web.cern.ch/.

[64] **ALICE** collaboration. *Technical Design Report of the Inner Tracking System (ITS)*. ALICE-DOC-2005-002. 2004.

[65] **ALICE** Collaboration. "Alignment of the ALICE Inner Tracking System with cosmic-ray tracks". In: *JINST* **5** (2010). P03003. DOI: 10.1088/1748-0221/5/03/P03003.

[66] J. Alme *et al.*. "The ALICE TPC, a large 3-dimensional tracking device with fast readout for ultra-high multiplicity events". In: *Nucl.Instrum.Meth. A* **622** (2010). arXiv:1001.1950 [physics.ins-det]. DOI: 10.1016/j.nima.2010.04.042.

[67] F. Carnesecchi for the **ALICE** Collaboration. "Performance of the ALICE Time-Of-Flight detector at the LHC". In: *JINST* **14** (2019). arXiv:1806.03825 [physics.ins-det]. DOI: 10.1088/1748-0221/14/06/C06023.

[68] **ALICE** collaboration. *Technical Design Report for the upgrade of the ALICE Time Projection Chamber*. ALICE-TDR-016. 2014.

[69] **ALICE** Collaboration. "Performance of the ALICE VZERO system". In: *JINST* **8** (2013). P10016. DOI: 10.1088/1748-0221/8/10/P10016.

[70] **ALICE** collaboration. *Technical Design Report for the Zero Degree Calorimeter (ZDC)*. ALICE-TDR-3. 1999.

[71] K. Oyama (for the **ALICE** collabration). *Reference cross section measurements with ALICE in pp and Pb-Pb collisions at LHC*. arXiv:1305.7044 [nucl-ex]. 2013.

[72] **ALICE** collaboration, B. Abelev et Al.. "Directed Flow of Charm Quarks as a Witness of the Initial Strong Magnetic Field in Ultra-Relativistic Heavy Ion Collisions". In: *Phys. Rev. Lett.* **111** (2013). arXiv:1306.4145 [nucl-ex]. DOI: 10.1103/PhysRevLett.111.232302.

[73] M. Luzum and J. Ollitrault. "Eliminating experimental bias in anisotropic-flow measurements of high-energy nuclear collisions". In: *Phys. Rev. C* **87** (2013). arXiv:1209.2323 [nucl-ex]. DOI: 10.1103/PhysRevC.87.044907.

[74] **ALICE** collaboration, B. Abelev et Al.. "Measurement of charm production at central rapidity in proton-proton collisions at $\sqrt{s}$ = 7 TeV ". In: *JHEP* **128** (2012). arXiv:1111.1553 [hep-ex]. DOI: 10.1007/JHEP01(2012)128.

[75] U. Gursoy et Al.. "Chagre-dependent flow induced by magnetic and electric fields in heavy ion collisions". In: *Phys. Rev. C* **98** (2018). arXiv:1806.05288 [hep-ph]. DOI: 10.1103/PhysRevC.98.055201.

[76] M. Tanabashi et Al. (Particle Data Group). "Review of Particle Physics". In: *Phys. Rev. D* **98** (2018). DOI: 10.1103/PhysRevD.98.030001.

[77] S. Bjelogrlic. "Azimuthal angular correlations of D mesons and charged particles with the ALICE detector at the LHC". PhD thesis. Utrecht University, 2016.

[78] **ALICE** collaboration, B. Abelev et Al.. "Azimuthal anisotropy of D meson production in Pb-Pb collisions at $\sqrt{s_{\mathrm{NN}}}$ = 2.76 TeV ". In: *Phys. Rev. C* **90** (2014). arXiv:1405.2001 [nucl-ex]. DOI: 10.1103/PhysRevC.90.034904.

[79] S. Jaelani for the **ALICE** collaboration. *Measurement of non-strange D-meson production and azimuthal anisotropy in Pb-Pb collisions with ALICE at the LHC*. arXiv:1910.04504 [nucl-ex]. 2019.

[80] **CERN**. URL: https://root.cern.ch/.

[81] **ALICE** collaboration. URL: https://alice-doc.github.io/alice-analysis-tutorial/.

[82] **ALICE** collaboration, S. Acharya et Al.. "Measurement of D^0, D^+, D^{*+} and D_S^+ production in Pb-Pb collisions at $\sqrt{s} = 5.02$ TeV ". In: *JHEP* **174** (2018). arXiv:1804.09083 [nucl-ex]. DOI: 10.1007/JHEP10(2018)174.

Appendix A: Details on the analyses

Below the details on the analysis are presented, for reproducing the analysis described in this thesis. First the names of the code as they can be found in the AliPhysics library are given. Then the data set used for the analysis and the settings used for the analysis on the LEGO trains will be specified. Finally the topological cuts of the main directed flow analysis will be given.

A1: Codes from Github

For the directed flow analyses the following codes were used from the AliPhysics library for performing the core of the analysis on the grid:

- AliAnalysisTaskHFv1.cxx
- AliAnalysisTaskHFv1.h
- AddTaskHFv1.C

For the Cut optimisation process the following codes were used from the AliPhysics library to analyse the data on the grid:

- AliAnalysisTaskSESignificance.cxx
- AliAnalysisTaskSESignificance.h
- AddTaskSignificance.C

For the check on the pseudorapidity dependence of the efficiency the following codes from the AliPhysics library were used to analyse the data on the grid:

- AliCFTaskVertexingHF.cxx
- AliCFTaskVertexingHF.h
- AddTaskCFVertexingHFCascade.C

A2: Data-set

The analysis on the charge dependent directed flow of the D^{*+} mesons was performed in the 2015 Pb–Pb data set LHC15o_AOD194_pass1 using the following run numbers:

246994, 246991, 246989, 246984, 246982, 246948, 246945, 246928, 246851, 246847, 246846, 246845, 246844, 246810, 246809, 246808, 246807, 246805, 246804, 246766, 246765, 246763, 246760, 246759, 246758, 246757, 246751, 246750, 246495, 246493, 246488, 246487, 246434, 246431, 246424, 246276, 246275, 246272, 246271, 246225, 246222, 246217, 246185, 246182, 246181, 246180, 246178, 246153, 246152, 246151, 246148, 246115, 246113, 246089, 246087, 246053, 246052, 246049, 246048, 246042, 246037, 246036, 246012, 246003, 246001, 245954, 245952, 245949, 245923, 245833, 245831, 245829, 245705, 245702, 245692, 245683.

In the cut optimisation process and in the cut variation analyses the same run numbers were used. The check on the pseudorapidity dependence of the efficiency was performed in the Monte-Carlo data LHC16i2b_AOD198 using the following run numbers:

246994, 246991, 246989, 246984, 246982, 246948, 246945, 246928, 246851, 246847, 246846, 246845, 246844, 246810, 246809, 246808, 246807, 246805, 246804, 246766, 246765, 246763, 246760, 246759, 246758, 246757, 246751, 246750, 246495, 246493, 246488, 246487, 246434, 246431, 246424, 246276, 246275, 246272, 246271, 246225, 246222, 246217, 246185, 246182, 246181, 246180, 246178, 246153, 246152, 246151, 246115, 246113, 246089, 246087, 246053, 246052, 246049, 246048, 246042, 246037, 246036, 246012, 246003, 246001, 245954, 245952, 245949, 245923, 245833, 245831, 245829, 245705, 245702, 245692, 245683

The calibration of the ZDC Q-vectors was performed in the 2018 Pb–Pb data set LHC18r_pass1 using the following run numbers:

297595, 297590, 297588.

For the main directed flow measurement the following settings were used in the LEGO trains:

- The settings for the AddTask were: AddTaskHFv1.C(1, kTRUE, "alien:///alice/cern.ch/user/o/omassen/Cuts_v1_1040Centr_ 01.root", AliAnalysisTaskHFv1::kDstartoKpipi, "DStartoKpipiCuts", kFALSE, "_test", AliAnalysisTaskHFv1::kZDC, 10., 40., kFALSE, AliAnalysisTaskHFv1::kSP, "QoverM", AliAnalysisTaskHFv1::kq2TPC, 1, kFALSE)

- The dependencies that were run together with the v1 task were: PhysicsSelection, MultSelection_15o, PIDResponse_15o, ZDC_QvectorCalibration

For the directed flow measurements of the cut variation the same settings as described above, varying only the file containing the topological cuts.

In the cut optimisation process the following settings were used in the LEGO trains:

- The settings for the AddTask were: AddTaskSignificance.C("alien:///alice/cern.ch/user/o/omassen/v1CutOptimization_001.root", 2, kFALSE, 0, 8, AliAnalysisTaskSESignificance::kBoth, "CutObj001", "tightercuts")
- The dependencies that were run together with the cut optimisation task were: PhysicsSelection, PIDResponse_15o

For the efficiencies task the following settings were used in the LEGO trains:

- The settings for the AddTask were: AddTaskCFVertexingHFCascade.C("alien:///alice/cern.ch/user/o/omassen/Cuts_v1_1040Centr_optimised_redBins.root", "DStartoKpipiCuts","Eff1040_v1-01", AliCFTaskVertexingHF:: kFalcon,kTRUE,kFALSE, 413,2,kFALSE,kFALSE,kFALSE,kFALSE,kFALSE)
- The dependencies that were run together with the efficiency task were:PhysicsSelection, ImproverTask_15o, PIDResponse

The ZDC-Calibration analysis was done using private jobs, since the code is under construction and is not yet implemented in the AliPhysics library.

A3: Topological cuts

In this part of the appendix the full set of topological cuts is given that was used for the directed flow analysis. The macro used for creating the cut files was makeTFile4CutsDStartoKpipi.C.

Table 8.1: List of the topological cutting parameters used for the direct flow analysis of the D^{*+} mesons. ΔM_{D0} is reported in MeV/c^2, the p_T is given in GeV/c, the DCA and d_0 are evaluated in cm and finally the $d_0 d_0$ is reported in cm^2

p_T (GeV/c)/ variable	[1-2]	[2-3]	[3-4]	[4-5]	[5-6]	[6-7]	[7-8]	[8-10]	[10-12]	[12-16]	[16-24]	[24-36]
ΔM_{D0}	0.025	0.025	0.032	0.032	0.04	0.043	0.045	0.055	0.06	0.074	0.074	0.094
DCA	0.023	0.023	0.022	0.022	0.021	0.021	0.021	0.021	0.021	0.021	0.021	0.02
$\cos\theta*$	0.8	0.8	0.8	0.8	1	1	1	1	1	1	1	1
$p_T(K)$	1	1	1	1	1	1	1	0.9	0.9	0.7	0.5	0.5
$p_T(\pi)$	1	1	1	1	1	1	1	0.9	0.9	0.7	0.5	0.5
$d_0(K)$	0.1	0.1	0.1	0.1	0.1	0.12	0.12	0.12	0.15	0.15	0.15	0.2
$d_0(\pi)$	0.1	0.1	0.1	0.1	0.1	0.12	0.12	0.12	0.15	0.15	0.15	0.2
$d_0 d_0 \cdot 10^{-3}$	-0.00040	-0.00035	-0.0003	-0.0003	-0.00023	-0.0001	-0.0001	-7.5e-05	-7.5e-05	-7.5e-05	-5e-05	0.0004
$\cos\theta_{point}$	0.97	0.94	0.93	0.93	0.93	0.93	0.93	0.93	0.93	0.93	0.92	0.85
$\cos\theta_{point}XY$	0.3	0.3	0.3	0.3	0.3	0.3	0.3	0.3	0.3	0.3	0.3	0.15
dstar inv mass window	0.15	0.15	0.15	0.15	0.15	0.15	0.15	0.15	0.15	0.15	0.15	0.15
$p_T min(\pi_s)$	0.05	0.05	0.05	0.05	0.25	0.3	0.3	0.3	0.3	0.3	0.3	0.3
$p_T max(\pi_s)$	0.5	0.5	0.5	10	10	100	100	100	100	100	100	100
θ	0.5	0.5	0.5	0.5	0.5	0.5	0.5	0.5	1	1	1	1
$\cos\theta_{point}$XY	0.998	0.998	0.998	0.998	0.998	0.998	0.998	0.998	0.998	0.99	0.99	0.9
Norm L_{XY}	7.8	7	6.7	6.5	6.5	6.4	6.4	4.7	4.7	3.7	2	0

Appendix B: Additional Figures and Tables

B1: Simultaneous fits

In the next pages the additional simultaneous fit figures are presented, that were not shown in the main bulk of the thesis.

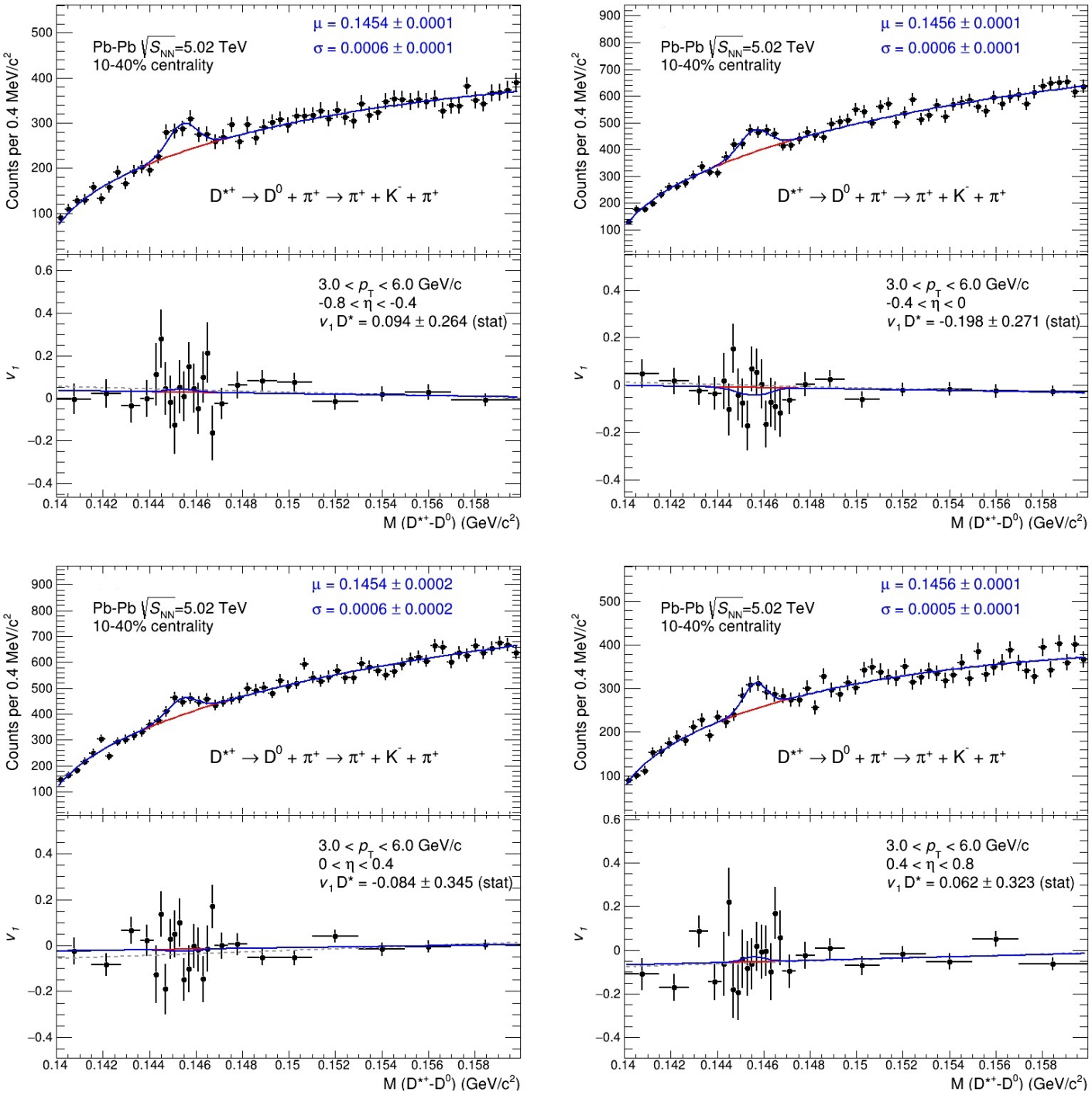

Figure 8.1: Simultaneous fits for the D^{*+} meson in the transverse momentum region $3 < p_{\mathrm{T}} < 6\mathrm{GeV}/c^2$. The top left figure is the $-0.8 < \eta < -0.4$ bin, the top left figure is the $-0.4 < \eta < -0.0$ bin, the bottom left figure is the $0 < \eta < 0.4$ bin and the bottom right figure is the $0.4 < \eta < 0.8$ bin.

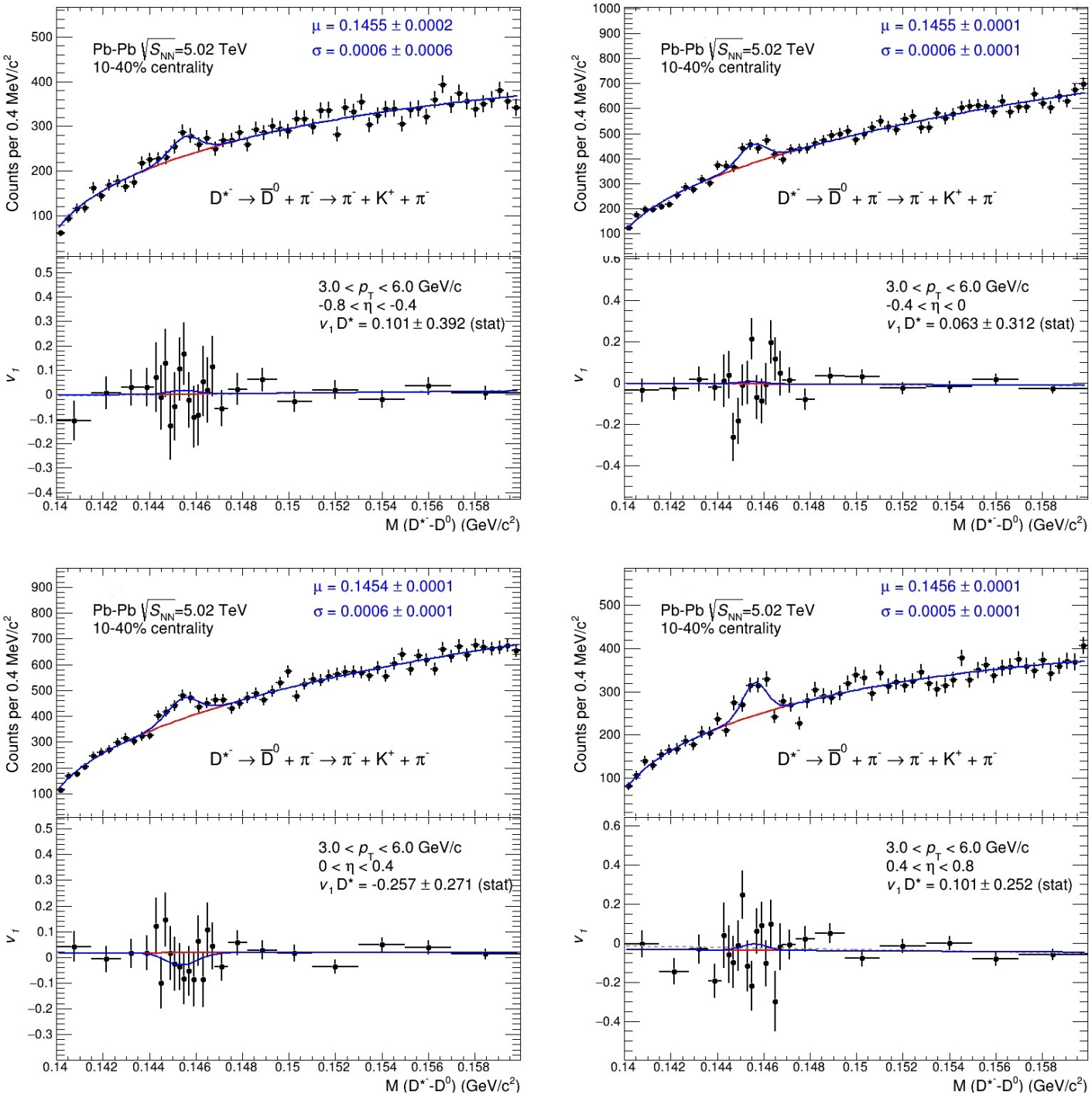

Figure 8.2: Simultaneous fits for the D^{*-} meson in the transverse momentum region $3 < p_T < 6 \mathrm{GeV}/c^2$. The top left figure is the $-0.8 < \eta < -0.4$ bin, the top left figure is the $-0.4 < \eta < -0.0$ bin, the bottom left figure is the $0 < \eta < 0.4$ bin and the bottom right figure is the $0.4 < \eta < 0.8$ bin.

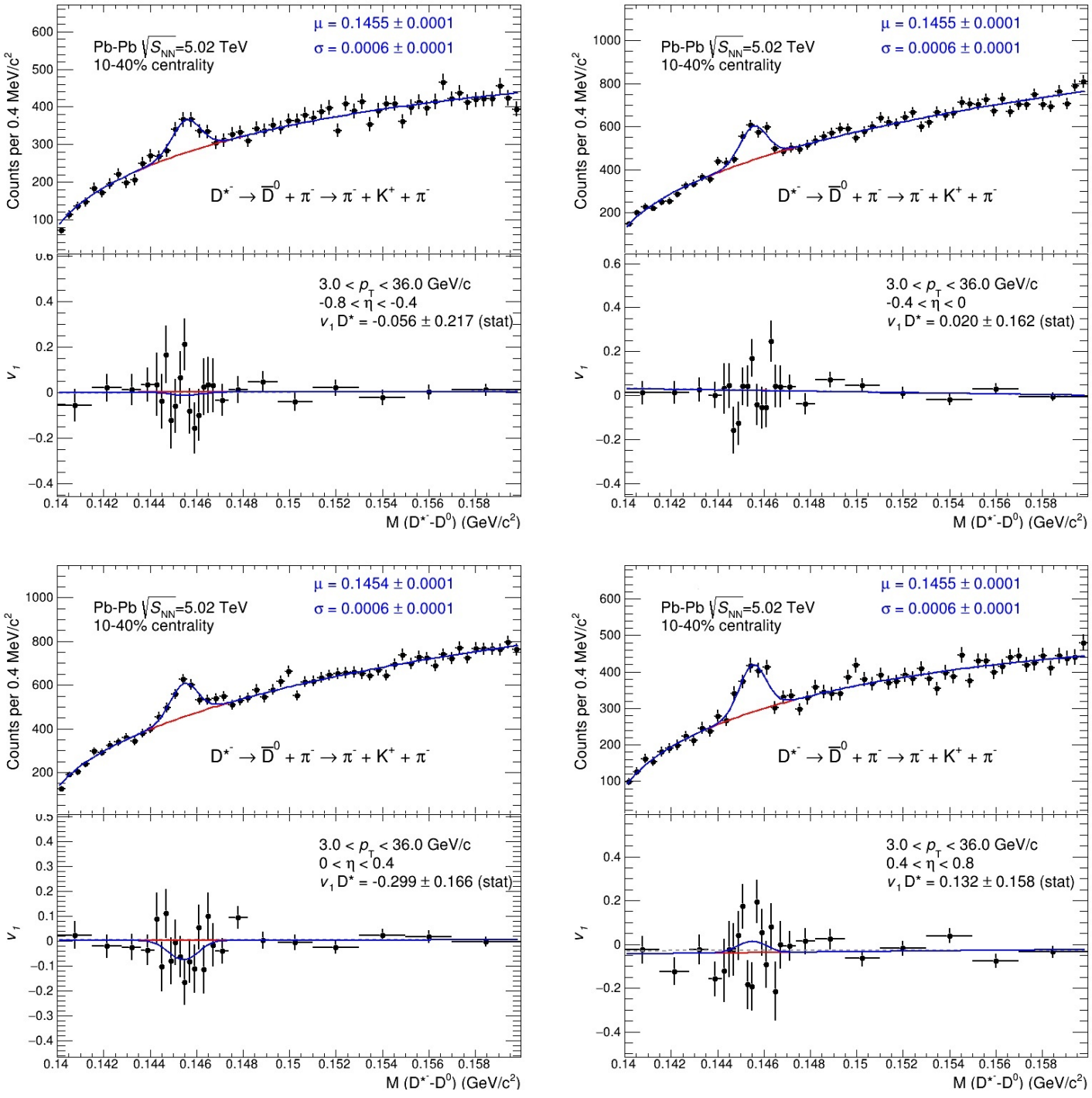

Figure 8.3: Simultaneous fits for the D^{*-} meson in the transverse momentum region $3 < p_T < 36 \mathrm{GeV}/c^2$. The top left figure is the $-0.8 < \eta < -0.4$ bin, the top left figure is the $-0.4 < \eta < -0.0$ bin, the bottom left figure is the $0 < \eta < 0.4$ bin and the bottom right figure is the $0.4 < \eta < 0.8$ bin.

B2: Cut Optimisation

In this section first the additional tables showing the changes in cutting parameters according to the cut optimisation process are presented.

Table 8.2: Original and optimised values for the cosine of the θ^* angle

p_{T} (GeV/c)/cos θ^*	Original	Significance	Signal
[3-6]	0.022	0.0201	0.0214
[6-10]	0.021	0.0185	0.0205
[10-16]	0.021	0.018	0.019
[16-36]	0.021	0.0181	0.0174

Table 8.3: Original and optimised values for the $d_0 d_0$

p_{T} (GeV/c)/$d0d0$	Original	Significance	Signal
[3-6]	-0.0003	-0.0003	-0.0003
[6-10]	-0.0001	-0.00015	-0.0001
[10-16]	-7.5e-05	-7.5e-05	-7.5e-05
[16-36]	0.0004	6.2e-05	6.2e-05

Table 8.4: Original and optimised values for cos θ_{point}

p_{T} (GeV/c)/cos θ_{point}	Original	Significance	Signal
[3-6]	0.93	0.96	0.93
[6-10]	0.93	0.983	0.953
[10-16]	0.93	0.96	0.96
[16-36]	0.85	0.973	0.868

Table 8.5: Original and optimised values for the Norm L_{XY}

p_{T} (GeV/c)/Norm L_{XY}	Original	Significance	Signal
[3-6]	6.5	7.4	6.7
[6-10]	6.4	6.4	6.4
[10-16]	3.7	5.85	3.7
[16-36]	0	4	0

B3: Systematics

In this section the additional figures concerning the systematic uncertainties are presented.

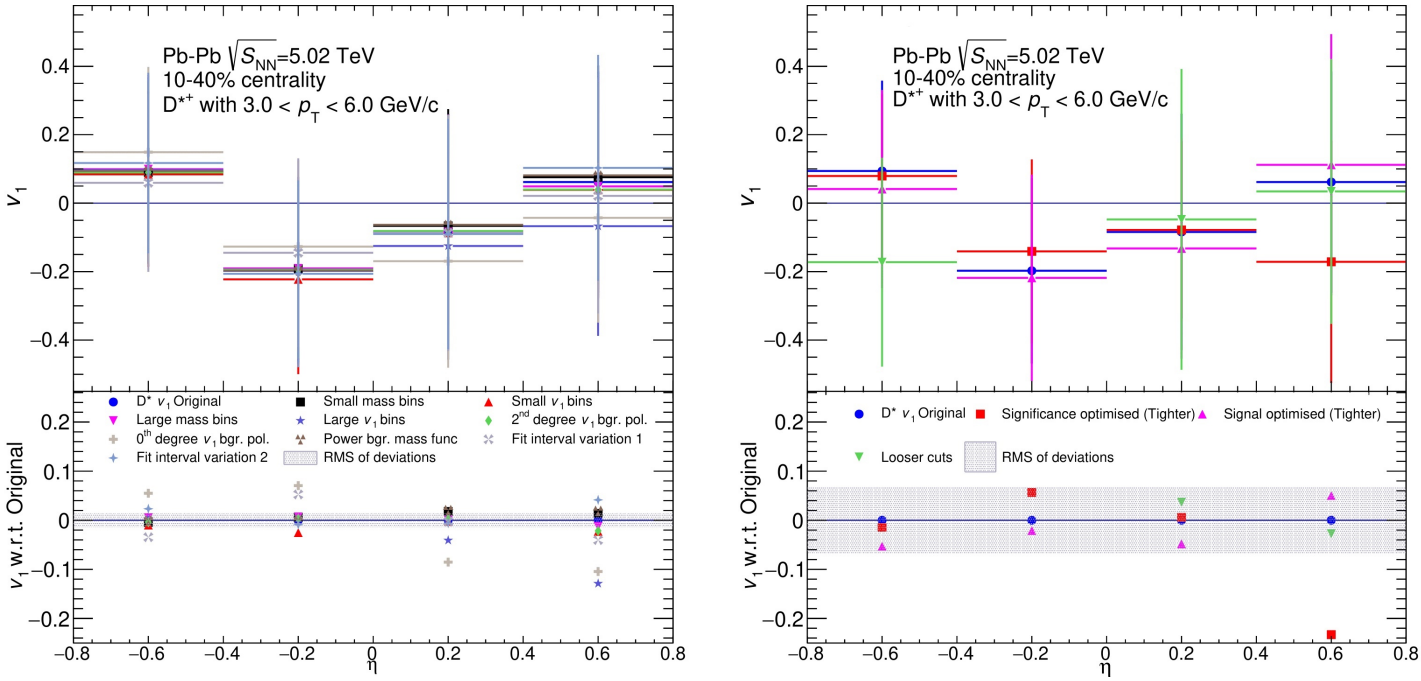

Figure 8.4: Directed flow values for the D^{*+} meson signal extraction (left panel) and cut variation (right panel) in the transverse momentum region $3 < p_T < 6\,\mathrm{GeV}/c^2$.

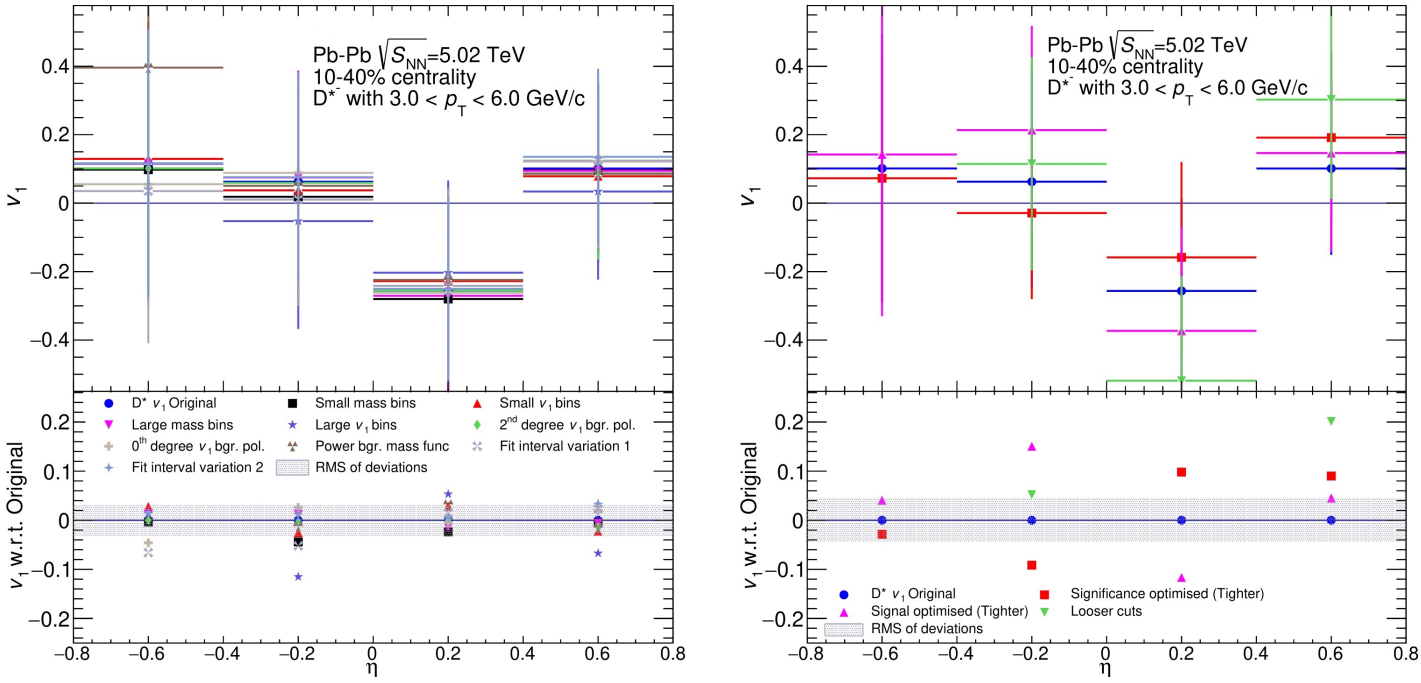

Figure 8.5: Directed flow values for the D^{*-} meson signal extraction (left panel) and cut variation (right panel) in the transverse momentum region $3 < p_T < 6\,\mathrm{GeV}/c^2$.

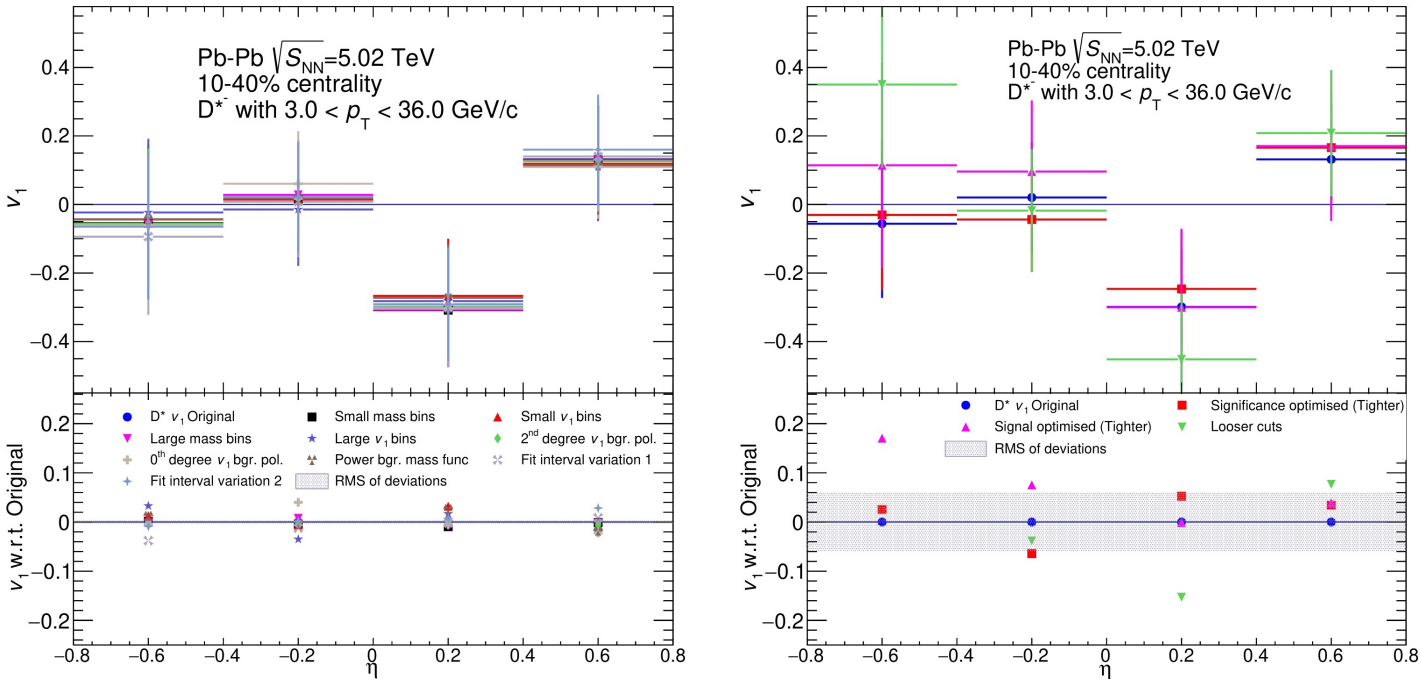

Figure 8.6: Directed flow values for the D^{*-} meson signal extraction (left panel) and cut variation (right panel) in the transverse momentum region $3 < p_T < 36\,\mathrm{GeV}/c^2$.

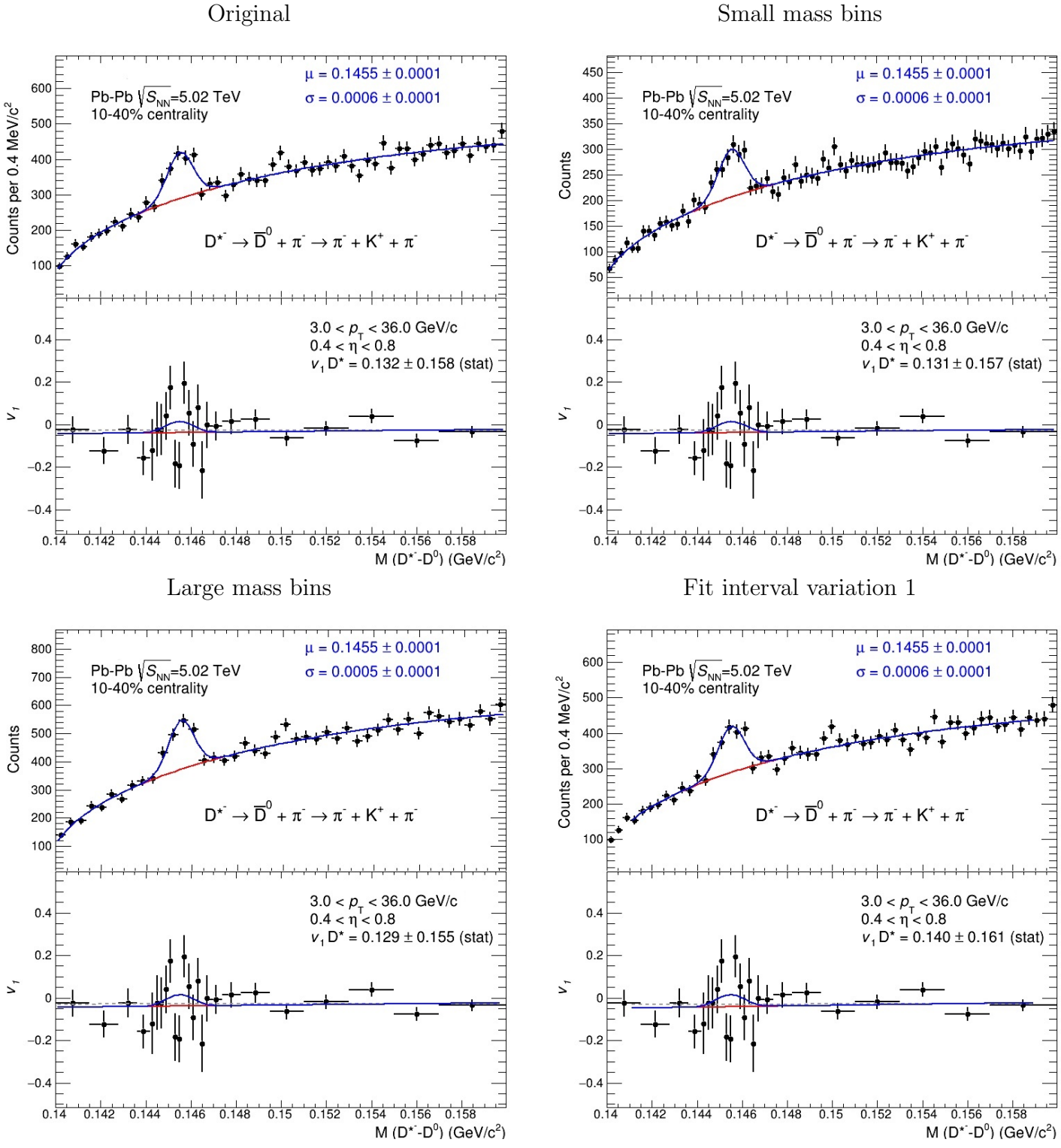

Figure 8.7: Comparison of the original simultaneous fit with the variations for signal extraction for the D^{*-} meson in the transverse momentum region $3 < p_T < 36 \mathrm{GeV}/c^2$ and pseudorapidity region $0.4 < \eta < 0.8$.

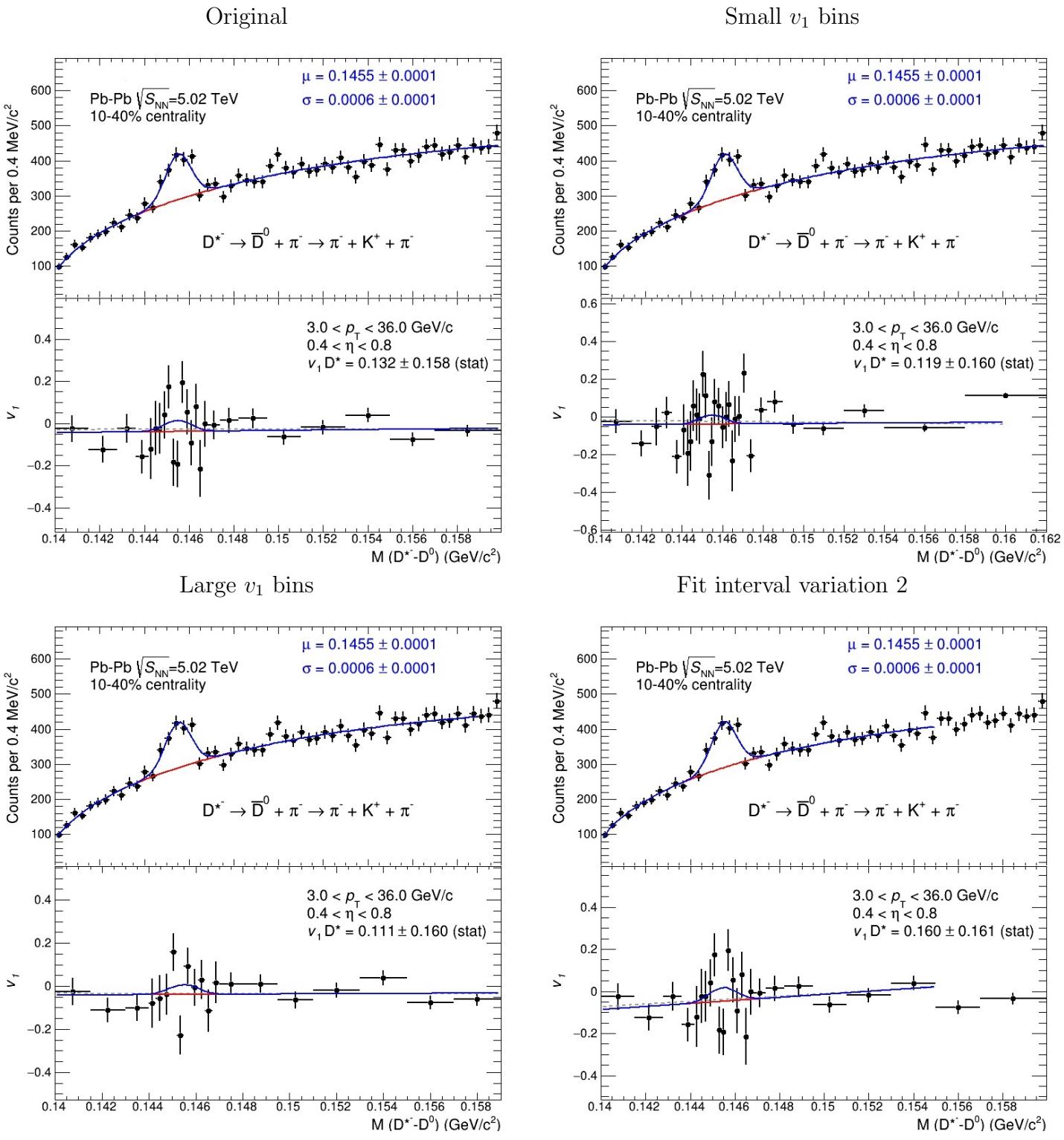

Figure 8.8: Comparison of the original simultaneous fit with the variations for signal extraction for the D^{*-} meson in the transverse momentum region $3 < p_T < 36 \mathrm{GeV}/c^2$ and pseudorapidity region $0.4 < \eta < 0.8$.

Original

Power mass-background function

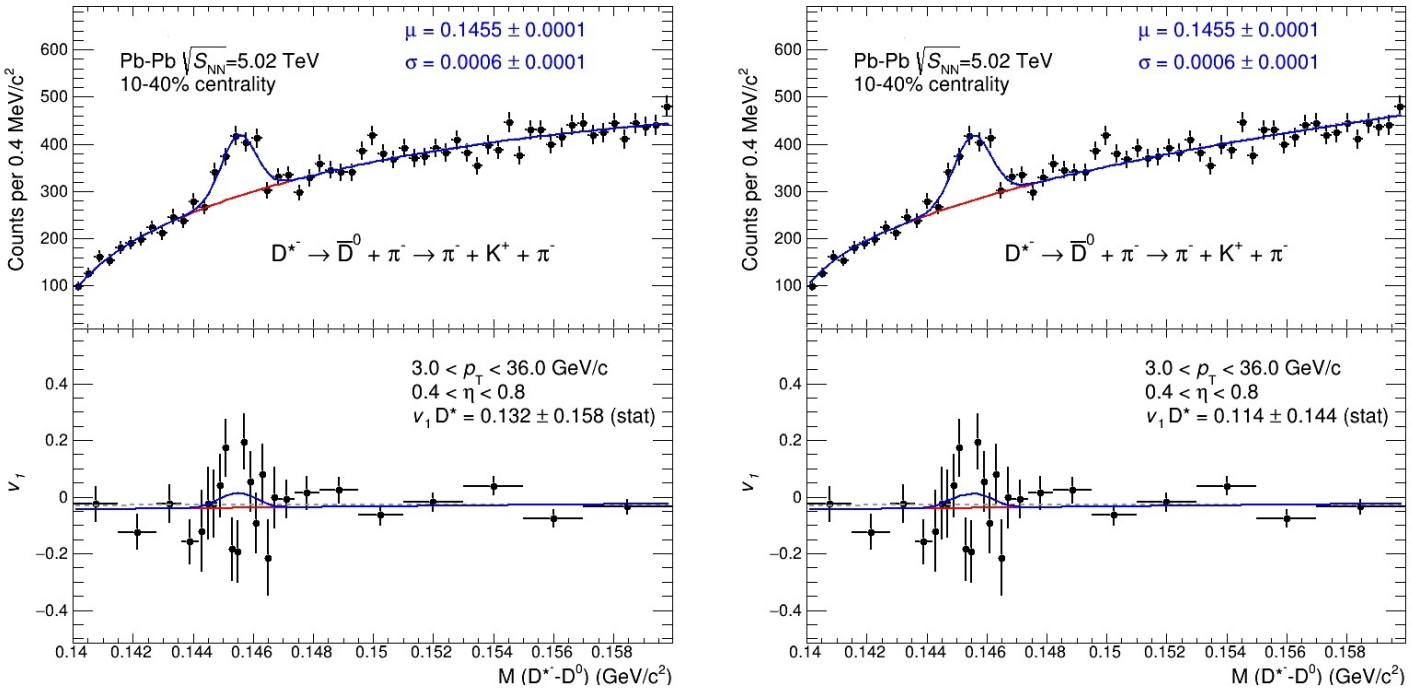

0^{th} order polynomial v_1 background function

2^{nd} order polynomial v_1 background function

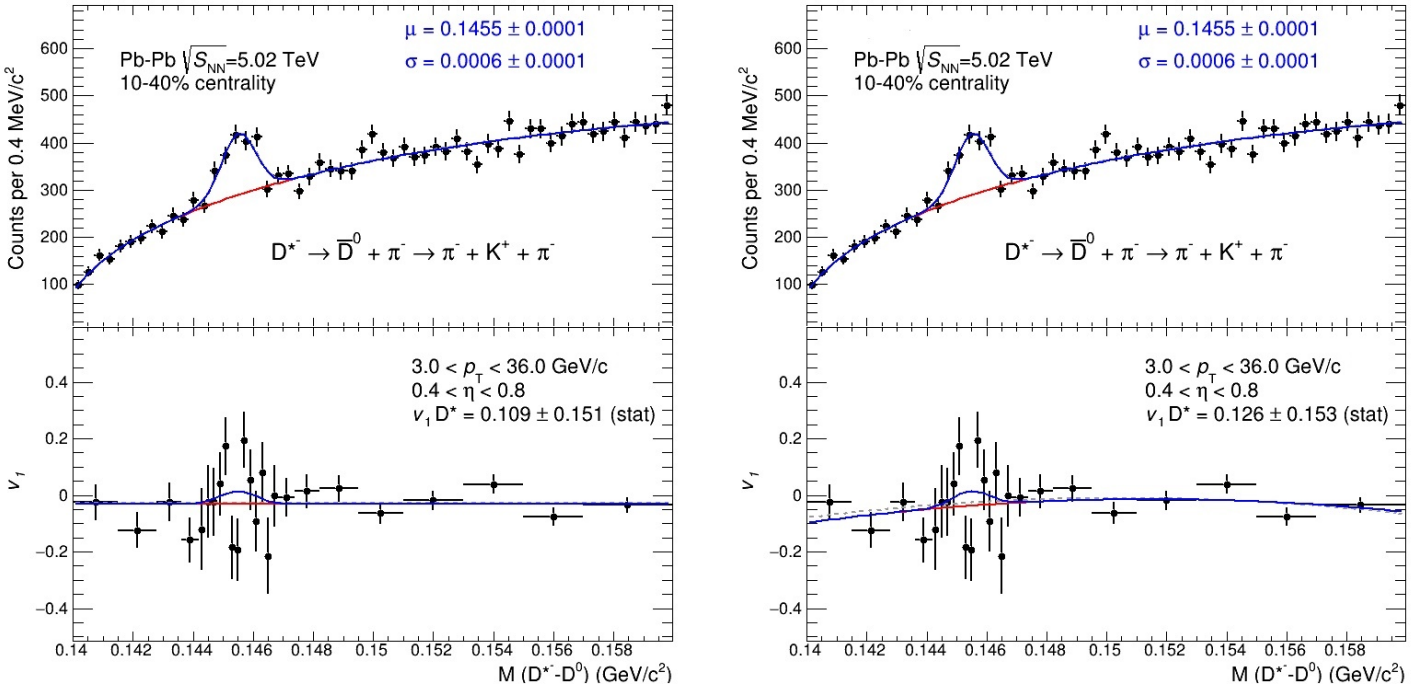

Figure 8.9: Comparison of the original simultaneous fit with the variations for signal extraction for the D^{*-} meson in the transverse momentum region $3 < p_{\mathrm{T}} < 36\mathrm{GeV}/c^2$ and pseudorapidity region $0.4 < \eta < 0.8$.

Acknowledgements

I must admit that I did not expect or think that I was going to put this much effort into my thesis. I also did not expect to enjoy a experimental thesis based on programming and data analysis that much. In both cases I was very wrong. This year has been the year I enjoyed most in my entire bachelor. I got to work with data directly from the largest working machine in the world, the LHC. I got access to the GRID and even got my own CERN email address! That's just really cool and something that I wanted since I was a little kid. But besides this the project was really rewarding, performing an entire analysis including the analysis of the systematics. On top of that I got to design an entirely new code teaching me more about the analysis framework of the ALICE collaboration and programming in C++. I also got to present at the ALICE wide research group D2H twice, in which I was treated as a full member of the collaboration that they took seriously. An amazing experience

I want to thank Alessandro Grelli for offering me the chance to work on this amazing project and for all the help he has offered during the process. No matter how busy he was he always had time for a quick chat if there were some questions and he never got tired of our "stupid bachelor student mistakes". I also want to thank Syaefudin Jaelani (aka Jay) for helping me with my endless questions and error messages when I started learning how to use ROOT and the ALICE framework. Also special thanks to Henrique Zanoli for the tremendous amount of help he offered me with writing the ZDC Q-vector re-centring code. A lot of the framework of the code is based on his knowledge and experience. He always offered to help me improve the code even though he was quite busy himself. Furhermore I want to thank the rest of the group, Luuk, Lennart and Auro, for the helpful comments and discussions during the group meetings. Finally I want to thank Justus, a close friend of mine who also did his bachelor thesis this year with Alessandro. It made the project ever so more enjoyable working together with a close friend and I have learned a lot from our many discussions.